Università di Pisa

Scuola di Dottorato in Ingegneria "Leonardo da Vinci"
Programma in Ingegneria Aerospaziale

ING-IND/03 Meccanica del volo

Tesi di Dottorato

Mission Applications for Continuous-Thrust Spacecraft within a Three-Body Problem

Tutore
Prof. Giovanni Mengali

Candidato
Generoso Aliasi

Presidente del Programma
Prof. Giovanni Mengali

Direttore della Scuola
Prof. Stefano Bennati

Marzo 2013

A coloro che sono sempre con me,
ovunque e comunque vada.

Io stimo più il trovar un vero, benché di cosa leggiera, che 'l disputar lungamente delle massime questioni senza conseguir verità nissuna.

Galileo Galilei
Opere, IV

We sail through endless skies,
stars shine like eyes,
the black night sighs.
The Moon in silver dreams
falls down in beams
light of the night.
The Earth a purple blaze
of sapphire haze
in orbit always.
While down below the trees,
bathed in cool breeze,
silver starlight breaks
dawn from night.
And so, we pass on by
the crimson eye
of great god Mars
as we travel the universe

Black Sabbath
Planet Caravan - Paranoid

Abstract

This Thesis presents a study of possible mission scenarios for spacecraft propelled by continuous-thrust propulsion systems within a gravitational model of three bodies.

The first Part concerns the study of the existence, stability, and control of *Artificial Equilibrium Point*s. A general mathematical model (referred to as *Generalized Sail*) for the propulsive acceleration of a spacecraft subjected to a continuous and purely radial thrust is proposed. Based on the choice of a coefficient related to the propulsion system and of a parameter (the lightness number) related to the system performance, the propulsive acceleration model encompasses the behavior of different propulsion systems, like Solar Sails, Electric Solar Wind Sails, Magnetic Sails and Electric Thrusters. The continuous propulsive acceleration provided by a Generalized Sail is used to create and maintain Artificial Equilibrium Points. The loci (curves in the space) and the stability of such Artificial Equilibrium Points are discussed both in the *Circular* and in the *Elliptic Restricted Three-Body Problem*. Even though similarities between the two problems exist in the description of the geometrical loci, some differences in the stability analysis are shown. Moreover, a Generalized Sail is required to provide a varying lightness number in the elliptical problem to maintain an Artificial Equilibrium Point.

The stabilization and control of a interesting class of Artificial Equilibrium Points, the L_1-type points, is also discussed to show how a simple Proportional-Derivative feedback control logic, based on the variation of the lightness number, is able to guarantee asymptotical stability. In this respect, two control techniques for Solar Sail based spacecraft are examined: *Solar Balloon* and *Electrochromic Material Panels*. A Solar Balloon can provide a passive Proportional control, however, if manufactured with the current technology, it is shown to be unable to stabilize an Artificial Equilibrium Point. Electrochromic Material Panels are, instead, used for an active control system. A suitable dimensioning of such a system provides asymptotical stability for the Artificial Equilibrium Points, when saturation effects are counteracted by means of an anti-windup compensator.

In the first Part, the Artificial Equilibrium Points created by an *Electric Solar Wind Sail* are also investigated. In this case, the radial thrust hypothesis is left, and the Electric Solar Wind Sail is assumed to maintain a constant attitude with respect to an orbital reference frame. This increases the number of attainable Artificial Equilibrium Points, and the loci now become space regions, whose extension depends on the thrust capabilities of the spacecraft. For those points a linear stability analysis is also provided.

In the second Part, new frozen orbits are sought for Solar Sail based space-

craft around an oblate planet and under the effects of the Sun's gravitational attraction. An averaging method of the Hamiltonian that describes the spacecraft motion is used to find new families of *displaced frozen orbits*, varying the sail lightness number. These orbits are examined both analytically and numerically when Mercury is the reference planet.

Preface

This Thesis is the result of the work done during the Ph.D. course carried out from January 2010 to December 2012 under the supervision of Prof. Giovanni Mengali. Most of the work was conducted at the Aerospace Engineering Department of the University of Pisa, except for the part concerning the frozen orbits, which was developed at the Advanced Space Concepts Laboratory of the University of Strathclyde in Glasgow (Scotland, UK) under the supervision of Dr. Malcolm Macdonald from February 2012 to July 2012.

Some of the results obtained can be found in the following papers:

- Aliasi G., Mengali G., Quarta A. A., *"Artificial Equilibrium Points for an Electric Sail with Constant Attitude"*, Journal of Spacecraft and Rockets, In Press.

- Aliasi G., Mengali G., Quarta A. A., *"Artificial Lagrange Points for Solar Sail with Electrochromic Material Panels"*, Journal of Guidance, Control, and Dynamics, In Press. doi: 10.2514/1.58167

- Aliasi G., Mengali G., Quarta A. A., *"Artificial Equilibrium Points for a Generalized Sail in the Elliptic Restricted Three-Body Problem"*, Celestial Mechanics and Dynamical Astronomy, Vol. 114, No. 1–2, pp. 181–200, October 2012. doi: 10.1007/s10569-012-9425-z

- Aliasi G., Mengali G., Quarta A. A., *"Passive Control Feasibility of Collinear Equilibrium Points with Solar Balloons"*, Journal of Guidance, Control, and Dynamics, Vol. 35, No. 5, pp. 1657-1661, September-October 2012. doi: 10.2514/1.57393

- Aliasi G., Mengali G., Quarta A. A., *"Artificial Equilibrium Points for a Generalized Sail in a Circular Restricted Three-Body Problem"*, Celestial Mechanics and Dynamical Astronomy, Vol. 110, No. 4 , pp. 343-368, August 2011. doi: 10.1007/s10569-011-9366-y

- Aliasi G., Mengali G., Quarta A. A., *"Artificial Equilibrium Points Mantained by an Electric Sail"*, European Planetary Science Congress 2010, Vol. 5, EPSC2010-501, 19-24 September, Rome, Italy, 2010.

while an other part of them is under review:

- Aliasi G., Macdonald M., Mengali G., *"Displaced Frozen Orbits"*, Journal of Guidance, Control, and Dynamics, Submitted.

Works concerning mission design with Electric Solar Wind Sails and Magnetic Sails, developed in a complementary way with respect to the Ph.D. project, can be found in

- Quarta A. A., Mengali G., Aliasi G., *"Optimal Control Laws for Heliocentric Transfers with a Magnetic Sail"*, Acta Astronautica, Submitted.
- Mengali G., Quarta A. A., Aliasi G., *"A Graphical Approach to E-Sail Mission Design with Radial Thrust"*, Acta Astronautica, Vol. 82, No. 2, pp. 197–208, February 2013. doi: 10.1016/ j.actaastro.2012.03.022
- Mengali G., Quarta A. A., Aliasi G., *"A Graphical Approach to E-Sail Mission Design with Radial Thrust"*, 7th IAA Symposium on Realistic Near-Term Advanced Scientific Space Missions, pp 97-102, 11-13 July, Aosta, Italy, 2011.

Acknowledgements

This is the end of another phase of my life, and, as always when phases finish, some things are going to remain the same, other things are going to change.

Every time a breakthrough happens in my life, I like to think about who has spent the previous period with me, sustaining and helping me, and enjoying it with me too. Here, I have the possibility to thank most of those people.

First of all, my gratitude goes to Prof. Mengali and to Prof. Quarta, who gave me the chance to take the Ph.D. course challenge. Thanks to Giovanni and thanks to Alessandro for all their precious support and for all the opportunities they have offered me.

I am also very grateful to Dr. Malcolm Macdonald, who gave me the possibility of a visiting period at the University of Strathclyde, and to his research group (in particular Chris, Pam, and Steve). Thanks also to the entire team of the Advanced Space Concepts Laboratory for the fertile working environment it provided me during my visiting period. Special thanks go to Daniele for the dinner time we spent together, talking about everything and nothing all at once, to Simone and Luca, who gave me a welcome one of the first days I was in Glasgow, and to Marta, who never told me to stop speaking about "frozen orbits". And thanks to Scotland, a stunning country where people are polite, landscapes are breathtaking, whiskies (yes, with -ies, they are Scotch) are for the most part exquisitely single malt, sheep are fat, and cows are hairy.

My special thanks go to all the guys of the DIA with whom coffee breaks, dinner reunions, and other stuff have never been wasted time. Thanks to the CDC group (Daniele, Massi, Giulia, Giuseppe, Roberto, Pasquale), to Vittorio, and to Andrea. A special thanks to Fabrizio and Annabella for their friendship, for their ways of jocking with me and making me laugh every day, and for the time spent talking about serious matter, and also for bearing with me.

A big thanks to all my friends in Pisa, both the ones who are no longer in the city (the list is too long to be presented) and the ones still here. In particular, thanks to Carletto, whose presence is always pleasant and whose parties are unforgettable.

I want also to thank my old friend Erminio. We don't meet very often, but I know he is always ready when I call.

I most want to thank my family. Thanks to my parents, who always support me and encourage me, this award mostly is their merit. Thanks to Gilda and Carmine, who are always ready to listen to me, and who continue to tolerate me. Very special thanks to my little nephew Guido, whose smiles at the evening after

work make me forget all my troubles. Last but not least, thanks to Cristina, who made (and is still making) me a better man. If behind every great man there is a great woman, then I am on the right track to become great.

Generoso Aliasi

Ringraziamenti

Questa è la fine di un'altra fase della mia vita, e, come sempre quando le fasi finiscono, alcune cose rimarranno le stesse, altre cose stanno per cambiare.

Ogni volta che si verifica una svolta nella mia vita, mi piace pensare a chi ha trascorso il periodo precedente assieme a me, sostenendomi e aiutandomi, e anche divertendosi con me. Qui, ho la possibilità di ringraziare la maggior parte di quelle persone.

Prima di tutto, la mia gratitudine va al Prof. Mengali e al Prof. Quarta, che mi hanno dato la possibilità di raccogliere la sfida del dottorato di ricerca. Un grazie a Giovanni e un grazie ad Alessandro per tutto il loro prezioso supporto e per tutte le opportunità che mi hanno offerto.

Sono anche molto grato al dottor Malcolm Macdonald, che mi ha dato la possibilità di un periodo di visita presso l'Università di Strathclyde, e al suo gruppo di ricerca (in particolare Chris, Pam, e Steve). Grazie anche a tutto il team dell'Advanced Space Concepts Laboratory per avermi procurato un fertile ambiente di lavoro durante il mio periodo di visita. Un ringraziamento particolare va a Daniele per le cene che abbiamo passato insieme, parlando di tutto e niente nello stesso momento, a Simone e Luca, che mi hanno dato il benvenuto uno dei primi giorni che ero a Glasgow, e a Marta, che non mi ha mai detto di smetterla di rompere parlando di "frozen orbits". E grazie alla Scozia, paese splendido dove le persone sono cortesi, i paesaggi sono mozzafiato, i whiskies (sì, con -ies, perchè sono Scotch) sono per la maggior parte squisitamente "single malt", le pecore sono grasse, e le mucche hanno i capelli.

Un ringraziamento speciale va a tutti i ragazzi de DIA con i quali pause caffè, cene sociali, e tutto il resto non sono mai stati tempo sprecato. Grazie al gruppo CDC (Daniele, Massi, Giulia, Giuseppe, Roberto, Pasquale), a Vittorio, e ad Andrea. Un ringraziamento speciale a Fabrizio e Annabella per la loro amicizia, per il loro modo di prendermi in giro e di farmi ridere ogni giorno, e per il tempo speso a parlare di cose serie, e anche perché mi sopportano.

Un grazie a tutti i miei amici di Pisa, sia quelli che non sono più a Pisa (l'elenco è troppo lungo per riportarlo) e quelli che sono ancora qui. In particolare, grazie a Carletto, la cui presenza è sempre piacevole e le cui feste sono indimenticabili.

Voglio anche ringraziare il mio amico di vecchia data Erminio. Non ci incontriamo molto spesso, ma io so che è sempre pronto quando chiamo.

Chi più desidero ringraziare è, però, la mia famiglia. Grazie ai miei genitori, che da sempre mi sostengono e mi incoraggiano, questo traguardo è in buona parte merito loro. Grazie a Gilda e a Carmine, sempre pronti ad ascoltarmi e che

ancora mi sopportano. Un ringraziamento molto speciale al mio nipotino Guido, i cui sorrisi la sera dopo lavoro mi fanno dimenticare tutte le preoccupazioni. E infine, grazie a Cristina, che ha fatto (e continua a fare) di me un uomo migliore. Se dietro un grande uomo c'è sempre una grande donna, allora io sono sulla strada giusta per diventarlo.

Generoso Aliasi

Contents

Chapter 1

Introduction

Since the dawning of astronautical sciences, continuous-thrust propulsion has been considered as an important way to provide high performance options for a large number of missions. Indeed, since the beginning of past century, the germinal ideas about continuous-thrust propulsion systems were formulated by the fathers of astronautics.

In 1906, for the first time, the pioneer of American rocket science Robert Goddard conjectured the possibility of using electric propulsion based on the prospective production of "*reaction with electrons*[1] *moving with the velocity of light*" [1,2]. Five years later, in 1911, the father of Soviet astronautics, Konstantin E. Tsiolkovsky, aware of the existence of fast particles, recognized the effectiveness of electric propulsion and mentioned the prophetic sentence: "*It is possible that in time we may use electricity to produce a huge velocity for the particles ejected from a rocket device*" [2,3]. He knew, from the famous equation having his name, the importance of rocket exhaust velocity to space propulsion. Some years later[2], in the early 1920's, Tsiolkovsky caught the possibility of solar sailing, and his co-worker Fridrickh A. Tsander wrote: "*For flight in interplanetary space, I am working on the idea of flying using tremendous mirrors of very thin sheets, capable of achieving favourable results*" [4].

From the era of pioneers to the present, researchers have become more and more interested in continuous-thrust technology and its applications. Such interest is well understood considering the increasing trend of the amount of work done

[1] At that time, only electrons were known to attain high velocities under the effects of electric fields at high voltage. Even though positively charged rays had been observed in cathode ray tubes, the concept of the ion had not yet been fully established.

[2] It is worth noting that, in the second half of 19th century, several science fiction authors already penned stories of spaceships propelled by large mirrors. See for example *From the Earth to the Moon* (Verne J., 1865) and *The Extraordinary Adventures of a Russian Scientist* (Le Faure G. and De Graffigny H., 1889).

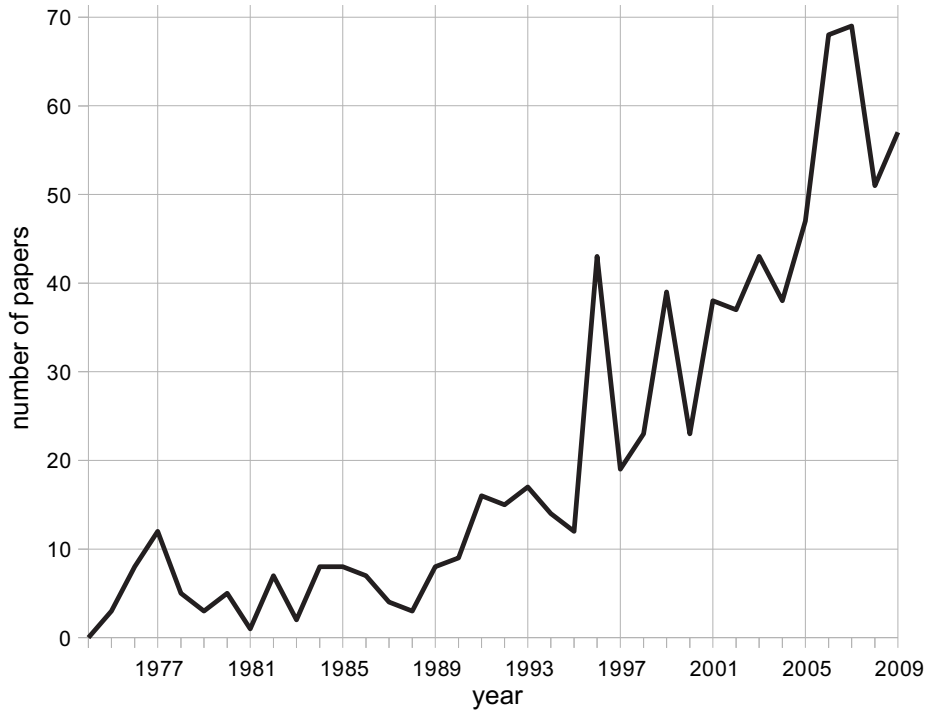

Figure 1.1: Analysis of the number of papers about continuous-thrust technology and applications published from 1974 to 2009.

in the last four decades. Figure 1.1 is a (not exhaustive) proof of such a trend[3]. Starting from 1974, the number of papers about continuous-thrust propulsion and its applications has grown nearly exponentially.

The increasing interest in continuous-thrust technology is also confirmed by the number of spacecraft that, starting from the 1960s, have used such type of propulsion systems (see Fig. 1.2, for some examples). From the first tests for Electric Thrusters (with the missions *Sert 1* and *Zond 2*), electric propulsion has been more and more widely used both for conventional missions (e.g., station keeping of geostationary satellites) and for more ambitious missions as, for example, missions towards the Moon (*Smart 1*) or towards asteroids and comets (*Deep Space 1*, *Hayabusa*, *Dawn*). Recently, the missions *Ikaros* and *NanoSail-D* have shown that Solar Sail technology is another practicable option for deep space propulsion[4].

[3]The analysis is based on the ISI Web of Knowledge^{TM}database (`www.webofknowledge.com`) and includes Articles, Notes, Reviews and Proceedings published in the most important journals of the aerospace field.

[4]Actually, the *Mariner 10*, *Messenger* and *Hayabusa* missions already showed the practicability of solar pressure on large structure for spacecraft attitude control, but not for spacecraft propulsion.

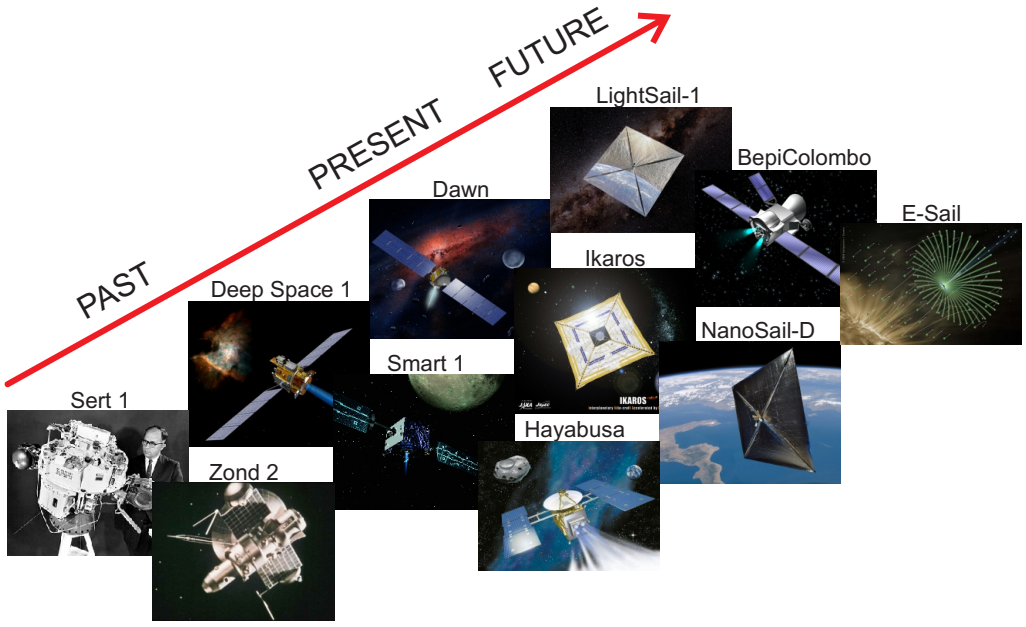

Figure 1.2: Examples of spacecraft using continuous-thrust propulsion systems.

The future seems to reserve an even more relevant use of continuous-thrust propulsion systems. Spacecraft like *LightSail-1* will continue testing the feasibility of space propulsion by means of Solar Sails, and *BepiColombo* will exploit the high impulse of an ion thruster to brake against the Sun's gravity. Furthermore, other exotic continuous-thrust propulsion systems are object of study by the scientific community. Examples are the *Magnetic Sail* (MagSail) conceived by D. G. Andrews and R. Zubrin [5] in 1990s or the *Electric Solar Wind Sail* (E-Sail) invented by P. Jahnunen [6] in 2004.

At this point a question arises: What are the motivations behind such an increasing interest? The answer involves two main reasons: 1) growth of either the mission life or the dry mass of the spacecraft, and 2) possibility of identification of new mission scenarios.

For example, in electric propulsion the much higher specific impulses (than those available from chemical thrusters) allow the propellant required for a given spacecraft velocity change to be reduced or, alternatively, the ratio of dry to initial spacecraft mass to be increased [7]. Similarly, in case of beamed momentum propulsion systems (Solar Sails, MagSails or E-Sails), the propellant mass is driven to zero, thus increasing the mission life theoretically to infinity.

On the other hand, as long as a continuous propulsive thrust is used on a spacecraft (in addition to the gravitational force due to celestial bodies), different and new mission scenarios are enabled [8]. In particular, in a two-body

gravitational model, new transfer orbits and displaced orbits are enabled, see Fig. 1.3. Moreover, in a three-body gravitational model, of particular interest

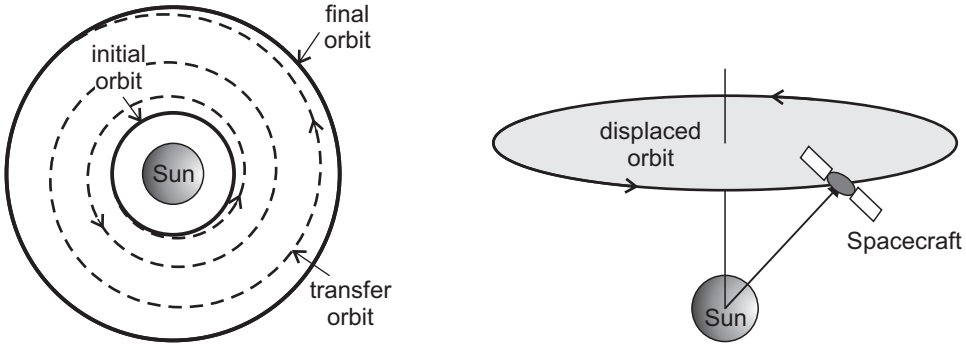

(a) Transfer orbit.

(b) Displaced orbit.

Figure 1.3: Example of non-Keplerian orbits with continuous-thrust propulsion system.

is the possibility of generating new equilibrium points [8], thus enabling mission scenarios like the *Geostorm* [9] or the *L1 Diamond* [10], both suggested for monitoring missions of space weather by means of Solar Sail based spacecraft, see Fig. 1.4.

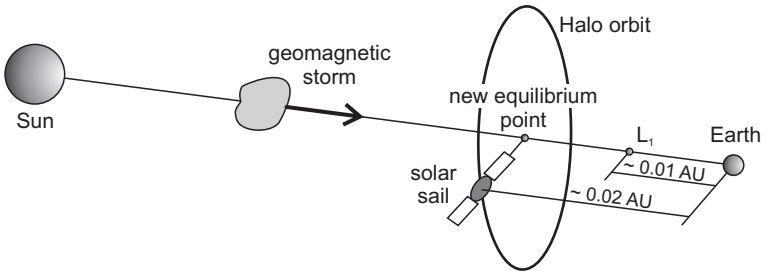

(a) Geostorm mission.

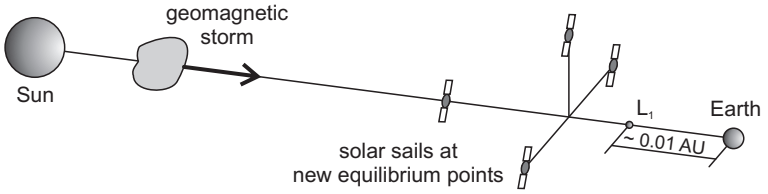

(b) L1 Diamond mission.

Figure 1.4: Examples of mission within a three-body gravitational model for Solar Sail based spacecraft.

This Thesis mainly concerns the effects of continuous-thrust propulsion systems on the spacecraft dynamics in a *Restricted Three-Body Problem*, with the dual aim of defining new possible mission scenarios and studying their practicability.

Most of the Thesis (Part I) deals with the concept of *Artificial Equilibrium Point*s, defined in Section 2.1.3. Such a part of the work started in 2010 as a natural continuation of the Master Thesis regarding the new equilibrium points in a *Circular Restricted Three-Body Problem* with radial and continuous-thrust propulsion systems. Using the Master Thesis as the starting point of the research project, the circular problem of three bodies has been reconsidered and developed from a different perspective after the introduction of a new mathematical model for the continuous propulsive acceleration of a spacecraft, whose name is *Generalized Sail*. An analysis of such a model can be found in Section 2.2, while the revisited approach to the *Circular Restricted Three-Body Problem* is found in Chapter 3. With a similar approach, the study of equilibrium points in an *Elliptic Restricted Three-Body Problem* is proposed in Chapter 4. In Chapter 5, the assumption of radial thrust (used in the Generalized Sail model) is relaxed, and the interest is confined to the use of E-Sails in generating *Artificial Equilibrium Point*s. The stability and controllability of a particularly interesting class of equilibrium points is then studied in Chapter 6, where the stability conditions for a Generalized Sail are identified and the control capabilities of two Solar Sail based spacecraft are analyzed.

Part II leaves the study of *Artificial Equilibrium Point*s and deals with the concept of *displaced frozen orbits*, obtained in a three-body system, when the continuous propulsive acceleration provided by a Solar Sail is also considered .

Part I

Artificial Equilibrium Points

Chapter 2

Restricted Three-Body Problem and Generalized Sail Model

In this chapter two goals are pursued. Firstly, some useful concepts related to the *Restricted Three-Body Problem* are recalled, with the aim to create the background necessary to introduce the succeeding work. Secondly, the innovative concept of *Generalized Sail* is introduced. The latter is used to show that, under suitable assumptions, the propulsive acceleration of spacecraft can be described within a general mathematical model that encompasses the behavior of different continuous-thrust propulsion systems, like Solar Sails, Electric Sails and Electric Thrusters.

2.1 Restricted Three-Body Problem

The *Restricted Three-Body Problem* (R3BP) is a mathematical model that deals with the gravitational interaction among three bodies when one body has negligible mass compared to the other two. Such a problem occupies a central place in celestial mechanics and astrodynamics, because several aspects of the motion of spacecraft and celestial bodies can be understood only by leaving the Keplerian model and using a three-body model. Even though simple and intuitive in its form, such a transition is actually a complex task, and the efforts of great mathematicians, during the past 250 years, have not yet given a complete analytical solution nor a trajectory equation, as for the two-body case.

Newton was the first who studied and obtained some approximate results for the general problem of three bodies, devoting much time to the Moon's motion. The first important contributions, however, came from Euler and Lagrange in 1772. Later on, other important results were obtained by Jacobi and Hill, and the studies were continued by Poincaré, Levi-Civita, Birkhoff and other important contributors to date.

2.1.1 Elliptic Restricted Three-Body Problem

Consider the motion of a small body S (e.g., a spacecraft or a small celestial body) under the gravitational effects of two celestial bodies P_1 and P_2, with masses m_1 and $m_2 \leq m_1$. The motion of the two celestial bodies (also referred to as attractors) is not affected by the small body, and, therefore, P_1 and P_2 move with respect to their relative center of mass C on trajectories that are solution of the two-body problem. As a consequence, the trajectories are on a plane that is fixed in a inertial reference frame, and they can be either both open (parabolic or hyperbolic) or both closed (elliptic or circular).

Assuming that such trajectories are closed, from an observer on P_1 (P_2) the orbit of P_2 (P_1) is an ellipse of semimajor axis a and eccentricity e, see Fig. 2.1, and the problem is referred to as *Elliptic Restricted Three-Body Problem* (ER3BP) or *Circular Restricted Three-Body Problem* (CR3BP), according to whether $e \neq 0$ or $e = 0$.

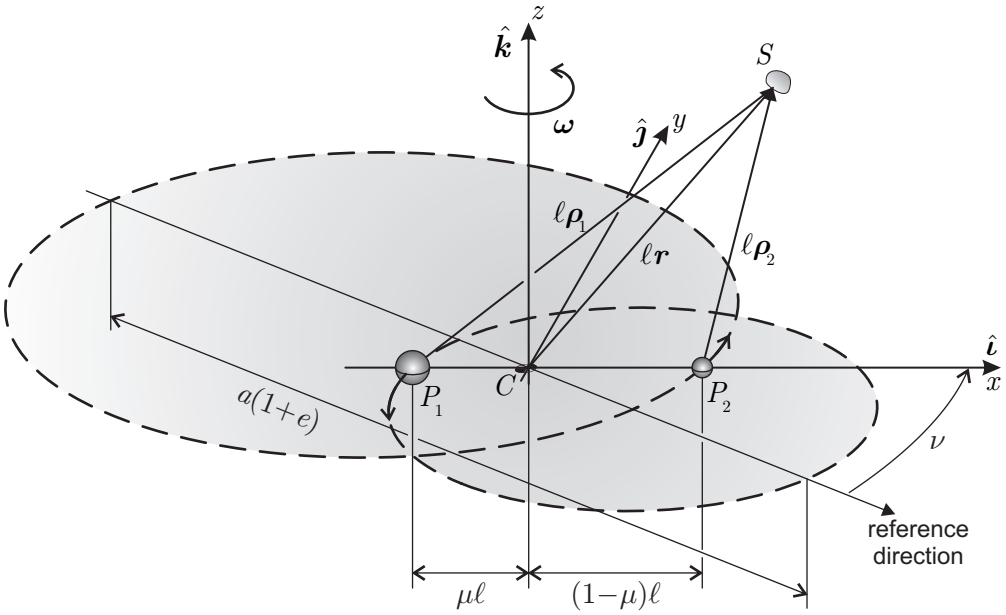

Figure 2.1: Geometry of the Elliptic Restricted Three-Body Problem.

Denoting with ν the angular coordinate (positive towards P_2) of the segment P_1P_2, measured on the plane of motion of the two attractors, and calculated from the direction given by the axis pointing from P_1 to the pericenter of the orbit of P_2, the time-dependent distance ℓ between the two celestial bodies is [11]

$$\ell = a(1 - e^2)g \tag{2.1}$$

with

$$g \triangleq \frac{1}{1 + e\cos\nu} > 0 \tag{2.2}$$

It is useful to introduce a rotating reference frame $\mathcal{T}(C;\, x,\, y,\, z)$, with unit vectors $\hat{\boldsymbol{\imath}}$, $\hat{\boldsymbol{\jmath}}$ and $\hat{\boldsymbol{k}}$, where $\hat{\boldsymbol{\imath}}$ points toward P_2 at any instant of time and $\hat{\boldsymbol{k}}$ is in the direction of the constant angular momentum of the two celestial bodies, see Fig. 2.1. The angular velocity $\boldsymbol{\omega} \triangleq \omega\hat{\boldsymbol{k}}$ of $\mathcal{T}$ with respect to an inertial frame, where $\omega = \mathrm{d}\nu/\mathrm{d}t$, is given by the solution of the two body problem as

$$\omega = \frac{\sqrt{a(1-e^2)\,G(m_1+m_2)}}{\ell^2} \tag{2.3}$$

where G is the universal gravitational constant.

In the rotating reference frame $\mathcal{T}$, the vectorial equation of motion of the small body S is [11]

$$\frac{\mathrm{d}^2(\ell\boldsymbol{r})}{\mathrm{d}t} + 2\boldsymbol{\omega}\times\frac{\mathrm{d}(\ell\boldsymbol{r})}{\mathrm{d}t} + \ell\frac{\mathrm{d}\boldsymbol{\omega}}{\mathrm{d}t}\times\boldsymbol{r} + \ell\boldsymbol{\omega}\times(\boldsymbol{\omega}\times\boldsymbol{r}) = -\frac{Gm_1}{\ell^2\rho_1^3}\boldsymbol{\rho}_1 - \frac{Gm_2}{\ell^2\rho_2^3}\boldsymbol{\rho}_2 \tag{2.4}$$

where $\boldsymbol{\rho}_1$, $\boldsymbol{\rho}_2$, and $\boldsymbol{r}$ (with $\rho_1 \triangleq \|\boldsymbol{\rho}_1\|$ and $\rho_2 \triangleq \|\boldsymbol{\rho}_2\|$) are the dimensionless position vectors of S with respect to P_1, P_2 and C, respectively.

Using the angular coordinate ν as the independent variable, the equation motion in Eq. (2.4) can be put in dimensionless form (see Appendix A)

$$\boldsymbol{r}'' + 2\hat{\boldsymbol{k}}\times\boldsymbol{r}' = g\left[-\frac{1-\mu}{\rho_1^3}\boldsymbol{\rho}_1 - \frac{\mu}{\rho_2^3}\boldsymbol{\rho}_2 - \hat{\boldsymbol{k}}\times\left(\hat{\boldsymbol{k}}\times\boldsymbol{r}\right) - e\cos\nu\left(\boldsymbol{r}\cdot\hat{\boldsymbol{k}}\right)\hat{\boldsymbol{k}}\right] \tag{2.5}$$

where the prime symbol denotes a derivative taken with respect to ν and $\mu \triangleq m_2/(m_1+m_2) \in (0,\ 0.5]$ is the dimensionless mass of P_2, which univocally identifies the positions of P_1 and P_2 in the frame $\mathcal{T}$ at any instant of time, see Fig. 2.1.

It is necessary to emphasize the particular meaning of the dimensionless equation (2.5). In fact, using the variable distance ℓ as the unit of distance, Eq. (2.5) describes the motion of the body S in a particular rotating coordinate system $\mathcal{T}_P(C;\, x/\ell,\, y/\ell,\, z/\ell)$, which is *pulsating* synchronously to the distance ℓ. Note that, for example, in the pulsating coordinate system the position of the two celestial bodies is fixed, whereas they actually oscillate (*pulsate*) when seen by an observer in the frame $\mathcal{T}$.

Lagrangian Points

The Lagrangian Points (also referred to as Libration Points or, simply, Equilibrium Points) are defined as the equilibrium solution of equation (2.5).

Enforcing the stationary conditions

$$\boldsymbol{r}'' = 0, \quad \boldsymbol{r}' = 0 \tag{2.6}$$

into Eq. (2.5), the Lagrangian Points are obtained as solution of

$$-\frac{1-\mu}{\rho_1^3}\boldsymbol{\rho}_1 - \frac{\mu}{\rho_2^3}\boldsymbol{\rho}_2 - \hat{\boldsymbol{k}} \times \left(\hat{\boldsymbol{k}} \times \boldsymbol{r}\right) - e\cos\nu\left(\boldsymbol{r}\cdot\hat{\boldsymbol{k}}\right)\hat{\boldsymbol{k}} = 0 \tag{2.7}$$

Equation (2.7) admits five solutions (denoted as L_i with i from 1 to 5) all belonging to the plane of motion of the two attractors (that is, where $\boldsymbol{r}\cdot\hat{\boldsymbol{k}} = 0$), see Fig. 2.2(a). The points L_1, L_2 and L_3, aligned with the segment P_1P_2, are

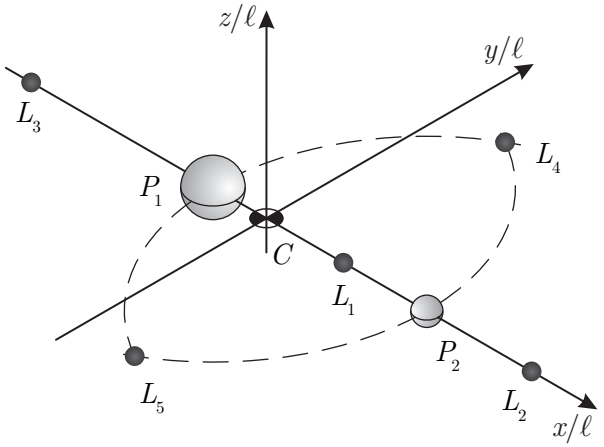

(a) Pulsating rotating frame.

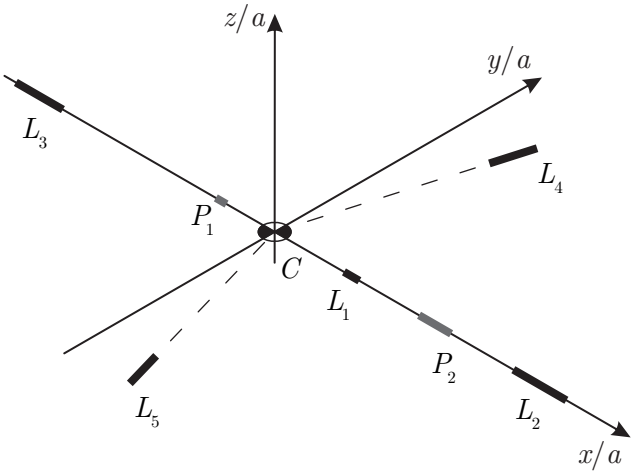

(b) Rotating frame.

Figure 2.2: Position of the Lagrangian Points in the classic ER3BP when $e = 0.1$ and $\mu = 0.25$.

called *collinear*, while the points L_4 and L_5, at a dimensionless distance equal to one from P_1 to P_2, are called *equilateral*. Note that a generic position $\boldsymbol{r}$ corresponds to the vector $\ell\boldsymbol{r}$ in the rotating frame. Therefore, an equilibrium point $\boldsymbol{r}_0$

of Eq. (2.5) is actually a segment of length $2ae\|\boldsymbol{r}_0\|$, parallel to the direction of $\boldsymbol{r}_0$, along which the small body S oscillates back and forth with a period $2\pi/\omega$, according to the length variation of the segment P_1P_2, see Fig. 2.2(b).

Stability of Lagrangian Points

The equation of motion (2.5) can be linearized around the Lagrangian Points. The resulting equation gives information about the linear stability[1] and the motion in the proximity of the equilibrium points [11].

The stability analysis is performed by means of the Floquet theory [12, 13], in the general case $e \neq 0$. The results of such an analysis show that the collinear points are always unstable, whereas the triangular points can be stable for some pairs (μ, e), see Fig. 2.3.

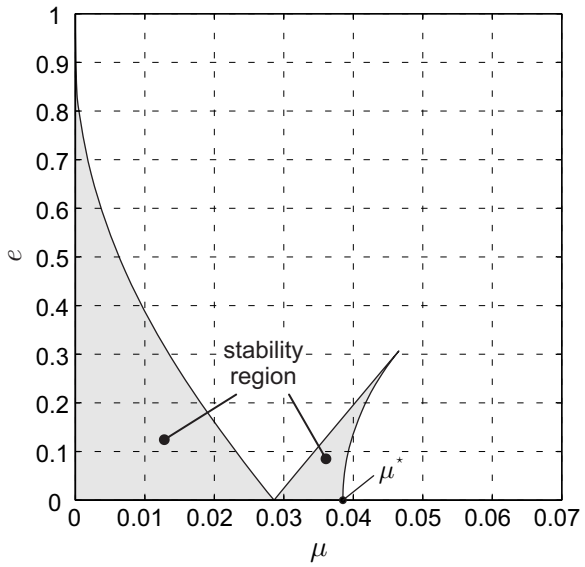

Figure 2.3: Linear Stability of the equilateral points in the ER3BP.

2.1.2 Circular Restricted Three-Body Problem

A particular case of the ER3BP is when the eccentricity e is zero, thus corresponding to circular orbits of the two celestial bodies, see Fig. 2.4. In such a case the problem is called *Circular Restricted Three-Body Problem*.

With the condition $e = 0$, Eqs. (2.1) and (2.3) state that ℓ and ω are constant. Defined

$$l \triangleq \ell|_{e=0} \tag{2.8}$$

[1] Note that a linear analysis provides necessary conditions for stability and sufficient conditions for instability.

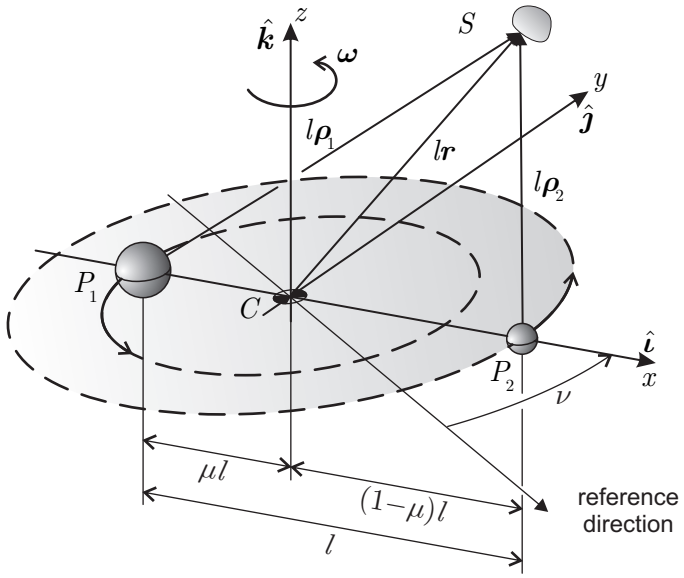

Figure 2.4: Geometry of the Circular Restricted Three-Body Problem.

the constant angular velocity is

$$\omega = \sqrt{\frac{G(m_1 + m_2)}{l^3}} \tag{2.9}$$

From Eq. (2.5), the dimensionless equation of motion reduces to [11, 14]

$$\boldsymbol{r}'' + 2\hat{\boldsymbol{k}} \times \boldsymbol{r}' = -\frac{1-\mu}{\rho_1^3}\boldsymbol{\rho}_1 - \frac{\mu}{\rho_2^3}\boldsymbol{\rho}_2 - \hat{\boldsymbol{k}} \times \left(\hat{\boldsymbol{k}} \times \boldsymbol{r}\right) \tag{2.10}$$

where the prime symbol is again the derivative with respect to the angular variable ν, measured from the reference direction defined by the direction of the segment P_1P_2 at the initial time instant, see Fig. 2.4.

Note that, Eq. (2.10) can be written in compact form as

$$\boldsymbol{r}'' + 2\hat{\boldsymbol{k}} \times \boldsymbol{r}' = \nabla J \tag{2.11}$$

where

$$J \triangleq \frac{1-\mu}{\rho_1} + \frac{\mu}{\rho_2} + \frac{1}{2}\left(\hat{\boldsymbol{k}} \times \boldsymbol{r}\right) \cdot \left(\hat{\boldsymbol{k}} \times \boldsymbol{r}\right) \tag{2.12}$$

is the opposite of the specific potential energy of the small body S. Taking the dot product of $\boldsymbol{r}'$ with Eq. (2.11), it is easily shown that a first integral of motion of the CR3BP is given by the *Jacobi integral* [11]

$$\boldsymbol{r}' \cdot \boldsymbol{r}' - 2J = \mathcal{C} \tag{2.13}$$

with $\mathcal{C}$ a constant of integration, referred to as *Jacobi constant*.

In analogy to the elliptic case, the Lagrangian Points are found as the equilibrium solution of Eq. (2.10), thus solving the equation

$$-\frac{1-\mu}{\rho_1^3}\boldsymbol{\rho}_1 - \frac{\mu}{\rho_2^3}\boldsymbol{\rho}_2 - \hat{\boldsymbol{k}} \times \left(\hat{\boldsymbol{k}} \times \boldsymbol{r}\right) = 0 \tag{2.14}$$

which is obtained enforcing the stationary conditions $\boldsymbol{r}'' = 0$ and $\boldsymbol{r}' = 0$.

The previous equation has the same formal solutions of Eq. (2.7), therefore the Lagrangian Points in the circular problem are the same of Fig. 2.2(a), where the variable length ℓ has now to be replaced with the constant length l.

The stability of the equilibrium positions can be studied [11,14] by linearizing Eq. (2.14) around the equilibrium points. Differently from the elliptic case, the linearized system results in a system of autonomous equations, and an analytical approach is possible for investigating the stability. The result is that the three collinear points are always unstable, whereas the equilateral points are stable provided that the mass parameter μ is small enough to satisfy $\mu < \mu^\star \approx 0.03852$ [11], see Fig. 2.3 when $e = 0$.

2.1.3 Artificial Equilibrium Points

When the small body S in Figs. 2.1 and 2.4 is a spacecraft equipped with a suitable continuous-thrust propulsion system, there is the possibility of modifying the position of the equilibrium points both in the ER3BP and in the CR3BP with respect to their classical (i.e., zero thrust) positions. These new displaced points are usually referred to as *Artificial Equilibrium Point*s (AEPs), in accordance with the nomenclature introduced by Dusek [15] and succeedingly adopted by many authors [8, 16, 17].

2.2 Generalized Sail

The *Generalized Sail* is a mathematical model useful for describing the propulsive acceleration of a spacecraft whose propulsion system provides a continuous and purely radial thrust with respect to some reference celestial body, see Fig. 2.5.

Assume that the magnitude of the propulsive acceleration of a spacecraft can be written as the product of two functions, one at most time dependent (a_c) and the other at most exponentially varying with the distance ρ from a reference celestial body. The purely radial propulsive acceleration is therefore written as

$$\boldsymbol{a}_\mathrm{P} = a_c \left(\frac{d}{\rho}\right)^\eta \hat{\boldsymbol{\rho}} \tag{2.15}$$

where d is a reference distance at which the so-called characteristic acceleration a_c is measured, η is a coefficient depending on the propulsion system type, while $\hat{\boldsymbol{\rho}}$ is the unit vector, oriented in the radial outward direction with respect to the celestial body.

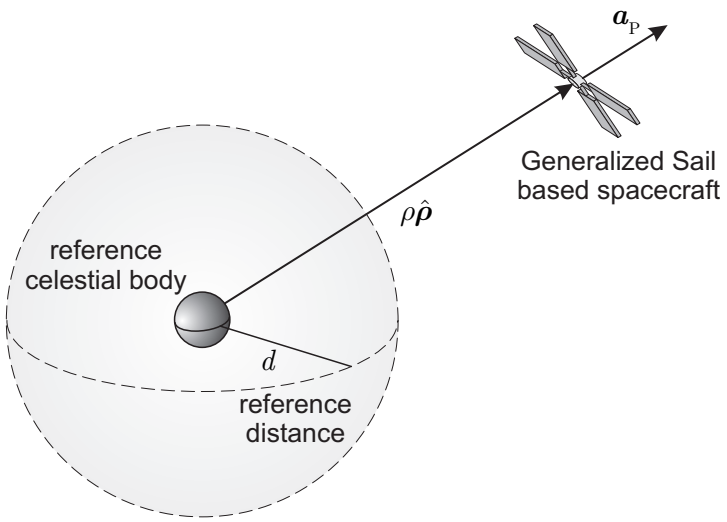

Figure 2.5: Generalized Sail.

Any propulsion system capable of generating an acceleration in the form of Eq. (2.15) will be referred to as *Generalized Sail*. The reason for the name is that Eq. (2.15) encompasses different types of propulsion systems (either currently available or under development), by simply specializing the value of η (see Table 2.1), when the reference celestial body coincides with the Sun. For example,

η	Propulsion System	Note
0	- M2P2 - Electric Thruster	- Power source independent of Sun-spacecraft distance
1	- E-Sail	
4/3	- MagSail	- Plasma Fluid Model [18]
2	- Solar Sail - MagSail - Electric Thruster	 - Particle Model [18] - Ideal Solar Array
η	- Electric Thruster	- Value depending on the solar array characteristics

Table 2.1: Summary of propulsion systems included in the Generalized Sail model.

$\eta = 2$ describes the acceleration provided by a Solar Sail [19]. The cases $\eta = 4/3$ or $\eta = 2$ (depending on the size of the magnetosphere around the spacecraft [18])

describe the acceleration of a MagSail based spacecraft, while $\eta = 1$ corresponds to an E-Sail based spacecraft [20]. Furthermore, the case $\eta = 0$ is representative of a propulsive acceleration that is independent of the distance from the reference body. Such a situation is consistent either with a Mini-Magnetospheric Plasma Thruster (M2P2, see Ref. [21]) or an Electric Thruster, when the power source is independent of the Sun-spacecraft distance, as in a nuclear powered system[2].

Note, however, that an Electric Thruster can also be characterized by a coefficient $\eta \neq 0$. In fact, the propulsive acceleration of a spacecraft equipped with an Electric Thruster of constant specific impulse is proportional to the input power P of the thruster, with coefficient of proportionality depending only on the time by means of the variable mass of the spacecraft and of the variable efficiency of the thruster [24]. For the case of nuclear-powered spacecraft, the input power is roughly constant in time and space, therefore, Eq. (2.15) with $\eta = 0$ describes the propulsive acceleration of such a spacecraft. In case of solar-powered spacecraft, in which the electric power is supplied by solar arrays, the maximum input power P is a function of the distance from the Sun [25, 26], but also depends on the flight time due to the solar cells degradation [27, 28]. If the time degradation of solar cells is neglected, the maximum input power P can be described through a rational function of ρ [25], and, to a first order approximation, it can be written as

$$P = \frac{P_r}{\rho^\eta} \tag{2.16}$$

where P_r is a reference value that usually coincides with the maximum power generated at the reference distance d from the Sun, and η depends on the numerical coefficients that model the solar cells performance variation with the Sun-spacecraft distance. In the ideal case, when the dependence of P from ρ is due only to the radial variation of the solar intensity, the exponent in Eq. (2.16) becomes $\eta = 2$, and an inverse square law of P with the Sun-spacecraft distance is obtained. In general, the value of η depends on the solar array characteristics and on the range of distance from the Sun considered. For example, with $\eta \approx 0.9$ for $\rho \in [0.7, 1.15]\,\mathrm{AU}$ or $\eta \approx 1.6$ for $\rho \in [0.9, 1.5]\,\mathrm{AU}$, Eq. (2.16) approximates the result of Sauer [25] with a percentage error of less than 6%.

2.2.1 Lightness Number

The characteristic acceleration a_c is a dimensional parameter that quantifies the performance of the propulsion system. It is closely related to the total mass of the spacecraft and to other parameters specific of the type of propulsion system considered.

[2] This happens, for example, when the power subsystem is represented by a radio-isotope thermoelectric generator [22, 23].

Often, especially when a dimensionless analysis is performed, a new parameter is conveniently introduced, which is related to the characteristic acceleration. This parameter is defined as the ratio of a_c to the gravitational acceleration exerted by the reference celestial body at the reference distance d, that is

$$\beta \triangleq \frac{a_c}{GM/d^2} \tag{2.17}$$

where M is the mass of the celestial body.

When such a new parameter is put into Eq. (2.15), the propulsive acceleration provided by a Generalized Sail is written as

$$\boldsymbol{a}_{\mathrm{P}} = \beta \frac{GM}{d^2} \left(\frac{d}{\rho}\right)^{\eta} \hat{\boldsymbol{\rho}} \tag{2.18}$$

Following the nomenclature usually adopted for Solar Sails [19], β will be referred to as (*sail*) *lightness number*.

Chapter 3

Artificial Equilibrium Points for a Generalized Sail in the Circular Restricted Three-Body Problem

This chapter deals with a new approach to the study of *Artificial Equilibrium Point*s in the *Circular Restricted Three-Body Problem* for spacecraft equipped with a *Generalized Sail*. The existence and stability of Artificial Equilibrium Points are investigated. It is shown that three different families of equilibrium points exist, and their locus is geometrically described by varying the value of the lightness number. The stability is also discussed by means of suitable stability maps. The resulting model is useful to compare the performance required by a given propulsion system to create and maintain an Artificial Equilibrium Point.

3.1 Introduction

The problem of describing the location of AEPs in the CR3BP and of investigating their stability properties has been addressed by several authors. In particular, during the two decades from 1970 to 1990, following the pioneering work of Radzievskii [29], the effects of the thrust due to the radiation pressure on the CR3BP have been thoroughly studied [30–34]. An important result is that seven equilibrium points exist if one of the massive bodies is luminous, because this problem is equivalent to consider a Solar Sail, whose thrust direction is fixed and radially directed with respect to the luminous body. Subsequently, different studies regarding the use of Solar Sails [35–37] or low-thrust systems [16] have been carried out, which proved the existence of infinite equilibrium surfaces depending on the magnitude of the propulsive acceleration. However, only a subset of the potentially achievable AEPs turns out to be stable and, as such, could be exploited by a spacecraft without the use of a suitable control system. The

topology of such subset of stable AEPs is strictly dependent on the propulsion system type employed by the spacecraft. For example, as was recently pointed out by Bombardelli and Peláez [17], if the available propulsive acceleration is low, in case of constant continuous acceleration, the stable AEPs are confined to a very restricted region around the classical Lagrange points.

3.2 Mathematical Model

Consider a CR3BP where a spacecraft S moves under the gravitational effects of two celestial bodies P_1 e P_2, both covering circular orbits about their centre of mass C, see Fig. 3.1. The rotating frame $\mathcal{T}(C;\, x,\, y,\, z)$, with unit vectors $\hat{\boldsymbol{\imath}}$, $\hat{\boldsymbol{\jmath}}$ and $\hat{\boldsymbol{k}}$ is also shown in Fig. 3.1.

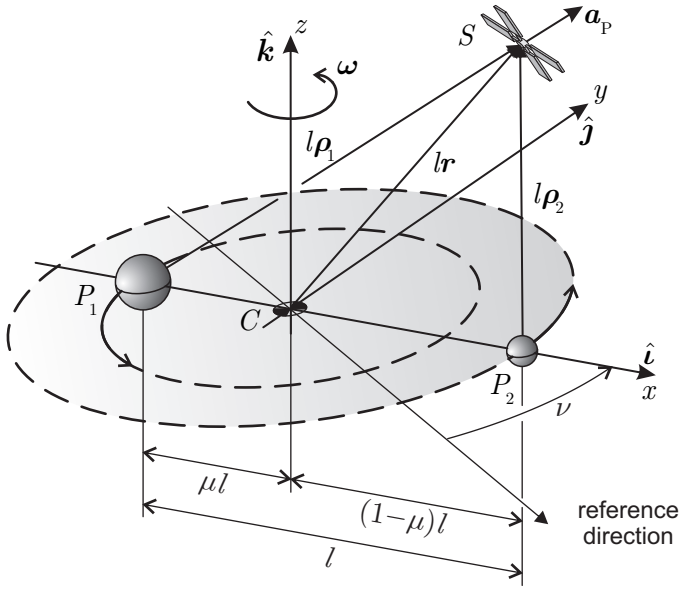

Figure 3.1: Generalized Sail based spacecraft in the Circular Restricted Three-Body Problem.

Assume that the spacecraft is equipped with a Generalized Sail. If P_1 and l are used as reference celestial body and reference distance, respectively, then the propulsive acceleration $\boldsymbol{a}_{\mathrm{P}}$ is parallel to $\boldsymbol{\rho}_1$ and is given by the following relationship, obtained from Eq. (2.18)

$$\boldsymbol{a}_{\mathrm{P}} = \beta \frac{G m_1}{l^2 \rho_1^{\eta}} \hat{\boldsymbol{\rho}}_1 \tag{3.1}$$

where $\hat{\boldsymbol{\rho}}_1 = \boldsymbol{\rho}_1 / ||\boldsymbol{\rho}_1||$.

From Appendix A, a dimensionless form of the equation of motion for the

spacecraft can be written as follows

$$\boldsymbol{r}'' + 2\hat{\boldsymbol{k}} \times \boldsymbol{r}' = -\frac{1-\mu}{\rho_1^3}\boldsymbol{\rho}_1 - \frac{\mu}{\rho_2^3}\boldsymbol{\rho}_2 + \beta\frac{1-\mu}{\rho_1^{\eta+1}}\boldsymbol{\rho}_1 - \hat{\boldsymbol{k}} \times \left(\hat{\boldsymbol{k}} \times \boldsymbol{r}\right) \tag{3.2}$$

Note that, according to Fig. 3.1

$$\boldsymbol{r} = \boldsymbol{\rho}_1 - \mu\,\hat{\boldsymbol{\imath}} \qquad , \qquad \boldsymbol{\rho}_2 = \boldsymbol{\rho}_1 - \hat{\boldsymbol{\imath}} \tag{3.3}$$

As a result, Eq. (3.2) can be rearranged and written as a function of the vector $\boldsymbol{\rho}_1$ only.

Notably, the equations of motion (3.2) can be written in compact form as

$$\boldsymbol{r}'' + 2\hat{\boldsymbol{k}} \times \boldsymbol{r}' = \nabla J^\star \tag{3.4}$$

where $J^\star \triangleq J + \Psi$, and J is the sum of the gravitational and centrifugal potential, see Eq. (2.12), while Ψ represents the potential due to the propulsive acceleration, that is

$$\Psi = \begin{cases} \dfrac{\beta}{1-\eta}\,\dfrac{1-\mu}{\rho_1^{\eta-1}} & \text{if } \eta \neq 1 \\ \beta(1-\mu)\ln\rho_1 & \text{if } \eta = 1 \end{cases} \tag{3.5}$$

Paralleling to Szebehely [11], it is possible to obtain a generalization of the Jacobi integral in Eq. (2.13) for a Generalized Sail based spacecraft as

$$\boldsymbol{r}' \cdot \boldsymbol{r}' - 2\,J^\star = \mathcal{C}_1 \tag{3.6}$$

where $\mathcal{C}_1$ is an integration constant.

3.3 Artificial Equilibrium Points

The positions of AEPs are obtained by enforcing the equilibrium conditions $\boldsymbol{r}'' = 0$ and $\boldsymbol{r}' = 0$ in Eq. (3.2), thus solving the equation

$$-\frac{1-\mu}{\rho_1^3}\boldsymbol{\rho}_1 - \frac{\mu}{\rho_2^3}\boldsymbol{\rho}_2 + \beta\frac{1-\mu}{\rho_1^{\eta+1}}\boldsymbol{\rho}_1 - \hat{\boldsymbol{k}} \times \left(\hat{\boldsymbol{k}} \times \boldsymbol{r}\right) = 0 \tag{3.7}$$

Using Eq. (3.3), the previous equation can be expressed in a more compact form as

$$d_k\,\hat{\boldsymbol{k}} + d_i\,\hat{\boldsymbol{\imath}} = d_\rho\,\hat{\boldsymbol{\rho}}_1 \tag{3.8}$$

where

$$d_k \triangleq \boldsymbol{\rho}_1 \cdot \hat{\boldsymbol{k}} \quad , \quad d_i \triangleq \mu\left(1 - \frac{1}{\rho_2^3}\right) \quad , \quad d_\rho \triangleq \rho_1 - \frac{1-\mu}{\rho_1^2} - \frac{\mu\,\rho_1}{\rho_2^3} + \beta\frac{1-\mu}{\rho_1^\eta} \tag{3.9}$$

An analysis of Eq. (3.8) provides the loci of AEPs (see Table 3.1 and Fig. 3.2) and the corresponding *constant* value of the lightness number β required to maintain such equilibrium points.

In what follows, the AEPs will be distinguished according to their different geometrical positions in: *triangular*, *collinear* and *displaced* points.

Conditions for Eq. (3.8)			Locus equations	Locus name
$d_k = 0$	$d_i = 0$	$d_\rho = 0$	$\boldsymbol{\rho}_1 \cdot \hat{\boldsymbol{k}} = 0,\ \rho_2 = 1$	triangular points
		$d_\rho \neq 0$	not possible	
	$d_i \neq 0$	$d_\rho = 0$	not possible	
		$d_\rho \neq 0$	$\boldsymbol{\rho}_1 \parallel \hat{\boldsymbol{\imath}}$	collinear points
$d_k \neq 0$	$d_i = 0$	$d_\rho = 0$	not possible	
		$d_\rho \neq 0$	not possible	
	$d_i \neq 0$	$d_\rho = 0$	not possible	
		$d_\rho \neq 0$	$\boldsymbol{\rho}_1 \cdot \hat{\boldsymbol{\jmath}} = 0,\ \frac{\mu}{\rho_2^3} = \mu - \boldsymbol{\rho}_1 \cdot \hat{\boldsymbol{\imath}}$	displaced points

Table 3.1: Summary of AEPs loci in the CR3BP (see also Fig. 3.2).

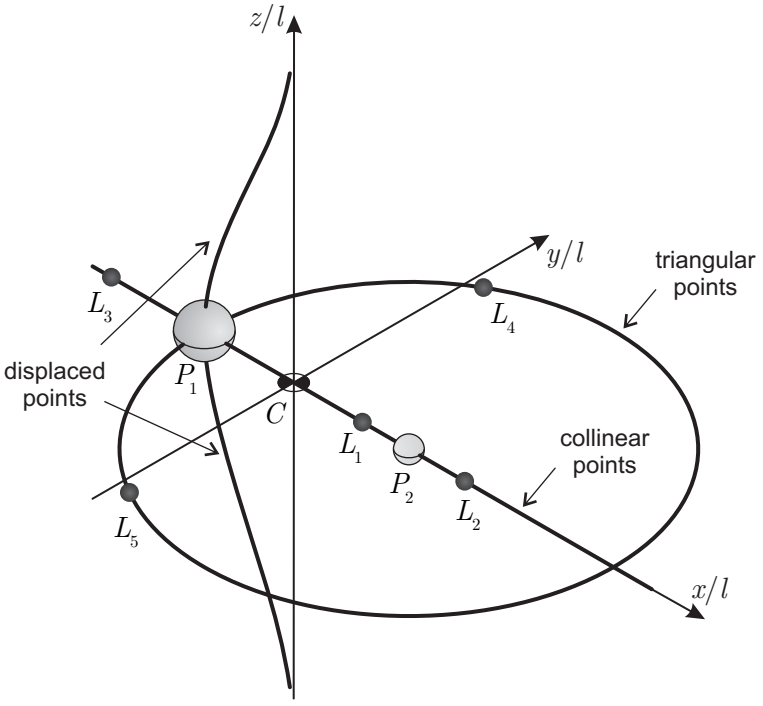

Figure 3.2: Nomenclature for AEPs loci in the CR3BP (see also Table 3.1).

3.3.1 Triangular Points

The triangular points are obtained by looking for the values of β, ρ_2, and $\boldsymbol{\rho}_1$ in correspondence of which the coefficients d_k, d_i, and d_ρ of Eq. (3.9) are all equal

to zero, that is

$$\boldsymbol{\rho}_1 \cdot \hat{\boldsymbol{k}} = 0 \quad , \quad \rho_2 = 1 \quad , \quad \beta = \rho_1^{\eta+1} \left(\frac{1}{\rho_1^3} - 1 \right) \tag{3.10}$$

As a result, the locus of the triangular AEPs is constituted by a circle, with center P_2 and radius l, belonging to the (x, y) plane (see Fig. 3.2). Note that the name triangular points comes from the fact that in the absence of any thrust ($\beta = 0$), Eq. (3.10) provides $\rho_1 \equiv \rho_2 = 1$, which corresponds to the position of the classical equilateral points $\rho_{1_{L_4}} \equiv \rho_{2_{L_4}} = 1$, and $\rho_{1_{L_5}} \equiv \rho_{2_{L_5}} = 1$, see Section 2.1.2.

For a given point on the locus, that is, for a given value of $\rho_1 \in (0, 2]$, the required constant value of β can be calculated using the third relation of Eq. (3.10). The shape of β as a function of the distance $\rho_1 \in (0, 2]$ and of the coefficient η is qualitatively shown in Fig. 3.3.

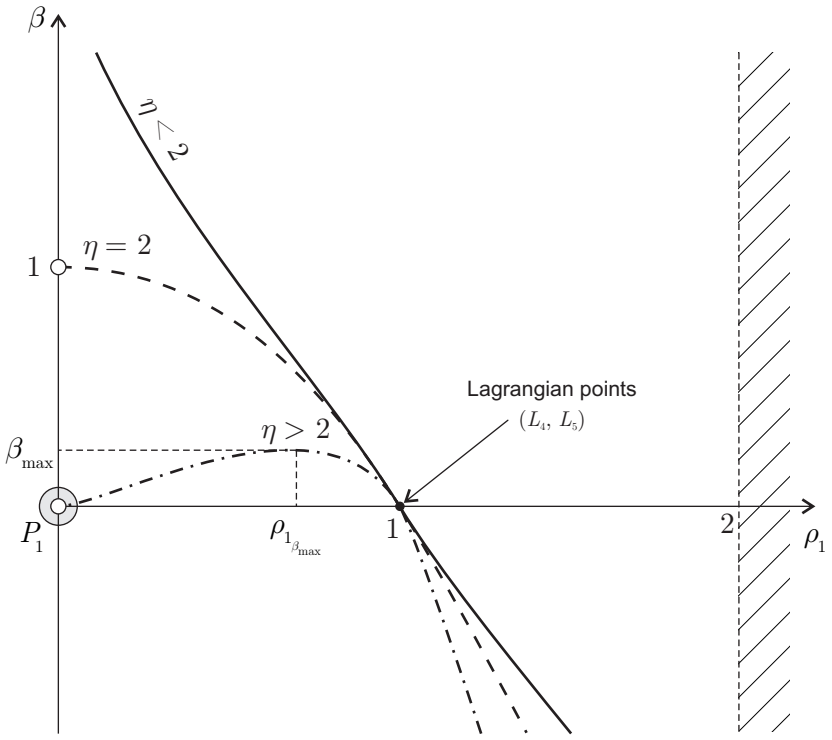

Figure 3.3: Lightness number β as a function of ρ_1 and η for triangular points.

Note that for a fixed distance $\rho_1 < 1$ (> 1), the parameter η must be increased (decreased) to reduce the value of $|\beta|$ necessary to maintain such an AEP. Moreover, for a fixed value of $\eta > 2$ the contour line $\beta = \beta(\rho_1, \eta)$ presents a maximum with coordinates $(\rho_{1_{\beta_{\max}}}, \beta_{\max})$, where

$$\rho_{1_{\beta_{\max}}} = \sqrt[3]{\frac{\eta - 2}{\eta + 1}} \quad , \quad \beta_{\max} = 3 \sqrt[3]{\frac{(\eta - 2)^{\eta-2}}{(\eta + 1)^{\eta+1}}} \tag{3.11}$$

In particular, when $\eta = 2$ and $\beta > 0$, that is, when the propulsion system is constituted by either a Solar or a Magnetic Sail (see Table 2.1), according to Simmons et al. [33], Eq. (3.11) states that β takes its maximum value ($\beta = 1$) as ρ_1 tends to zero. Clearly such a condition is not physically acceptable[1] because the corresponding AEP would coincide with the attractor P_1.

The presence of a maximum value of the lightness number β implies that, for a given value of $\beta > 0$, there exist either two AEPs (if $\eta \leq 2$) or four AEPs (if $\eta > 2$). These points are at symmetrical positions with respect to the x-axis of the synodic reference frame, as is shown in Fig. 3.4. This figure also illustrates the variation of $|\beta|$ on the locus of triangular points in the three cases $\eta < 2$, $\eta = 2$, and $\eta > 2$.

3.3.2 Collinear Points

The collinear points are obtained from Eq. (3.8) when $d_k = 0$, but $d_i \neq 0$ and $d_\rho \neq 0$. The condition $d_k = 0$ in Eq. (3.8) states $d_i \hat{\boldsymbol{\imath}} = d_\rho \hat{\boldsymbol{\rho}}_1$, which implies that the directions of $\hat{\boldsymbol{\rho}}_1$ and $\hat{\boldsymbol{\imath}}$ are parallel. Accordingly, the AEPs belong to the x-axis, thus explaining the name collinear, see Fig. 3.2. Therefore, the collinear points are such that

$$\hat{\boldsymbol{\rho}}_1 \cdot \hat{\boldsymbol{\imath}} = \pm 1 \quad , \quad d_\rho = d_i \, \hat{\boldsymbol{\rho}}_1 \cdot \hat{\boldsymbol{\imath}} \tag{3.12}$$

With $\hat{\boldsymbol{\rho}}_1$ parallel to $\hat{\boldsymbol{\imath}}$, Eq. (3.3) states that $\rho_2 = \|\rho_1 \, \hat{\boldsymbol{\rho}}_1 \cdot \hat{\boldsymbol{\imath}} - 1\|$. The latter relationship can be substituted into Eq. (3.12) to find the lightness number required to obtain the collinear AEPs. After some algebraic manipulations the result is

$$\beta = \frac{\mu \rho_1^\eta}{(1-\mu)\hat{\boldsymbol{\rho}}_1 \cdot \hat{\boldsymbol{\imath}}} \left(1 + \frac{\rho_1 \, \hat{\boldsymbol{\rho}}_1 \cdot \hat{\boldsymbol{\imath}} - 1}{\|\rho_1 \, \hat{\boldsymbol{\rho}}_1 \cdot \hat{\boldsymbol{\imath}} - 1\|^3} \right) + \rho_1^{\eta-2} - \frac{\rho_1^{\eta+1}}{1-\mu} \tag{3.13}$$

As in the triangular points case, the condition $\beta = 0$ in Eq. (3.13) provides the position of the three classical collinear Lagrange points $\rho_{1_{L_1}}$, $\rho_{1_{L_2}}$, and $\rho_{1_{L_3}}$. Recall that L_1 is between the two attractors, L_2 is placed on the positive x-axis beyond P_2, and L_3 is on the left of P_1. Based on this nomenclature, it is useful to distinguish the collinear points according to their position with respect to the celestial bodies, as shown in Fig. 3.5

The variation of β with ρ_1 for L_3-type points (the points in which $\hat{\boldsymbol{\rho}}_1 \cdot \hat{\boldsymbol{\imath}} = -1$) is qualitatively shown in Fig. 3.6(a), while Fig. 3.6(b) illustrates the corresponding variation of the AEPs position as a function of β. Figure 3.6(a) shows that the contour curves with $\eta > 2$ take an absolute maximum whose value decreases as η is increased. Once again, when $\eta = 2$ the maximum is not attainable because it would coincide with the attractor P_1. If $\eta > 2$ and $\beta \in (0, \beta_{\max})$ two AEPs are obtained, whose position along the x-axis is between P_1 and the classical

[1] In the following those unattainable equilibrium points will be marked in the figures with a white circle "○".

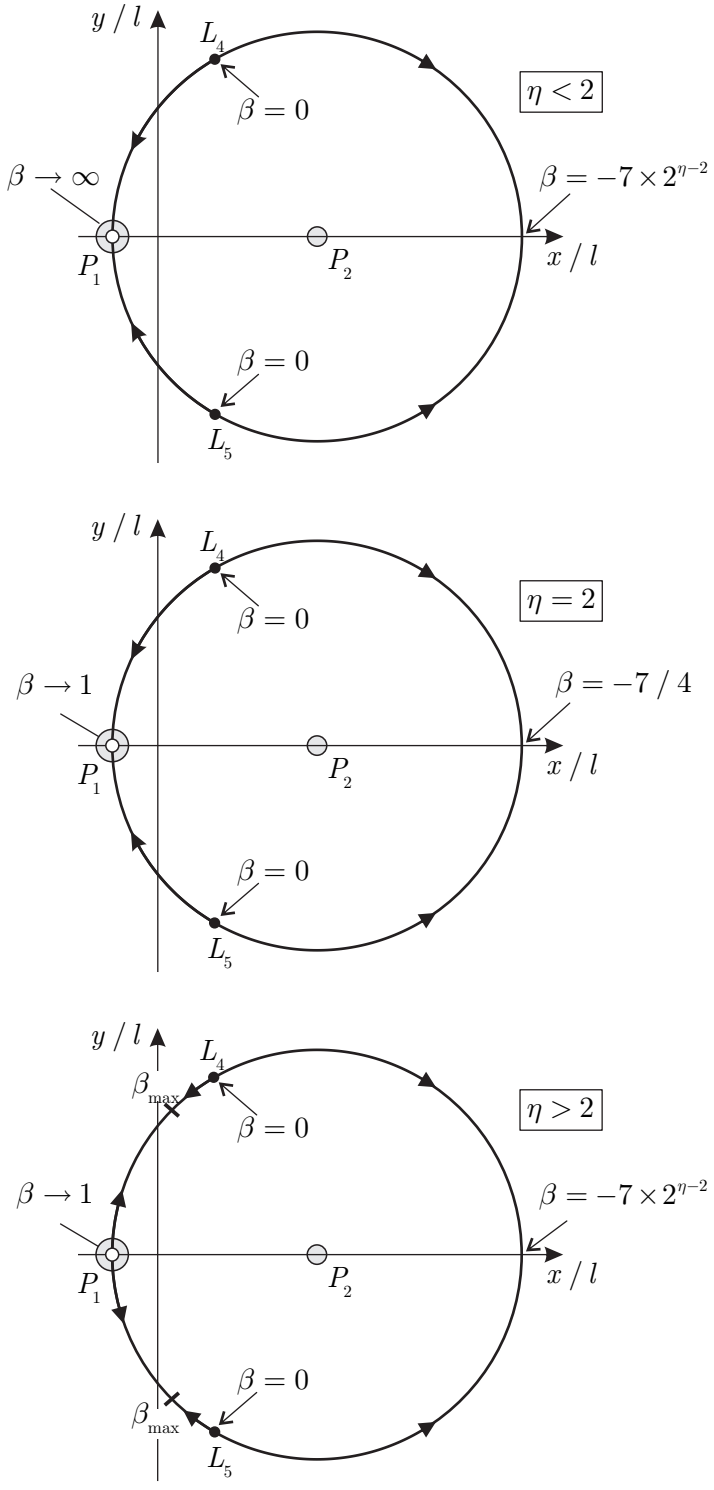

Figure 3.4: Triangular equilibrium points locus (arrows indicate a $|\beta|$ increase).

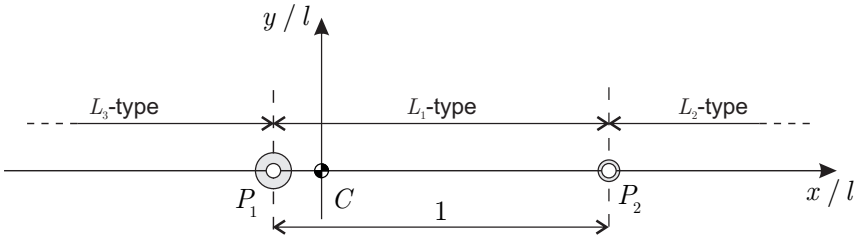

Figure 3.5: Nomenclature of the collinear equilibrium points.

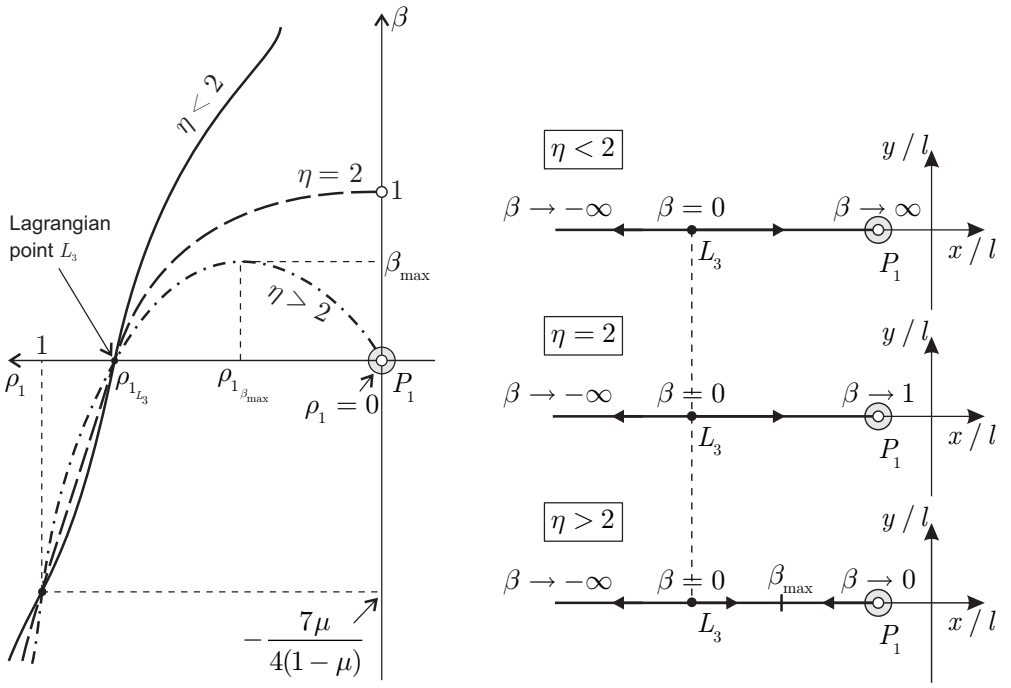

(a) Lightness number β.

(b) Variation of β on the locus (arrows indicate a $|\beta|$ increase).

Figure 3.6: Lightness number as a function of ρ_1 and η for L_3-type equilibrium points locus.

Lagrange point L_3. As the thrust tends to zero ($\beta = 0$), one AEP tends to coincide with L_3 and the other approaches P_1. Moreover, if β is negative, that is, the propulsive acceleration is in the direction of the attractor P_1, there exists a single AEP on the left of L_3. Such a point can be theoretically placed at any distance from P_1 provided that a sufficient value of β is available.

Similar conclusions can be drawn for L_1-type points, that is, points in which $\hat{\boldsymbol{\rho}}_1 \cdot \hat{\boldsymbol{\imath}} = +1$ and $\rho_1 < 1$, see Figs. 3.7(a) and 3.7(b). In this case, η being the same, a negative value of β corresponds to an AEP between the Lagrangian point

L_1 and the attractor P_2, while the condition $\beta > 0$ allows the AEP to be moved toward the massive attractor P_1. In this case, differently from the triangular and L_3-type points, an increase of η always corresponds to a decrease of $|\beta|$.

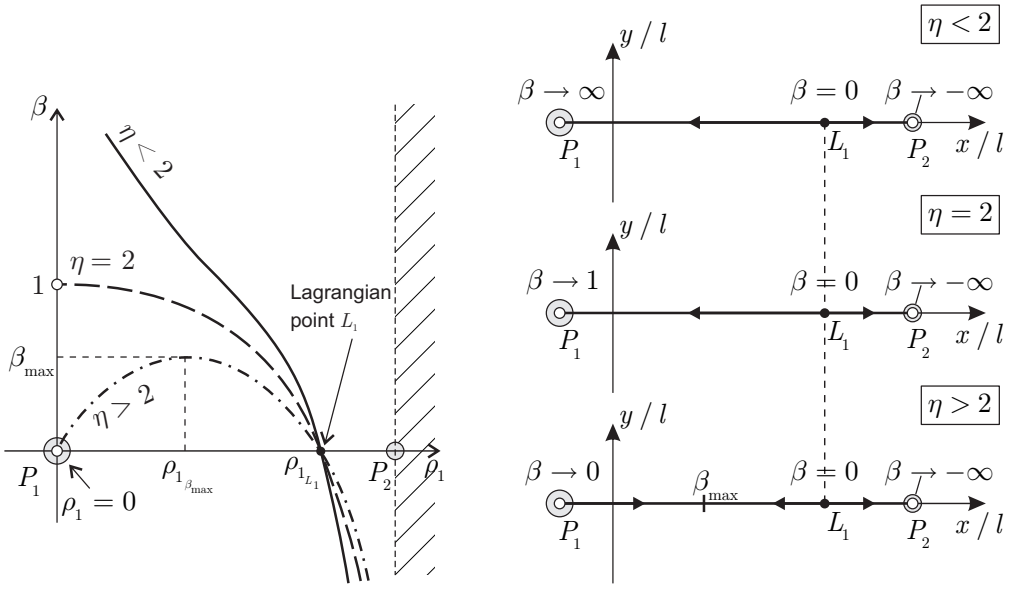

(a) Lightness number β.

(b) Variation of β on the locus (arrows indicate a $|\beta|$ increase).

Figure 3.7: Lightness number as a function of ρ_1 and η for L_1-type equilibrium points locus.

Finally, the contour curves corresponding to the L_2-type points (when $\hat{\boldsymbol{\rho}}_1 \cdot \hat{\boldsymbol{\imath}} = +1$ and $\rho_1 > 1$) are illustrated in Fig. 3.8(a). Figure 3.8(a) shows that there exists a suitable value of η, referred to as $\widetilde{\eta}$, beyond which the contour curves of β display both a local minimum ($\beta_{\min}$) and a maximum ($\beta_{\max}$) at a distance $\rho_{1_{\beta_{\min}}}$ and $\rho_{1_{\beta_{\max}}}$ from the body P_1, respectively. For $\eta > \widetilde{\eta}$ and $\beta \in (\beta_{\min}, \beta_{\max})$, three AEPs are obtained, whose position is between $\rho_{1_{\beta_{\min}}}$ and $\rho_{1_{\beta_{\max}}}$. Note that the value of $\widetilde{\eta}$ is a function of the dimensionless mass of P_2 only and decreases with μ, as is shown in Fig. 3.9. The presence of the above points of maximum and minimum is therefore confined to high value of η, that is, $\widetilde{\eta} > 9.5$, see Fig. 3.9.

3.3.3 Displaced Points

If d_k, d_i, and d_ρ are all different from zero, Eq. (3.8) can be satisfied only provided that $\boldsymbol{\rho}_1 \cdot \hat{\boldsymbol{\jmath}} = 0$, that is, if AEPs belong to the (x, z) plane. Such points will be referred to as displaced points, in analogy to the usual nomenclature for non-Keplerian orbits [8], which are obtained by using low-thrust propulsion systems.

Taking the dot product of both sides of Eq. (3.8) by $\hat{\boldsymbol{k}}$, by $\hat{\boldsymbol{\imath}}$ and by $\hat{\boldsymbol{\jmath}}$ the

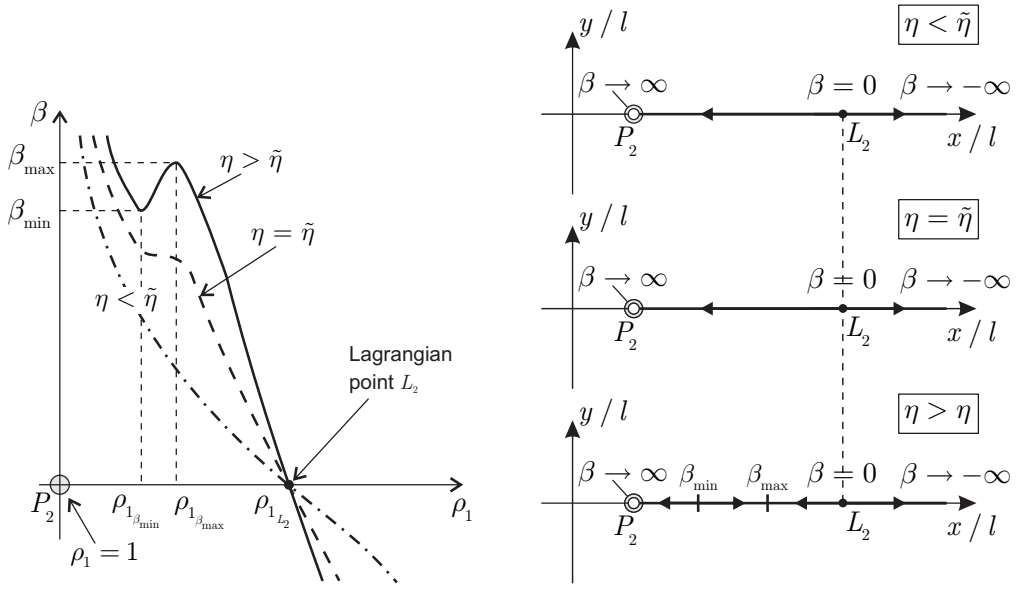

(a) Lightness number β.

(b) Variation of β on the locus (arrows indicate a $|\beta|$ increase).

Figure 3.8: Lightness number as a function of ρ_1 and η for L_2-type equilibrium points locus.

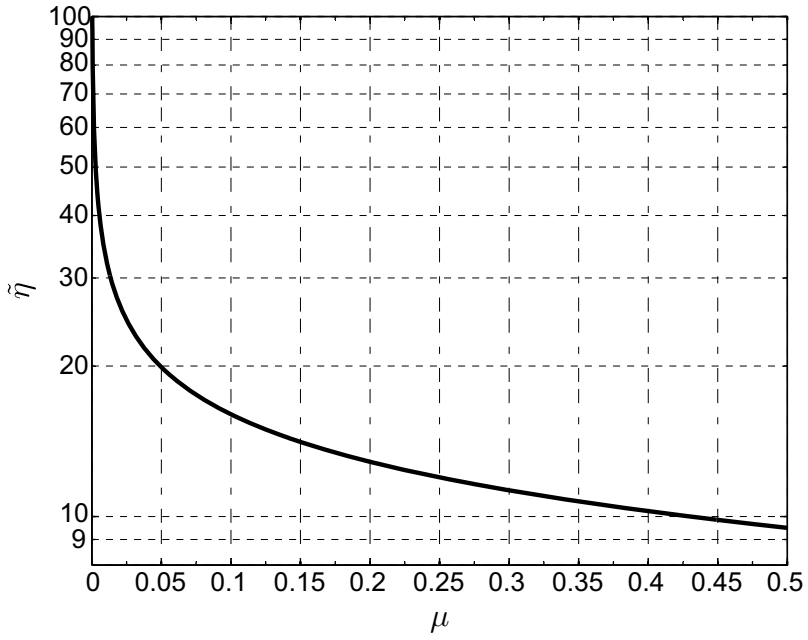

Figure 3.9: Parameter $\widetilde{\eta}$ as a function of μ for L_2-type points.

position of displaced points is defined by

$$d_k = d_\rho \hat{\boldsymbol{\rho}}_1 \cdot \hat{\boldsymbol{k}} \quad , \quad d_i = d_k \frac{\hat{\boldsymbol{\rho}}_1 \cdot \hat{\boldsymbol{\imath}}}{\hat{\boldsymbol{\rho}}_1 \cdot \hat{\boldsymbol{k}}} \quad , \quad \hat{\boldsymbol{\rho}}_1 \cdot \hat{\boldsymbol{\jmath}} = 0 \tag{3.14}$$

Recalling Eqs. (3.9), Eq. (3.14) is written as

$$\boldsymbol{\rho}_1 \cdot \hat{\boldsymbol{\jmath}} = 0 \quad , \quad \frac{\mu}{\rho_2^3} = \mu - \boldsymbol{\rho}_1 \cdot \hat{\boldsymbol{\imath}} \quad , \quad \beta = \rho_1^{\eta-2} \left(1 + \frac{\mu}{1-\mu} \frac{\rho_1^3}{\rho_2^3} \right) \tag{3.15}$$

The first two relations of Eq. (3.15) define the locus of the displaced points. In fact, by using the condition $\boldsymbol{\rho}_1 \cdot \hat{\boldsymbol{\jmath}} = 0$, is

$$\boldsymbol{\rho}_1 = (x/l + \mu)\hat{\boldsymbol{\imath}} + (z/l)\hat{\boldsymbol{k}} \tag{3.16a}$$

$$\boldsymbol{\rho}_2 = (x/l + \mu - 1)\hat{\boldsymbol{\imath}} + (z/l)\hat{\boldsymbol{k}} \tag{3.16b}$$

Therefore, the second relation of Eq. (3.15) gives

$$z/l = \pm\sqrt{(-l\,\mu/x)^{2/3} - (x/l + \mu - 1)^2} \tag{3.17}$$

which defines the locus of the displaced points. Note that the locus is symmetrical with respect to the x-axis and the points are such that $x \in (-\mu, 0)$ or, equivalently, $\rho_2 > 1$.

The third condition of Eq. (3.15), provides the value of β for each point of the locus. As expected, displaced points cannot be obtained if $\beta = 0$. Indeed, the right hand side of the third condition of Eq. (3.15) is the sum of two strictly positive terms and, therefore, it cannot vanish. Moreover, with $\eta = 2$, the expression for β is in agreement with Kunitsyn and Perezhogin [31] and Simmons et al. [33], who consider the acceleration caused by the solar radiation pressure.

Using Eq. (3.16) to calculate ρ_1 and ρ_2, and substituting Eq. (3.17) for z/l, the third relation of Eq. (3.15) for β can be written as a function of the dimensionless coordinate x/l only. The function $\beta = \beta(x/l)$ is drawn in Fig. 3.10.

As for the L_2-type points, it can be shown that a suitable value $\widetilde{\eta} < 2$ exists, such that the function $\beta = \beta(x/l)$ presents two stationary points when $\eta \in (\widetilde{\eta},\, 2)$. Figure 3.11 shows how $\widetilde{\eta}$ varies with μ. When $\eta \leq \widetilde{\eta}$ or $\eta > 2$, only two equilibrium points exist for a given value of β. On the other hand, when $\eta \in (\widetilde{\eta}, 2)$, there is a range of $\beta \in [\beta_{\min}, \beta_{\max}]$, such that four or six equilibrium points are possible. The different kinds of AEP locus are illustrated in Fig. 3.12, where the point A corresponds to the condition $\rho_1 = 1$. Note that for a given $\rho_1 < 1$ (> 1) it is necessary to increase (decrease) η to decrease the lightness number β. In particular, according to Kunitsyn and Perezhogin [31] and Simmons et al. [33], if $\eta = 2$ two (symmetrical) equilibrium points exist only for β ranging in the interval $(1, 1/(1-\mu))$.

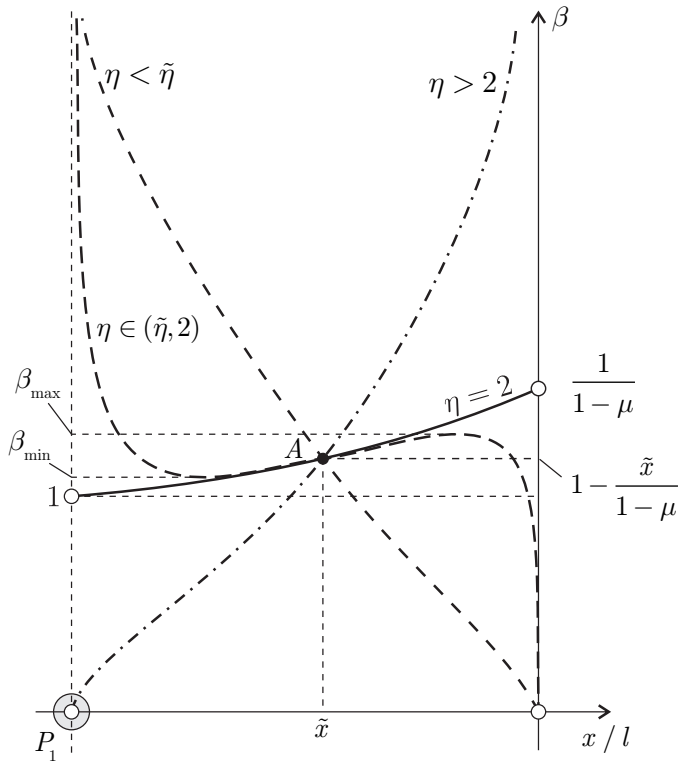

Figure 3.10: Lightness number β as a function of x/l and η for displaced points.

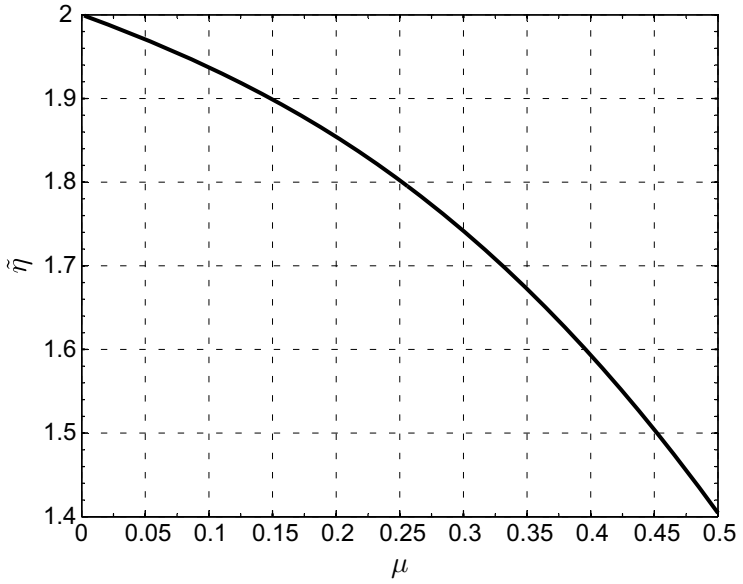

Figure 3.11: Parameter $\widetilde{\eta}$ as a function of μ for displaced points.

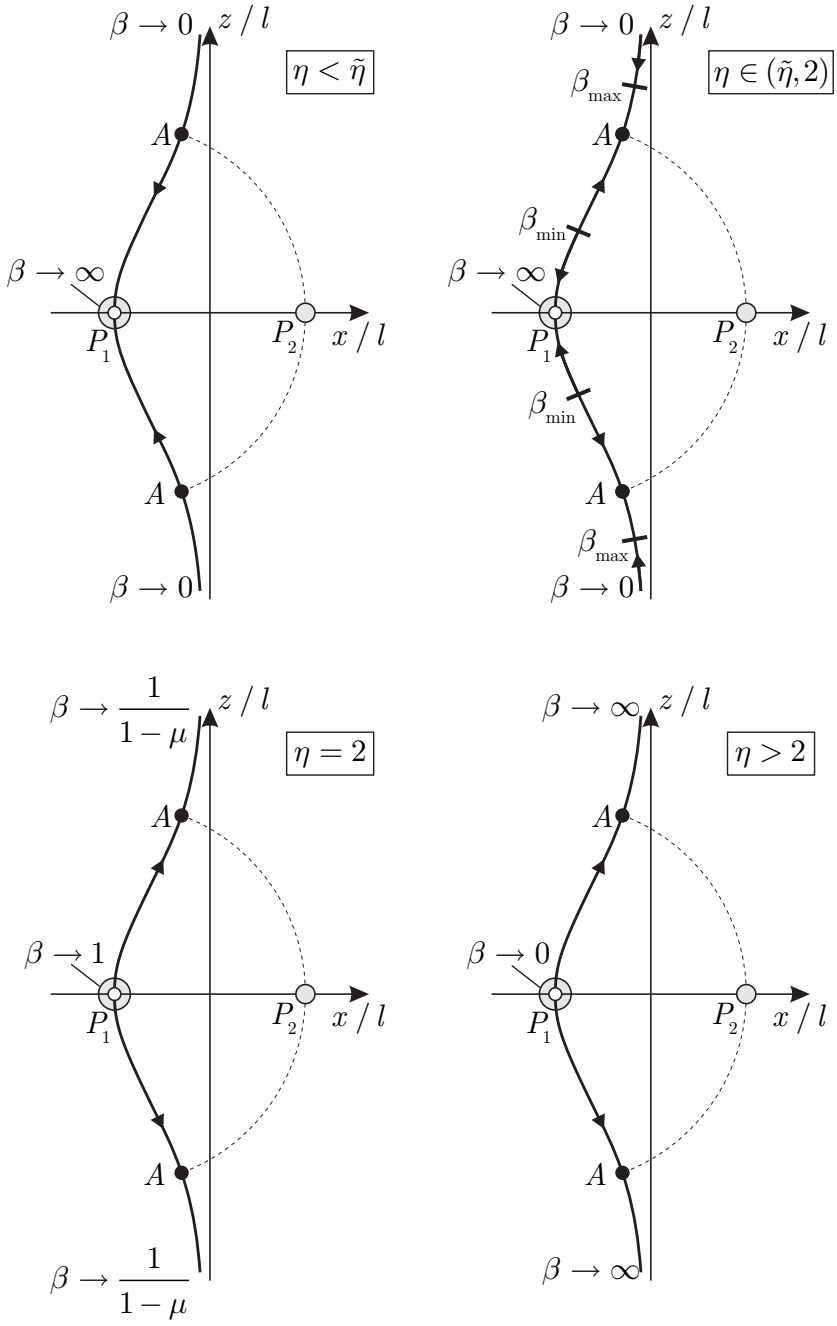

Figure 3.12: Variation of β on the displaced points locus (arrows indicate a $|\beta|$ increase).

3.4 Linear Stability Analysis

In this section, the dynamical behavior of the spacecraft is better characterized by investigating its linear stability around an AEP. To this end, define the generic equilibrium position $\boldsymbol{r}_0$ and introduce the transformation $\boldsymbol{r} = \boldsymbol{r}_0 + \delta\boldsymbol{r}$.

The variational equation of motion is obtained by linearizing Eq. (3.2) around $\boldsymbol{r}_0$. According to Refs. [11, 14], the result is

$$\delta\boldsymbol{r}'' = \boldsymbol{K}^{\mathrm{T}} \cdot \delta\boldsymbol{r} - 2\boldsymbol{E} \cdot \delta\boldsymbol{r}' \tag{3.18}$$

where the second order tensors $\boldsymbol{K}$ and $\boldsymbol{E}$ are defined by

$$\boldsymbol{K} \triangleq \nabla \left[-\frac{1-\mu}{\rho_1^3}\boldsymbol{\rho}_1 - \frac{\mu}{\rho_2^3}\boldsymbol{\rho}_2 + \beta\frac{1-\mu}{\rho_1^{\eta+1}}\boldsymbol{\rho}_1 - \hat{\boldsymbol{k}} \times \left(\hat{\boldsymbol{k}} \times \boldsymbol{r}\right) \right] \Bigg|_{\boldsymbol{r}_0} \tag{3.19}$$

$$\boldsymbol{E} \cdot \boldsymbol{r} \triangleq \hat{\boldsymbol{k}} \times \boldsymbol{r} \tag{3.20}$$

Introducing the state vector

$$[\boldsymbol{\xi}]_{\mathcal{T}} = \left[\delta\boldsymbol{r} \cdot \hat{\boldsymbol{\imath}},\ \delta\boldsymbol{r} \cdot \hat{\boldsymbol{\jmath}},\ \delta\boldsymbol{r} \cdot \hat{\boldsymbol{k}},\ \delta\boldsymbol{r}' \cdot \hat{\boldsymbol{\imath}},\ \delta\boldsymbol{r}' \cdot \hat{\boldsymbol{\jmath}},\ \delta\boldsymbol{r}' \cdot \hat{\boldsymbol{k}} \right]^{\mathrm{T}} \tag{3.21}$$

the linearized equation of motion takes the form

$$\left[\boldsymbol{\xi}'\right]_{\mathcal{T}} = \mathbb{A}\,[\boldsymbol{\xi}]_{\mathcal{T}} \tag{3.22}$$

with

$$\mathbb{A} = \begin{bmatrix} \mathbb{O} & \mathbb{I} \\ \mathbb{K}^{\mathrm{T}} & -2\,\mathbb{E} \end{bmatrix} \tag{3.23}$$

where $\mathbb{O}$ is a 3×3 zero matrix, $\mathbb{I}$ is a 3×3 identity matrix, while matrices $\mathbb{K}$ and $\mathbb{E}$ contain the components of the second order tensors $\boldsymbol{K}$ and $\boldsymbol{E}$ in the rotating frame $\mathcal{T}$, that is

$$\mathbb{K} \triangleq [\boldsymbol{K}]_{\mathcal{T}} = \begin{bmatrix} k_{11} & k_{12} & k_{13} \\ k_{21} & k_{22} & k_{23} \\ k_{31} & k_{32} & k_{33} \end{bmatrix} \quad , \quad \mathbb{E} \triangleq [\boldsymbol{E}]_{\mathcal{T}} = \begin{bmatrix} 0 & -1 & 0 \\ 1 & 0 & 0 \\ 0 & 0 & 0 \end{bmatrix} \tag{3.24}$$

The value of all of matrix entries k_{ij} (with $(i,j) = 1,2,3$) is detailed in the Appendix B, as a function of ρ_1 (or ρ_2), η, and μ, for the three different families of AEPs.

Equation (3.22) represents a system of autonomous, linear differential equations. Consequently, the study of the linear stability of such a system is based on the calculation of the eigenvalues of the matrix $\mathbb{A}$. If λ is the generic eigenvalue of $\mathbb{A}$, the characteristic equation of $\mathbb{A}$ can be shown to be in the form

$$\lambda^6 + a\,\lambda^4 + b\,\lambda^2 + c = 0 \tag{3.25}$$

or

$$s^3 + a\,s^2 + b\,s + c = 0 \tag{3.26}$$

where $s \triangleq \lambda^2$ and a, b, and c are real coefficients that depend on the entries k_{ij}. Note that if $\bar{\lambda}$ is a root of Eq. (3.25), then so is $-\bar{\lambda}$. Therefore, for $\bar{\lambda}$ to be a stable eigenvalue (that is, a root with no positive real part) it is necessary that $\bar{\lambda}$ is both imaginary and a simple root[2] of Eq. (3.25). In such a case the system is *marginally*[3] stable.

According to Abramowitz and Stegun [38] and by using the Descartes sign rule [39], the system is marginally stable if and only if

$$\Delta_3 < 0 \;\cap\; a \geq 0 \;\cap\; b \geq 0 \;\cap\; c > 0 \tag{3.27}$$

where Δ_3 is the discriminant of the cubic equation (3.26), that is:

$$\Delta_3 \triangleq \frac{1}{4}\left(c + \frac{2\,a^3 - 9\,a\,b}{27}\right)^2 + \frac{1}{27}\left(b - \frac{a^2}{3}\right)^3 \tag{3.28}$$

As will be shown later, in some cases the characteristic equation (3.26) can be factorized as

$$(s - \widetilde{c})\,\left(s^2 + \widetilde{a}\,s + \widetilde{b}\right) = 0 \tag{3.29}$$

with suitable values of $\widetilde{a}, \widetilde{b}$, and $\widetilde{c}$, still depending on the entries k_{ij}. In such circumstances the necessary and sufficient conditions for the marginal stability become

$$\left(\widetilde{a}^2 - 4\,\widetilde{b}\right) > 0 \;\cap\; \widetilde{a} \geq 0 \;\cap\; \widetilde{b} > 0 \;\cap\; \widetilde{c} < 0 \;\cap\; \left(\widetilde{c}^2 + \widetilde{a}\,\widetilde{c} + \widetilde{b}\right) \neq 0 \tag{3.30}$$

Because both the conditions (3.27) and (3.30) affect only the coefficients of the characteristic equation, the stability of the linearized system can be investigated without the need of calculating the roots of Eq. (3.25). Moreover, with the aid of the results in Appendix B, it can be verified that for a given system of attractors the coefficients of the characteristic equation are a function only of η and ρ_1 (or ρ_2). Therefore, it is possible to draw the regions of stable AEPs for the different families of points, as is now discussed in detail.

3.4.1 Stability of Triangular Points

The characteristic equation for triangular type points is in the form of Eq. (3.29) with

$$\widetilde{a} = 4 - k_{11} - k_{22} \quad , \quad \widetilde{b} = k_{11}\,k_{22} - k_{12}^2 \quad , \quad \widetilde{c} = k_{33} \tag{3.31}$$

[2] An eigenvalue of $\mathbb{A}$ is $\lambda = \pm\sqrt{s}$, therefore the system is stable if s is a negative, real and simple root of Eq. (3.26). As a consequence, the system is stable if λ is both imaginary and a simple root of Eq. (3.25).

[3] *Marginally* stable is a system where bounded oscillations around the equilibrium point are maintained indefinitely.

where k_{11}, k_{22}, k_{33} and k_{12} are given in Appendix B by Eqs. (B.5)–(B.8).

The conditions (3.29) (with the exception of $\tilde{c} < 0$, which is always satisfied) must be studied numerically to find the stability region in the plane (ρ_1, η). An example is shown in Fig. 3.13 for some values of μ, including the critical value $\mu^\star$, which defines the stability of the classic solution with $\rho_1 = 1$, see Sec. 2.1.2.

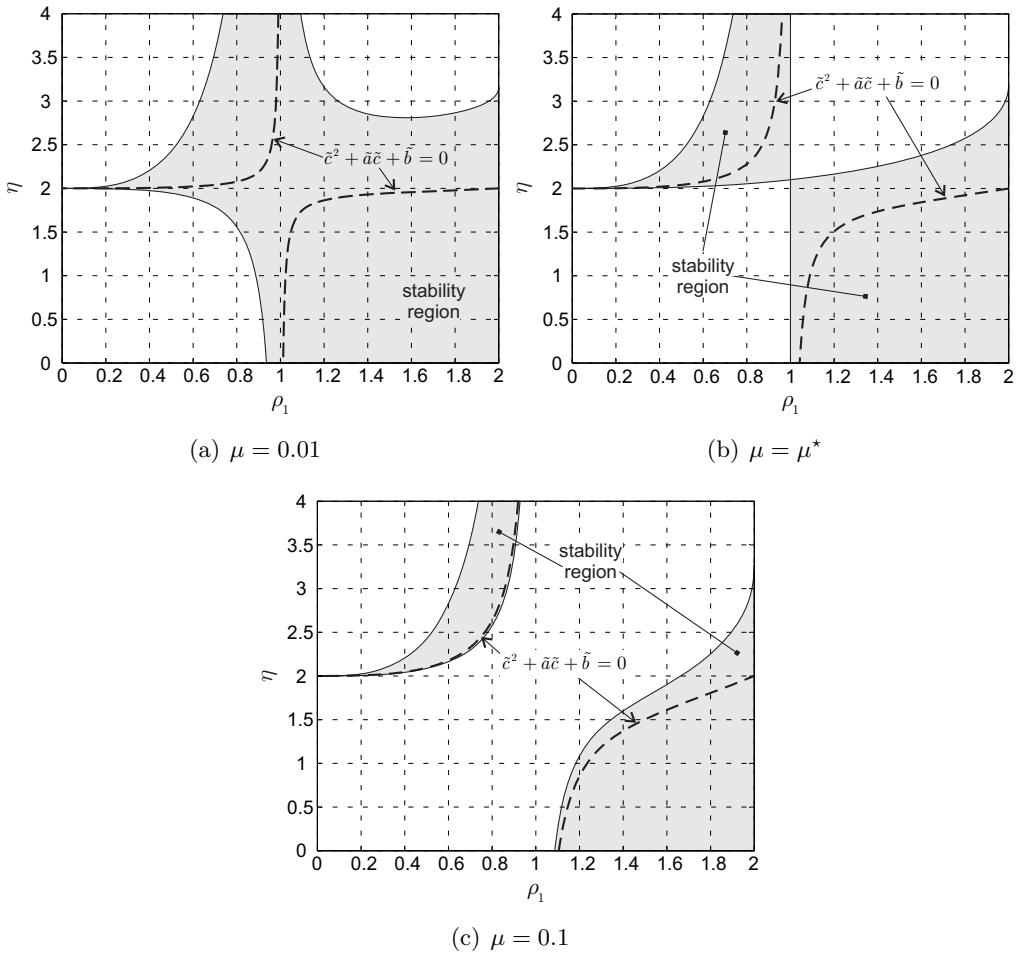

(a) $\mu = 0.01$

(b) $\mu = \mu^\star$

(c) $\mu = 0.1$

Figure 3.13: Stability region for triangular points for different values of μ (the dashed lines are excluded).

As long as $\mu \geq \mu^\star$, the plane (ρ_1, η) contains two distinct stability regions, see Fig. 3.13(c), which exclude the case $\rho_1 = 1$. As μ is decreased, the two regions get closer and eventually they touch when $\mu = \mu^\star$, see Fig. 3.13(b). Finally, if $\mu < \mu^\star$ there exists a single stability region in the plane (ρ_1, η), as shown in Fig. 3.13(a). Note that, in the various cases, the boundary line does not belong to the stability region.

3.4.2 Stability of Collinear Points

The characteristic equation for collinear points is in the form of Eq. (3.29) with

$$\widetilde{a} = 4 - k_{11} - k_{22} \quad , \quad \widetilde{b} = k_{11}\, k_{22} \quad , \quad \widetilde{c} = k_{33} \tag{3.32}$$

where k_{11}, k_{22}, and k_{33} are given in Eqs. (B.11)–(B.12) or (B.17)–(B.18). The stability conditions, provided by Eq. (3.30), must be specialized to the different families of AEPs.

For L_3-type points, taking into account that $k_{33} < 0$ and $k_{22} < 0$, the stability conditions (3.30) reduce to

$$(4 - k_{11} - k_{22})^2 - 4\, k_{11}\, k_{22} > 0 \ \cap \ k_{11} < 0 \tag{3.33}$$

where k_{11} and k_{22} are given by Eqs. (B.11) and (B.12), respectively. Firstly assume that $k_{11} < 0$. The left inequality (3.33) can be written as

$$(k_{11} - k_{22})^2 - 8\ (k_{11} + k_{22}) + 16 > 0 \tag{3.34}$$

which is always fulfilled because $k_{22} < 0$. That means that L_3-type points are stable provided that $k_{11} < 0$. From Eq. (B.11) the sign of k_{11} is a function of $\partial\beta/\partial\rho_1$. According to Fig. 3.6(a), it is $k_{11} < 0$ if $\eta > 2 \cap \rho_1 < \rho_{1_{\beta_{\max}}}$, where $\rho_{1_{\beta_{\max}}}$ corresponds to the distance ρ_1 at which the function $\beta = \beta(\rho_1, \eta > 2)$ attains its maximum value. The variation of $\rho_{1_{\beta_{\max}}}$ with η, for a given value of μ, is qualitatively drawn in Fig. 3.14(a) along with the stability region of L_3-type points.

Similar considerations apply to L_1-type points, when k_{11}, k_{22}, and k_{33} are taken from (B.17)–(B.18). The corresponding stability region is shown in grey in Fig. 3.14(b). Note that for both Figs. 3.14(a) and 3.14(b), the boundary of the stability region is to be excluded as it corresponds to the condition $k_{11} = 0$.

Finally, the stability conditions (3.30) for L_2-type points can be simplified by separating the analysis for $\rho_1 < 2$ and $\rho_1 > 2$. In fact, when $\rho_1 < 2$ the stability conditions coincide with those shown in Eq. (3.33) in which k_{11} and k_{22} are now given by Eqs. (B.17) and (B.18). The study of the stability region proceeds as in case of L_3-type points, and the corresponding graphical results are summarized in Fig. 3.14(c). Note that the value $\widetilde{\eta}$ shown in Fig. 3.14(c) depends on μ and can be taken from Fig. 3.9. On the contrary, when $\rho_1 > 2$ the conditions (3.30) must be studied with a numerical approach. For a given value of μ the stability region (with the exclusion of the boundary line) can be drawn in the plane (ρ_1, η). An example of this kind of study is shown in Fig. 3.15 where the region corresponding to $\rho_1 < 2$ is also displayed for the sake of completeness. Note that the equilibrium point corresponding to $\rho_1 = 2$ is unstable. In fact in such a case $\widetilde{b} = 0$, see Eqs. (3.30).

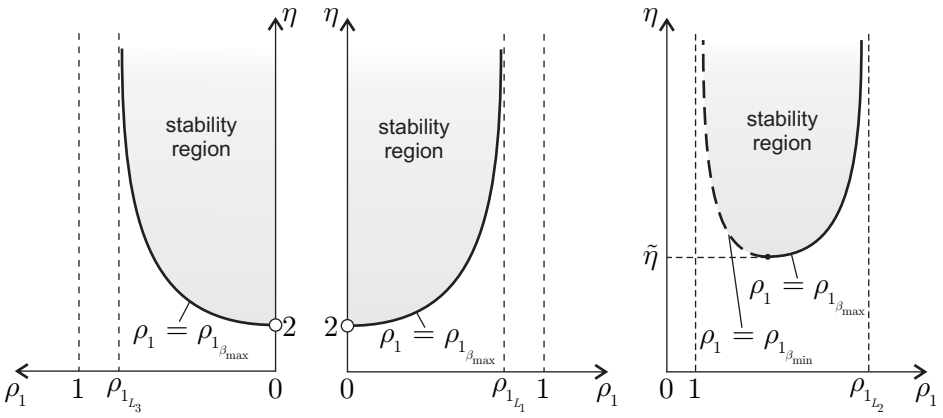

(a) L_3-type points. (b) L_1-type points. (c) L_2-type points.

Figure 3.14: Position of stationary values of β as a function of η for collinear points.

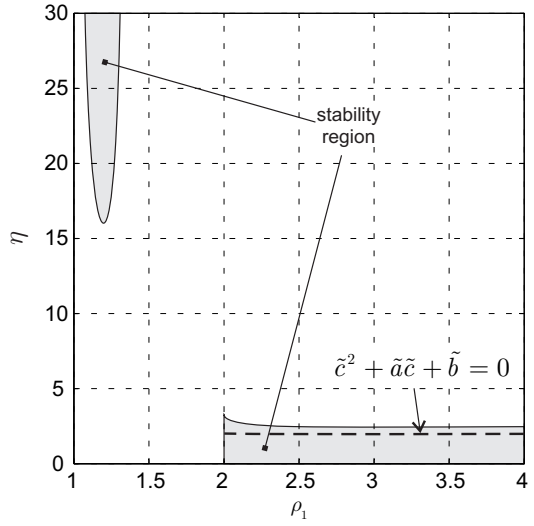

Figure 3.15: Stability region for L_2–type collinear points with $\mu = 0.1$ (the dashed line is excluded).

It is interesting to note that Fig. 3.15 shows that for $\eta = 0$ there exist stable points only provided that $\rho_1 > 2$. Such a result of Fig. 3.15 do not match that of Morimoto et al. [16] because of the different assumptions made on the thrust direction. In fact Morimoto et al.. [16] use a constant thrust vector, that is, a vector with a constant modulus and a fixed direction in the synodic reference frame. Accordingly, in Ref. [16] the gradient of the propulsive acceleration is equal to zero. On the contrary, in the case of a generalized sail, when $\eta = 0$ the thrust

modulus is constant, but its orientation is always radial, see Eq. (2.15). Therefore, when the system is perturbed, the gradient of the propulsive acceleration is different from zero, see Eq. (3.19).

3.4.3 Stability of Displaced Points

The characteristic equation for displaced points is in the form of Eq. (3.26) in which, bearing in mind Eq. (B.25), the coefficients a, b, and c can be written as

$$a = 3 - k_{11} - k_{33} \quad , \quad c = k_{13}^2 - k_{11}\, k_{33} \quad , \quad b = k_{11} - 3\, k_{33} - c \tag{3.35}$$

where k_{11}, k_{33}, and k_{13} are obtained from Eqs. (B.24), (B.26), and (B.27).

The stability region must be investigated with a numerical approach by looking for the pairs ρ_2 and η that, for a given value of μ, satisfy the conditions in Eq. (3.27). The results for some value of μ are summarized in Fig. 3.16, in which the stability region does not include the boundary line.

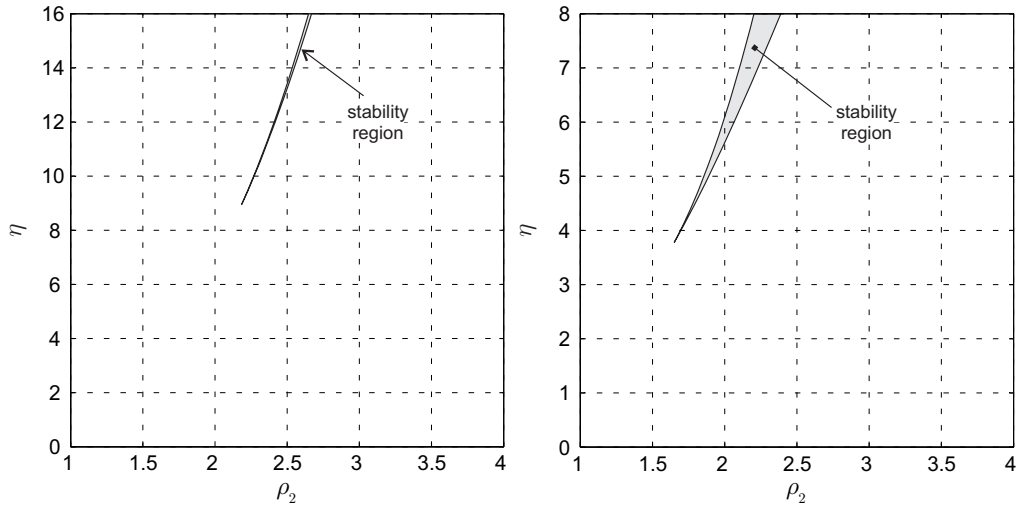

(a) $\mu = 0.01$ (b) $\mu = 0.1$

Figure 3.16: Stability region for displaced points for different values of μ.

Chapter 4

Artificial Equilibrium Points for a Generalized Sail in the Elliptic Restricted Three-Body Problem

To obtain a more realistic model than the circular case, this chapter discusses the existence of *Artificial Equilibrium Point*s maintained by a *Generalized Sail* based spacecraft in an *Elliptic Restricted Three-Body Problem*. The position of the Artificial Equilibrium Points is conveniently located using a rotating and pulsating coordinate frame, where the loci of the equilibrium points coincide with those obtained for the circular case. Moreover, as expected in the classical case of absence of thrust, all the equilibrium points belong to the orbital plane of the two celestial bodies. The stability of Artificial Equilibrium Points is also discussed by means of the Floquet theory, and a comparison with the results of the circular case is provided.

4.1 Introduction

In the past, several authors studied the equilibrium points of the classical ER3BP, concentrating most efforts on the study of their linear stability and on the evaluation of the monodromy matrix associated to the periodic linear system, arising from the linearization of the equation of motion [40–49]. Subsequently, the possibility of generating equilibrium points different from the classical ones has been revealed, when the photogravitational problem has been studied [50–53]. Recently, as a natural extension of the photogravitational problem, Baoyin and McInnes [54] have discussed the creation of AEPs maintained by Solar Sail based spacecraft in the ER3BP. In this mission scenario, it has been shown that Solar Sails are also able to maintain equilibrium points out of the orbital plane of the two attractors, by means of a control logic exploiting their thrust vectoring capability.

4.2 Mathematical Model

Consider the motion of a Generalized Sail based spacecraft (S in Fig. 4.1) under the gravitational effect of two celestial bodies P_1 and P_2, with masses m_1 and $m_2 \leq m_1$, respectively (see Fig. 4.1). Assume the two celestial bodies cover elliptic orbits, of eccentricity e, around their centre-of-mass C, and that their variable reciprocal distance is $\ell = a(1-e^2)g$, where g is defined in Eq. (2.2).

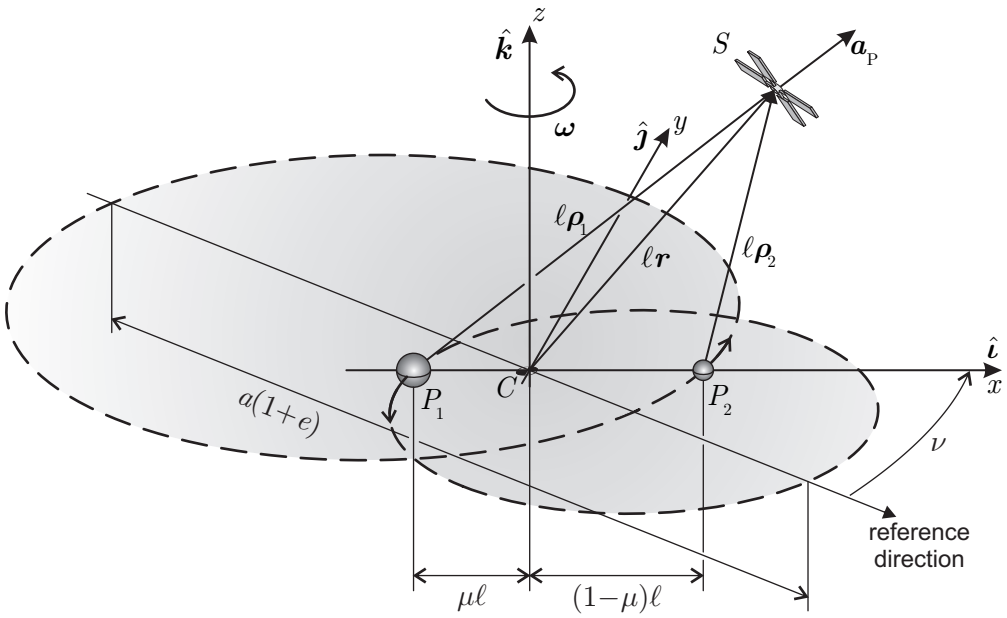

Figure 4.1: Generalized Sail based spacecraft in the Elliptic Restricted Three-Body Problem.

If P_1 is used as reference celestial body and a as reference distance, then the propulsive acceleration $\boldsymbol{a}_{\mathrm{P}}$ provided by the Generalized Sail is parallel to $\hat{\boldsymbol{\rho}}_1 = \boldsymbol{\rho}_1/\|\boldsymbol{\rho}_1\|$, and, from Eq. (2.18)

$$\boldsymbol{a}_{\mathrm{P}} = \beta \frac{Gm_1}{a^2}\left(\frac{a}{\ell\rho_1}\right)^{\eta}\hat{\boldsymbol{\rho}}_1 \tag{4.1}$$

According to Appendix A, the dimensionless equation of motion of the spacecraft is

$$\begin{aligned}&\boldsymbol{r}'' + 2\hat{\boldsymbol{k}}\times\boldsymbol{r}' = \\ &\quad g\left[-\frac{1-\mu}{\rho_1^3}\boldsymbol{\rho}_1 - \frac{\mu}{\rho_2^3}\boldsymbol{\rho}_2 + B\frac{1-\mu}{\rho_1^{\eta}}\hat{\boldsymbol{\rho}}_1 - \hat{\boldsymbol{k}}\times\left(\hat{\boldsymbol{k}}\times\boldsymbol{r}\right) - e\cos\nu\left(\boldsymbol{r}\cdot\hat{\boldsymbol{k}}\right)\hat{\boldsymbol{k}}\right]\end{aligned} \tag{4.2}$$

where

$$B \triangleq \frac{\beta}{\left[(1-e^2)\,g\right]^{\eta-2}} \tag{4.3}$$

will be referred to as *modified sail lightness number*.

Note that in the limiting case of $e = 0$, which corresponds to the CR3BP, Eqs. (2.2) and (4.3) state that B coincides with β, irrespective of the value of η. The same conclusion holds for any eccentricity provided that $\eta = 2$ (this is the case when the propulsion system corresponds to a Solar Sail, for example). However, in a generic case in which $e > 0$ and $\eta \neq 2$, the value of B depends on the angular coordinate ν by means of g, see Eq. (2.2). In particular, for a fixed value of β, B varies with time, between a minimum and a maximum value, depending[1] on the angular coordinate ν.

4.3 Artificial Equilibrium Points

As for the classical case in absence of thrust, the AEPs are obtained by enforcing the stationary condition $\boldsymbol{r}'' = 0$ and $\boldsymbol{r}' = 0$ in Eq. (4.2).

Recalling that (see Fig. 4.1)

$$\boldsymbol{r} = \boldsymbol{\rho}_1 - \mu\,\hat{\boldsymbol{\imath}} \qquad , \qquad \boldsymbol{\rho}_2 = \boldsymbol{\rho}_1 - \hat{\boldsymbol{\imath}} \tag{4.4}$$

the position of AEPs can be found as solution of

$$d_k\,\hat{\boldsymbol{k}} + d_i\,\hat{\boldsymbol{\imath}} = d_\rho\,\hat{\boldsymbol{\rho}}_1 \tag{4.5}$$

where the dimensionless parameters d_k, d_i, and d_ρ are given by

$$\begin{aligned} d_k &\triangleq (1 + e\,\cos\nu)\left(\boldsymbol{\rho}_1 \cdot \hat{\boldsymbol{k}}\right) \quad , \quad d_i \triangleq \mu\left(1 - \frac{1}{\rho_2^3}\right) \quad , \\ d_\rho &\triangleq \rho_1 - \frac{1-\mu}{\rho_1^2} - \frac{\mu\rho_1}{\rho_2^3} + \frac{B}{\rho_1^\eta}(1-\mu) \end{aligned} \tag{4.6}$$

The constraint in Eq. (4.5) can be thought of as the extension to the elliptic case of the similar result found for the circular problem, see Eq. (3.8). In particular, an analysis of Eq. (4.5) provides the loci of the AEPs in the pulsating rotating reference frame $\mathcal{T}_P(C;\, x/\ell,\, y/\ell,\, z/\ell)$ and the value of the *constant* modified sail lightness number B necessary to maintain the equilibrium points. Table 4.1 and Fig. 4.2 provide the equations for the loci and the corresponding nomenclature, derived from the circular problem.

Before going into a detailed description of the loci, note that, similar to the classical case in absence of thrust (see Fig. 2.2(b)), an AEP corresponds to a spacecraft position $\boldsymbol{r}_0$ that is fixed with respect to the pulsating rotating reference frame $\mathcal{T}_P$. However such a position, when seen by an observer in the rotating frame $\mathcal{T}\,(C;\; x,\; y,\; z)$, oscillates pulsating back and forth along a segment of length $d = 2ae\|\boldsymbol{r}_0\|$, see Fig. 4.3.

[1] The presence of ν in Eq. (4.2) implies an increase in complexity of the ER3BP with respect to the CR3BP. Note, in fact, that the system dynamics is now described in terms of non-autonomous ordinary differential equations.

Conditions for Eq. (3.8)			Locus equations	Locus name
$d_k = 0$	$d_i = 0$	$d_\rho = 0$	$\boldsymbol{\rho}_1 \cdot \hat{\boldsymbol{k}} = 0,\ \rho_2 = 1$	triangular points
		$d_\rho \neq 0$	not possible	
	$d_i \neq 0$	$d_\rho = 0$	not possible	
		$d_\rho \neq 0$	$\boldsymbol{\rho}_1 \parallel \hat{\boldsymbol{\imath}}$	collinear points
$d_k \neq 0$	$d_i = 0$	$d_\rho = 0$	not possible	
		$d_\rho \neq 0$	not possible	
	$d_i \neq 0$	$d_\rho = 0$	not possible	
		$d_\rho \neq 0$	not possible	

Table 4.1: Summary of AEPs loci in the ER3BP.

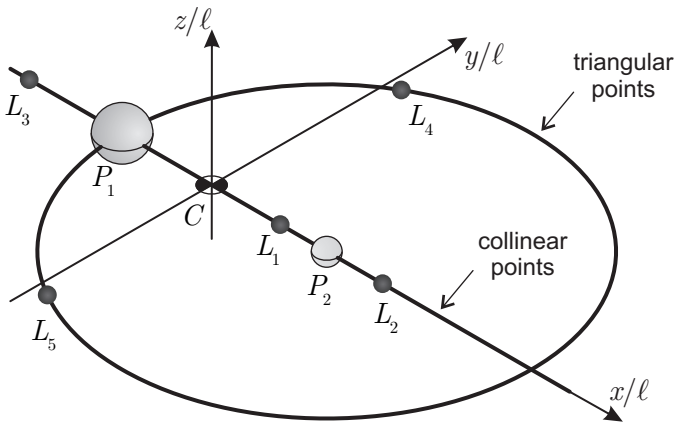

Figure 4.2: Nomenclature for AEPs loci in the ER3BP.

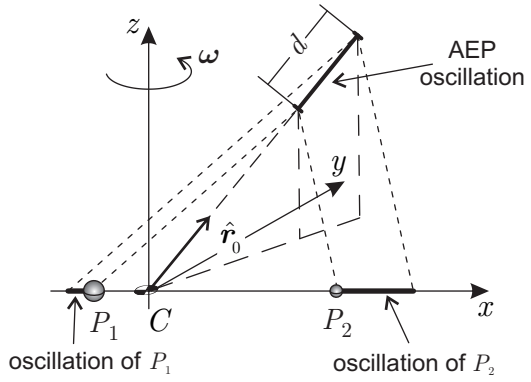

Figure 4.3: Oscillation of an AEP in the rotating frame.

4.3.1 Triangular Points

The triangular points are obtained when the coefficients d_k, d_i and d_ρ are all equal to zero, that is, from Eq. (4.6), when

$$\boldsymbol{\rho}_1 \cdot \hat{\boldsymbol{k}} = 0 \quad , \quad \rho_2 = 1 \quad , \quad B = \rho_1^{\eta+1} \left(\frac{1}{\rho_1^3} - 1 \right) \tag{4.7}$$

Equation (4.7) formally coincides with the corresponding Eq. (3.10) for the circular case, therefore similar conclusions regarding the triangular points are obtained.

In particular, triangular AEPs are located on a circle of unit radius and center P_2 in the pulsating reference frame, and they coincide with the classical equilibrium points L_4 and L_5 in absence of thrust (namely, $B = 0$). In addition, for a given value of ρ_1, the third relation of Eq. (4.7) gives the constant value of B required to satisfy the equilibrium conditions. Such a value of B coincides with the lightness number that would be required to generate a triangular equilibrium point in a CR3BP at a distance ρ_1 from the massive body P_1.

Therefore, the results in Figs. 3.3 and 3.4 for the circular problem are immediately extended to the elliptic case by formally substituting the classic sail lightness number β with the modified sail lightness number B.

4.3.2 Collinear Points

The collinear points are identified by the conditions $d_k = 0$, $d_i \neq 0$ and $d_\rho \neq 0$. In this case Eqs. (4.5) and (4.6) may be combined to get

$$\begin{aligned} &\boldsymbol{\rho}_1 \cdot \hat{\boldsymbol{k}} = 0 \quad , \quad \hat{\boldsymbol{\rho}}_1 \cdot \hat{\boldsymbol{\imath}} = \pm 1 \quad , \\ &B = \frac{\mu \rho_1^\eta}{(1-\mu)\hat{\boldsymbol{\rho}}_1 \cdot \hat{\boldsymbol{\imath}}} \left(1 + \frac{\rho_1 \, \hat{\boldsymbol{\rho}}_1 \cdot \hat{\boldsymbol{\imath}} - 1}{|\rho_1 \, \hat{\boldsymbol{\rho}}_1 \cdot \hat{\boldsymbol{\imath}} - 1|^3} \right) + \rho_1^{\eta-2} - \frac{\rho_1^{\eta+1}}{1-\mu} \end{aligned} \tag{4.8}$$

In particular, the first two conditions of Eq. (4.8) state that the collinear points are located on the x-axis of the rotating frame, and three different families may be recognized as in the circular case, see Fig. 3.5.

Similarly to the previous case of triangular points, the position of the three classical Lagrangian points L_1, L_2, and L_3 is recovered by setting $B = 0$. If, instead, the propulsion system is turned on ($B \neq 0$), the third relation in Eq (4.8) yields the constant value of modified sail lightness number B required to maintain an AEP at a distance ρ_1 from the massive body P_1. As for the triangular points, the formal coincidence of Eqs. (3.12) and (3.13) with Eq. (4.8) results in an extension of Figs. 3.6–3.8 to the elliptic case by formally substituting β with B.

4.3.3 Displaced Points

The displaced points are the AEPs that do not belong to the orbital plane of the two celestial bodies, see Fig. 3.2. By means of an analysis of Eq. (4.5), they

would correspond to the points that satisfy the equation with d_k, d_i and d_ρ are all different from zero.

Taking the dot product of Eq. (4.5) with $\hat{\boldsymbol{k}}$, $\hat{\boldsymbol{\imath}}$ and $\hat{\boldsymbol{\jmath}}$, and using Eq. (4.6) yield

$$\boldsymbol{\rho}_1 \cdot \hat{\boldsymbol{\jmath}} = 0 \quad , \quad \frac{\mu}{\rho_2^3} = \mu - (1 + e\,\cos\nu)\,\boldsymbol{\rho}_1 \cdot \hat{\boldsymbol{\imath}} \quad ,$$
$$B = \rho_1^{\eta-2}\left(1 + \frac{\mu}{1-\mu}\,\frac{\rho_1^3}{\rho_2^3} + \frac{e\,\cos\nu\,\rho_1^3}{1-\mu}\right) \tag{4.9}$$

Equation (4.9) states that, for a generalized sail, a displaced equilibrium point may exist only if $e = 0$, that is, in a CR3BP only. This conclusion, which is independent of the value of η, extends the results discussed by Baoyin and McInnes [54] for a Solar Sail (namely, $\eta = 2$). However, it is important to note that a displaced AEP may still be maintained by means of a feedback attitude control strategy [54], or by means of a low-thrust feedforward control system as suggested by Macdonald et al. [55].

4.4 Thrust Modulation Requirements

As seen in the previous section, fixing the position of an equilibrium point on the admissible loci imposes a constant value of B to be assigned according to Eqs. (4.7) or (4.8). Therefore, as a consequence of Eq. (4.3), a variable value β is necessary to maintain an AEP. In other terms a propulsive acceleration modulation is necessary such that β varies between a minimum value $\beta_{\min}$ and a maximum value $\beta_{\max}$, with a period equal to the orbital period of P_2 around P_1, according to the law

$$\beta = B\left(\frac{1-e^2}{1+e\,\cos\nu}\right)^{\eta-2} \tag{4.10}$$

The corresponding maximum variation of the sail lightness number $\Delta\beta$ in an orbital period is

$$\Delta\beta \triangleq \beta_{\max} - \beta_{\min} = B\left|(1+e)^{\eta-2} - (1-e)^{\eta-2}\right| \tag{4.11}$$

Note that both Eqs. (4.10) and (4.11) state that no variation of β is needed in case $e = 0$ or $\eta = 2$.

Isocontour lines of the function $\Delta\beta = \Delta\beta(e, \eta)$ are drawn, per unit of B, in Fig. 4.4. Figure 4.4(a) shows that $\Delta\beta$ is an increasing function of the eccentricity e and, as expected, is zero in the circular case ($e = 0$). In particular, for sufficiently small eccentricities, as in the Sun-(Earth+Moon) problem where $e = e_\oplus = 0.01671022$, $\mu = \mu_\oplus = 3.0404 \times 10^{-6}$ and $a = a_\oplus = 1.00000011\,\text{AU}$ [56], the ratio $\Delta\beta/B$ is on the order of a few percentage points (about 7% for an Electric Thruster and about 3% for an E-sail), see Fig. 4.4(b). Also note that, in accordance with the literature [51, 54], when $\eta = 2$ the variation in sail lightness number $\Delta\beta$ is zero for all values of eccentricity.

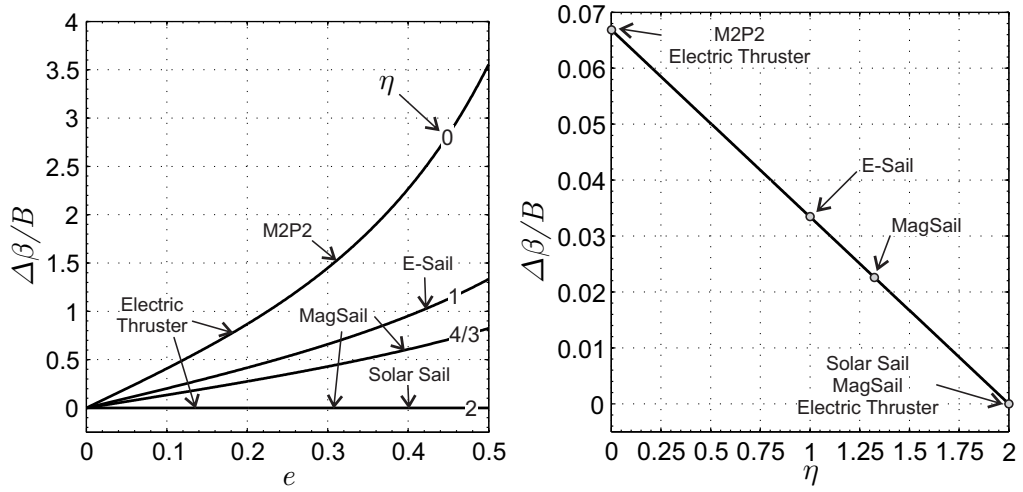

(a) $e \in [0,\, 0.5)$ and $\eta \in \{0,\, 1,\, 4/3,\, 2\}$. (b) Sun-(Earth+Moon) system ($e = e_{\oplus}$).

Figure 4.4: Sail lightness number variation $\Delta\beta$, per unit of B, as a function of e and η, see Eq. (4.11).

4.5 Linear Stability Analysis

The linear stability around a generic AEP is now studied in order to better characterize the dynamical behavior of a spacecraft equipped with a Generalized Sail in an ER3BP.

Let $\boldsymbol{r}_0$ be the dimensionless vector defining the position of a generic AEP and introduce the transformation $\boldsymbol{r} = \boldsymbol{r}_0 + \delta\boldsymbol{r}$. The variational equation of motion is obtained by linearizing Eq. (4.2) around $\boldsymbol{r}_0$, similarly to the circular case. The result is

$$\delta\boldsymbol{r}'' = g(\boldsymbol{K} + \boldsymbol{K}_P)^{\mathrm{T}} \cdot \delta\boldsymbol{r} - 2\boldsymbol{E} \cdot \delta\boldsymbol{r}' \tag{4.12}$$

where $\boldsymbol{K}$, $\boldsymbol{K}_P$, and $\boldsymbol{E}$ are second-order tensors defined by

$$\boldsymbol{K} \triangleq \nabla \left[-\frac{1-\mu}{\rho_1^3}\boldsymbol{\rho}_1 - \frac{\mu}{\rho_2^3}\boldsymbol{\rho}_2 + B\frac{1-\mu}{\rho_1^{\eta+1}}\boldsymbol{\rho}_1 - \hat{\boldsymbol{k}} \times \left(\hat{\boldsymbol{k}} \times \boldsymbol{r}\right) \right] \Bigg|_{\boldsymbol{r}_0} \tag{4.13}$$

$$\boldsymbol{K}_P \triangleq \nabla \left[-e\cos\nu \, \left(\boldsymbol{r} \cdot \hat{\boldsymbol{k}}\right) \hat{\boldsymbol{k}} \right] \Big|_{\boldsymbol{r}_0} \tag{4.14}$$

$$\boldsymbol{E} \cdot \boldsymbol{r} \triangleq \hat{\boldsymbol{k}} \times \boldsymbol{r} \tag{4.15}$$

Note that Eqs. (4.13) and (4.15) are formally similar to the corresponding Eqs. (3.19) and (3.20) for the circular problem. Consequently, the components of

$\boldsymbol{K}$ and $\boldsymbol{E}$ in the pulsating reference frame $\mathcal{T}_P$ are

$$\mathbb{K} \triangleq [\boldsymbol{K}]_{\mathcal{T}_P} = \begin{bmatrix} k_{11} & k_{12} & k_{13} \\ k_{21} & k_{22} & k_{23} \\ k_{31} & k_{32} & k_{33} \end{bmatrix} \quad , \quad \mathbb{E} \triangleq [\boldsymbol{E}]_{\mathcal{T}_P} = \begin{bmatrix} 0 & -1 & 0 \\ 1 & 0 & 0 \\ 0 & 0 & 0 \end{bmatrix} \tag{4.16}$$

where k_{ij} are provided in Appendix B for each family of AEP, by formally substituting β with B. In addition, the components of $\boldsymbol{K}_P$ are

$$\mathbb{K}_P \triangleq [\boldsymbol{K}_P]_{\mathcal{T}_P} = \begin{bmatrix} 0 & 0 & 0 \\ 0 & 0 & 0 \\ 0 & 0 & -e\cos\nu \end{bmatrix} \tag{4.17}$$

since $\boldsymbol{K}_P = -e\cos\nu\,\hat{\boldsymbol{k}}\hat{\boldsymbol{k}}$, see Eq. (4.14).

Introducing the state vector

$$[\boldsymbol{\xi}]_{\mathcal{T}_P} = \left[\delta\boldsymbol{r}\cdot\hat{\boldsymbol{\imath}},\ \delta\boldsymbol{r}\cdot\hat{\boldsymbol{\jmath}},\ \delta\boldsymbol{r}\cdot\hat{\boldsymbol{k}},\ \delta\boldsymbol{r}'\cdot\hat{\boldsymbol{\imath}},\ \delta\boldsymbol{r}'\cdot\hat{\boldsymbol{\jmath}},\ \delta\boldsymbol{r}'\cdot\hat{\boldsymbol{k}}\right]^{\mathrm{T}} \tag{4.18}$$

the linearized equation of motion (4.12) is written as

$$\left[\boldsymbol{\xi}'\right]_{\mathcal{T}_P} = \mathbb{A}_e\,[\boldsymbol{\xi}]_{\mathcal{T}_P} \tag{4.19}$$

with

$$\mathbb{A}_e = \begin{bmatrix} \mathbb{O} & \mathbb{I} \\ g(\mathbb{K}+\mathbb{K}_P)^{\mathrm{T}} & -2\,\mathbb{E} \end{bmatrix} \tag{4.20}$$

where $\mathbb{O}$ is a 3×3 zero matrix, $\mathbb{I}$ is a 3×3 identity matrix, while $\mathbb{K}$, $\mathbb{K}_P$, and $\mathbb{E}$ are given in Eqs. (4.16) and (4.17).

Equation (4.19) with (4.20) constitutes a system of linear, non-autonomous, homogeneous, periodic differential equations. The stability analysis of the system in Eq. (4.20) may be, therefore, addressed with the aid of Floquet theory, by calculating the eigenvalues of the monodromy matrix $\mathbb{M} = \mathbb{F}(2\pi)$, where $\mathbb{F}(\nu)$ is the fundamental matrix solution of the system (4.19) with $\mathbb{F}(0)$ corresponding to the 6×6 identity matrix, see Appendix D. The analysis can be performed using different combinations of μ and e. For a given system of attractors (namely, a pair (μ, e)), stability maps[2] are built to check the stability of an AEP in the plane (η, ρ_1). In the following analysis it is useful to distinguish between triangular and collinear points.

4.5.1 Stability of Triangular Points

For triangular points the entries of $\mathbb{K}$-matrix are provided by Eqs. (B.5)–(B.9). To simplify the numerical analysis, it is useful introduce an auxiliary pulsating

[2]The accuracy of the stability maps was checked by comparing the results with some solutions available in the literature both for the classic problem (namely, $a_{\mathrm{P}} = 0$, see [11, 40, 41, 49]) and for the photogravitational problem where $\eta = 2$ [51].

rotating coordinates frame $\mathcal{T}_R(C; x_R/\ell, y_R/\ell, z/\ell)$, according to Refs. [11,42,46], with unit vectors $\hat{\boldsymbol{\imath}}_R$, $\hat{\boldsymbol{\jmath}}_R$, and $\hat{\boldsymbol{k}}$, obtained by a counterclockwise rotation of $\mathcal{T}_P$ around $\hat{\boldsymbol{k}}$ of an angle ψ such that

$$\psi \triangleq \frac{1}{2} \arctan\left(\frac{2\,k_{12}}{k_{11} - k_{22}}\right) \tag{4.21}$$

where k_{11}, k_{22}, and k_{12} are given by Eqs. (B.5), (B.6) and (B.8), respectively. The projection of the linearized equation (4.19) in the new coordinates frame gives

$$\left[\delta \boldsymbol{r}''\right]_{\mathcal{T}_R} = g([\boldsymbol{K}]^{\mathrm{T}}_{\mathcal{T}_R} + [\boldsymbol{K}_P]^{\mathrm{T}}_{\mathcal{T}_R}) \cdot [\delta \boldsymbol{r}]_{\mathcal{T}_R} - 2\,[\boldsymbol{E}]_{\mathcal{T}_R} \cdot \left[\delta \boldsymbol{r}'\right]_{\mathcal{T}_R} \tag{4.22}$$

Note[3] that while $[\boldsymbol{E}]_{\mathcal{T}_R} \equiv [\boldsymbol{E}]_{\mathcal{T}_P}$ and $[\boldsymbol{K}_P]_{\mathcal{T}_R} \equiv [\boldsymbol{K}_P]_{\mathcal{T}_P}$, the projection of the second-order tensor $\boldsymbol{K}$ on the auxiliary frame $\mathcal{T}_R$ is a diagonal matrix

$$[\boldsymbol{K}]_{\mathcal{T}_R} = \begin{bmatrix} \widetilde{k}_{11} & 0 & 0 \\ 0 & \widetilde{k}_{22} & 0 \\ 0 & 0 & k_{33} \end{bmatrix} \tag{4.23}$$

where

$$\widetilde{k}_{11} = \frac{1}{2}\left[3 + (1-\mu)(\eta - 2)\left(1 - \frac{1}{\rho_1^3}\right) + \sqrt{D}\right] \tag{4.24}$$

$$\widetilde{k}_{22} = \frac{1}{2}\left[3 + (1-\mu)(\eta - 2)\left(1 - \frac{1}{\rho_1^3}\right) - \sqrt{D}\right] \tag{4.25}$$

with

$$\begin{aligned} D \triangleq\ & 9[1 - \mu(1-\mu)(4 - \rho_1^2)] + \\ & (1-\mu)(\eta-2)\left(1 - \frac{1}{\rho_1^3}\right)\left[6 - 3\mu(4-\rho_1^2) + (1-\mu)(\eta-2)\left(1 - \frac{1}{\rho_1^3}\right)\right] \end{aligned} \tag{4.26}$$

In particular, for the classical triangular Lagrangian points L_4 and L_5 (corresponding to $\rho_1 = 1$), or for the special case in which the propulsion system is a Solar Sail ($\eta = 2$), Eqs. (4.24) and (4.25) reduce to $\widetilde{k}_{11} = 3/2\,[1 + \sqrt{1 - 3\,\mu\,(1-\mu)}]$ and $\widetilde{k}_{22} = 3/2\,[1 - \sqrt{1 - 3\,\mu\,(1-\mu)}]$. This result is in accordance with Refs. [42,45,46] for the classical Lagrangian points, and with Ref. [51] for the photogravitational case ($\eta = 2$).

The numerical analysis can be further simplified by noting that the component along z of the linearized equation of motion (4.22) is

$$(\hat{\boldsymbol{k}} \cdot \delta \boldsymbol{r}'') + \hat{\boldsymbol{k}} \cdot \delta \boldsymbol{r} = 0 \tag{4.27}$$

[3] If $\mathbb{T}$ is the rotation (orthogonal) matrix from $\mathcal{T}_P$ to $\mathcal{T}_R$, the relation between the components of the second order tensor $\boldsymbol{U}$ in the two different coordinate frames is $[\boldsymbol{U}]_{\mathcal{T}_R} = \mathbb{T} \cdot [\boldsymbol{U}]_{\mathcal{T}_P} \cdot \mathbb{T}^{\mathrm{T}}$.

because k_{33} is given by Eq. (B.7) and $[\boldsymbol{E}]_{\mathcal{T}_P}$ is obtained from Eq. (4.16). As a result, the linearized equation of motion along the z-axis coincides with the equation of a harmonic oscillator with a period equal to 2π. Therefore, the motion along the z-axis is uncoupled from that in the (x, y)-plane, and it is marginally stable [40, 45, 48]. Such a motion may therefore be disregarded in the stability analysis.

As a consequence, a reduced-order state vector may be introduced such that

$$\left[\widetilde{\boldsymbol{\xi}}\right]_{\mathcal{T}_R} \triangleq \left[\delta\boldsymbol{r}\cdot\hat{\boldsymbol{\imath}}_R,\ \delta\boldsymbol{r}\cdot\hat{\boldsymbol{\jmath}}_R,\ \delta\boldsymbol{r}'\cdot\hat{\boldsymbol{\imath}}_R,\ \delta\boldsymbol{r}'\cdot\hat{\boldsymbol{\jmath}}_R\right]^{\mathrm{T}} \tag{4.28}$$

thus reducing from 6 to 4 the number of scalar differential equations involved in the numerical simulations. The linearized equations of motion in the (x, y)-plane take the form

$$\left[\widetilde{\boldsymbol{\xi}}'\right]_{\mathcal{T}_R} = \mathbb{A}_t \left[\widetilde{\boldsymbol{\xi}}\right]_{\mathcal{T}_R} \tag{4.29}$$

where

$$\mathbb{A}_t \triangleq \begin{bmatrix} 0 & 0 & 1 & 0 \\ 0 & 0 & 0 & 1 \\ g\,\widetilde{k}_{11} & 0 & 0 & 2 \\ 0 & g\,\widetilde{k}_{22} & -2 & 0 \end{bmatrix} \tag{4.30}$$

with $\widetilde{k}_{11}$ and $\widetilde{k}_{22}$ given by Eqs. (4.24)-(4.25). Also note that the matrix $\mathbb{A}_t$ satisfies the Hale's property-E in Eq. (D.5), if $\mathbb{S} = \mathrm{diag}(1, -1, -1, 1)$. Therefore Eq. (D.6) may be used to reduce the computational time and increase the accuracy in numerical simulations.

Figure 4.5 shows the stability maps for the triangular points in the Sun-(Earth+Moon) system. As expected from Fig. 2.3, the classical Lagrangian (equilateral) points, corresponding to $\rho_1 = 1$, are stable for any value of η. Also note that when $\eta = 2$ all the triangular points are stable. These results are in agreement with the photogravitational case studied by Markellos et al. [51], but not with Baoyin and McInnes [54]. The reason of such a discrepancy lies in different assumptions made on the propulsive acceleration direction (similarly to the discrepancy with Morimoto et al. [16] in the circular case). In fact, while for Baoyin and McInnes the thrust direction remains constant (therefore, the gradient is zero), for a Generalized Sail the thrust is always radial with respect to P_1 and, accordingly, $\nabla\hat{\boldsymbol{\rho}}_1$ is different from zero, see Eq. (4.13).

Figure 4.5 also shows that unlike the circular case (see Fig 3.13), the stability region is not uniform, since it contains some *instability stripes* whose position and width heavily depend on the attractors system through the values of μ and e. This is clearly illustrated in Fig. 4.6, where the topology of stability maps is shown for different pairs $(\mu,\, e)$. In particular note that for $e = 0$ the stripes

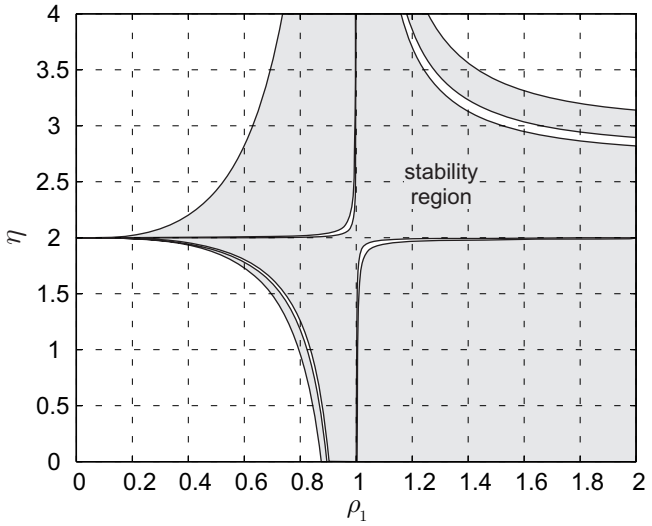

Figure 4.5: Stability map for triangular AEPs in the Sun-(Earth+Moon) system.

collapse, see Fig. 4.6(a), and the result of the circular problem is recovered, see Fig. 3.13(a).

At a first sight, the main effect of the eccentricity is a variation in the width of the instability stripes, whereas the main effect of the mass parameter is the variation of both the number of stripes and the position of the outside borders of the stability regions. Actually, the combined effect of eccentricity and mass parameter is more complicated, and a relationship between shape of stability map and pair (μ, e) is not currently available.

4.5.2 Stability of Collinear Points

For collinear points, the entries of the matrix $\mathbb{K}$ are given in Eqs. (B.11)–(B.14) or Eqs. (B.17)–(B.20). The matrix $\mathbb{A}_e$ in Eq. (4.20) satisfies the Hale's property-E defined in Eq. (D.5) with $\mathbb{S} = \text{diag}(1, -1, 1, -1, 1, -1)$. Consequently, the computational time to calculate the monodromy matrix is reduced by using Eq. (D.6), similarly to the triangular points.

Figures 4.7–4.9 show the stability maps for the collinear AEPs in various systems corresponding to different pair (μ, e). Note that for both L_1-type and L_3-type AEPs the stability region is unique, whereas for L_2-type points[4] there exist more stability regions alternated with instability stripes, see Figs. 4.7(c), 4.8(c), and 4.9(c).

[4]Simulations show that for L_2-type points there exists a stability region (not shown in Figs. 4.7(c), 4.8(c), and 4.9(c)) for distances close to $\rho_1 = 1$ and very high values of η, that depend on the value if μ. This result is in agreement with a similar conclusion obtained for the circular problem, see in particular Figs. 3.9, 3.14(c), and 3.15.

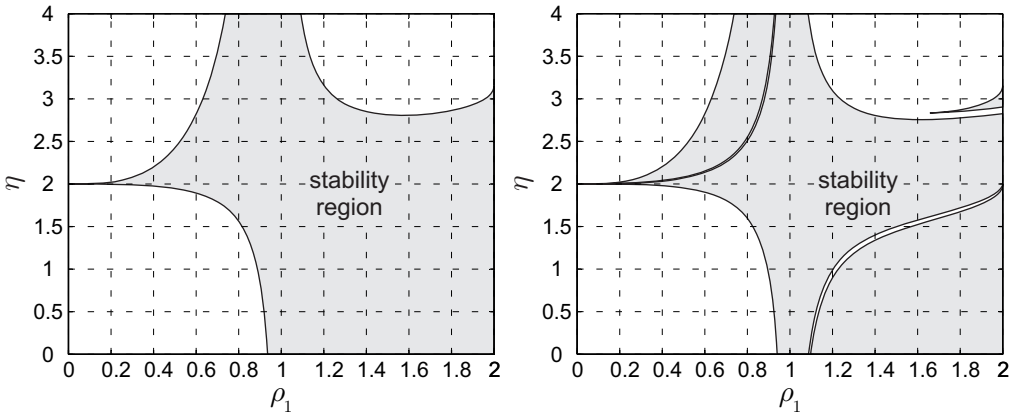

(a) $\mu = 0.01$ and $e = 0$.

(b) $\mu = 0.01$ and $e = e_\oplus$.

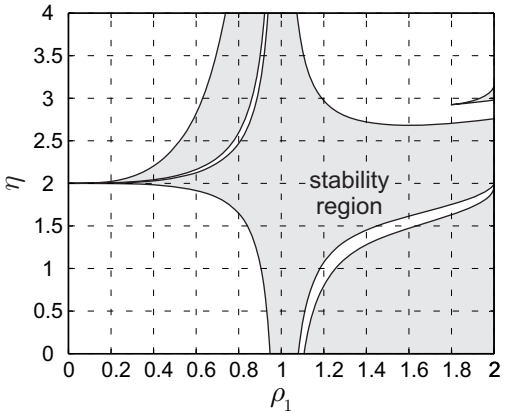

(c) $\mu = 0.01$ and $e = 0.05$.

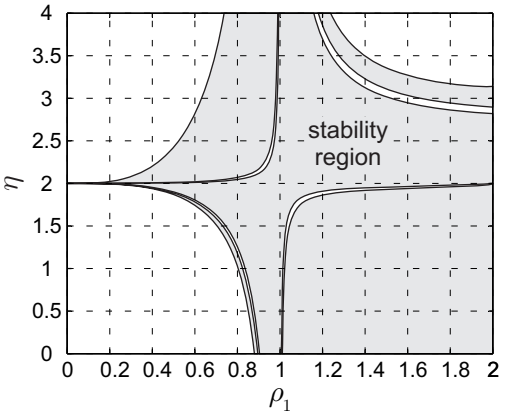

(d) $\mu = 0.0001$ and $e = e_\oplus$.

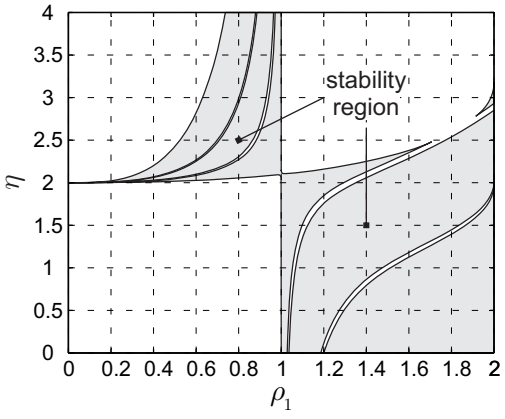

(e) $\mu = \mu^\star$ and $e = e_\oplus$.

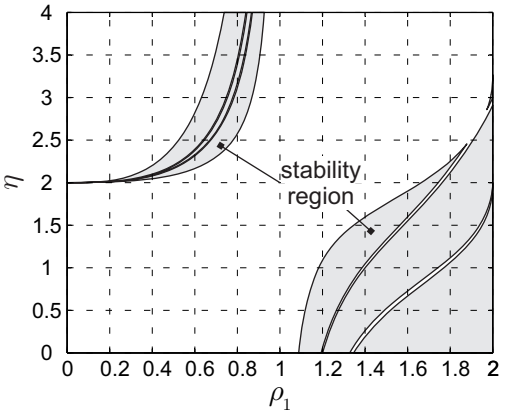

(f) $\mu = 0.1$ and $e_\oplus$.

Figure 4.6: Topology of the stability maps for triangular AEPs as a function of μ and e.

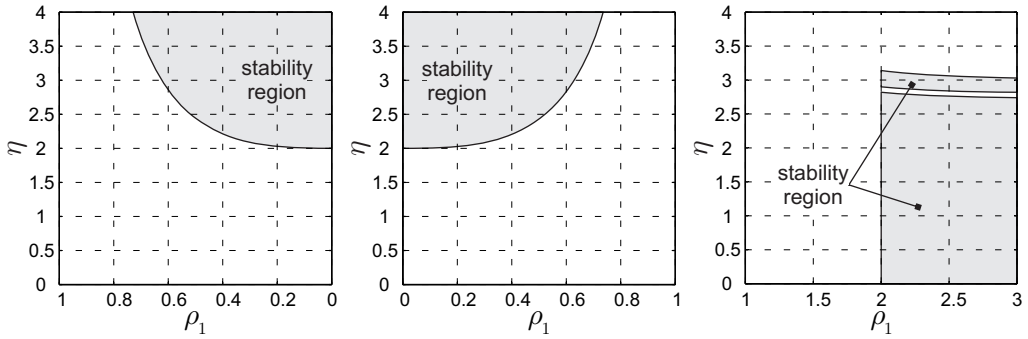

(a) L_3-type. (b) L_1-type. (c) L_2-type.

Figure 4.7: Stability maps for collinear AEPs in the Sun-(Earth+Moon) system.

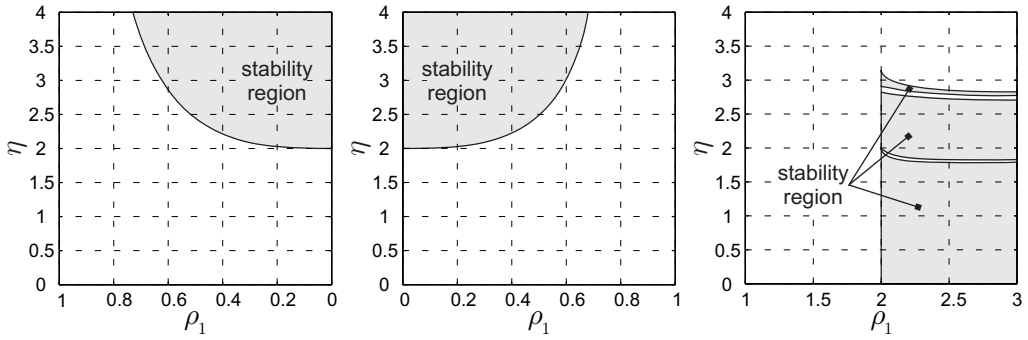

(a) L_3-type. (b) L_1-type. (c) L_2-type.

Figure 4.8: Stability maps for collinear AEPs for $\mu = 0.01$ and $e = e_{\oplus}$.

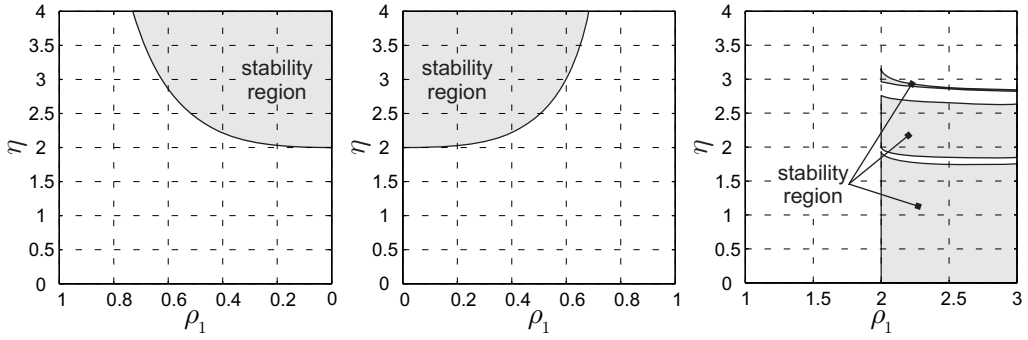

(a) L_3-type. (b) L_1-type. (c) L_2-type.

Figure 4.9: Stability maps for collinear AEPs for $\mu = 0.01$ and $e = 0.05$.

Simulations also show that the stability maps for L_1-type and L_3-type AEPs are essentially insensitive to a variation of the parameters μ and e. On the other hand, for L_2-type points, the number of stripes increases with the mass parameter μ, and the width of such stripes increases too, for a given value of μ, with the eccentricity e, similarly to the triangular points. In particular, when $e = 0$ the instability stripes collapse into a line, according to Fig. 3.15.

Chapter 5

Artificial Equilibrium Points for an Electric Solar Wind Sail with Constant Attitude

So far the assumption of radial thrust has been used to show how it is possible to create *Artificial Equilibrium Point*s by means of the propulsive acceleration provided by a Generalized Sail. In this chapter the hypothesis of radial thrust is left, and the existence of Artificial Equilibrium Points maintained by a spacecraft equipped with an *Electric Solar Wind Sail* is studied. The study is addressed within an *Elliptic Restricted Three-Body Problem* where the system of main celestial bodies is constituted by the Sun and a planet. A discussion of the stability of the Artificial Equilibrium Points is also provided.

5.1 Introduction

An E-Sail[1] is an innovative continuous-thrust propulsion system invented in 2004 by Pekka Janhunen [6] of the Finnish Meteorological Institute. Such a propulsion system is known to be able to provide a continuous propulsive acceleration by means of Coulomb's interaction of a number of positively charged tethers with the solar wind plasma stream [6, 57], see Fig. 5.1.

Similar to Solar Sails [35, 54], creating and maintaining AEPs in the R3BP is one of the mission scenario in which an E-Sail can exploit its natural potential. Indeed, in such a problem the acceleration resulting from the sum of centrifugal and gravitational forces can be balanced, for a theoretically unlimited time period, by means of the continuous acceleration provided by the E-Sail.

A thorough analysis involving the location and stability of AEPs has been addressed in Chapters 3 and 4 for Generalized Sail based spacecraft, which includes also spacecraft equipped with E-Sails providing a purely radial thrust with respect to the Sun. However, in a more general case, the direction of the E-sail

[1] See `www.electric-sailing.fi`.

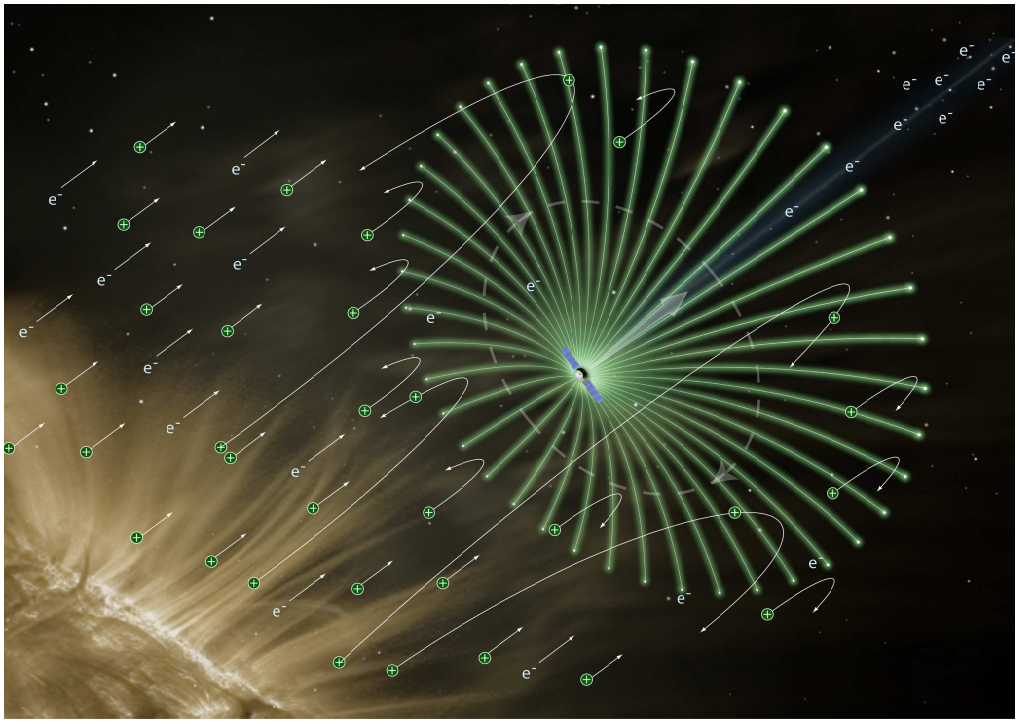

Figure 5.1: Artistic impression of an E-Sail (courtesy of A. Szames).

propulsive acceleration may be inclined (within prescribed limits) with respect to the radial direction, and a transverse acceleration component may be generated. The latter, in its turn, introduces an additional degree of freedom that can be exploited to expand the region of admissible AEPs. The study of such a region is the subject of this chapter, whose aim is to extend the result of Chapter 4 by removing the assumption of radial direction for the propulsive acceleration.

5.2 Equations of Motion

Consider the motion of a spacecraft equipped with an E-Sail propulsion system, under the gravitational effects of the Sun and a planet with masses m_1 and m_2, respectively. The two celestial bodies cover elliptic orbits around their center-of-mass C (see Fig. 5.2), and the time-dependent distance between the two celestial bodies is $\ell = a\,(1-e^2)\,g$, with g defined in Eq. (2.2)

According to Janhunen et al. [58], the propulsive acceleration for an E-sail based spacecraft is given by

$$\boldsymbol{a}_{\mathrm{P}} = \beta \frac{G\,m_1}{a\,\ell\,\rho_1}\,\hat{\boldsymbol{a}}_{\mathrm{P}} \qquad \text{with} \qquad \beta \triangleq \frac{a_c}{G\,m_1/a^2} \tag{5.1}$$

where $\ell\rho_1$ is the distance with respect to the Sun and $\hat{\boldsymbol{a}}_{\mathrm{P}} \triangleq \boldsymbol{a}_{\mathrm{P}}/\|\boldsymbol{a}_{\mathrm{P}}\|$. Moreover,

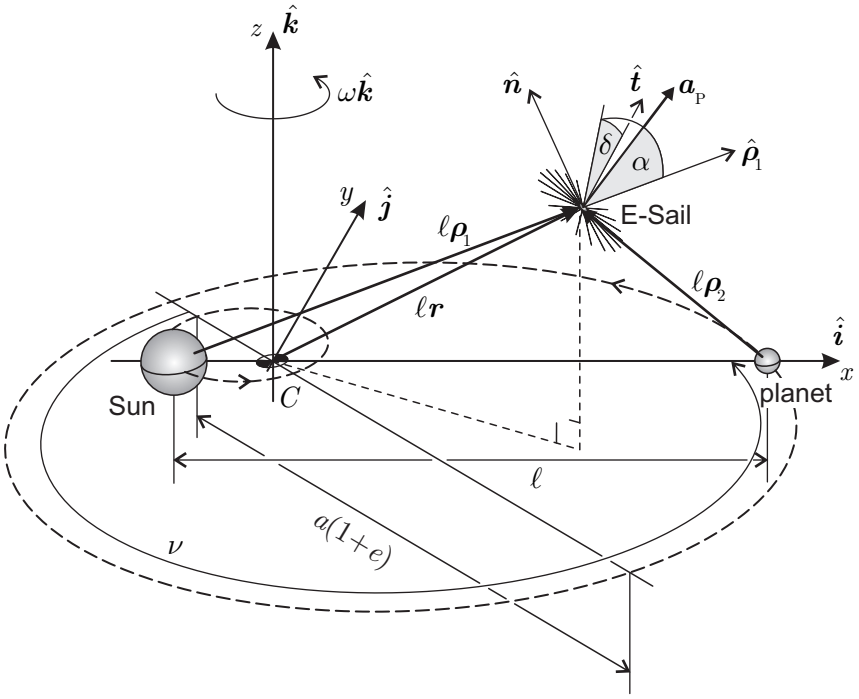

Figure 5.2: E-Sail in the Elliptic Restricted Three-Body Problem.

similarly to Eqs. (2.15) and (2.17), β represents the sail lightness number and a_c is the characteristic acceleration (that is, the acceleration modulus measured at the distance a from the Sun).

With reference to Fig. 5.2, the equation of motion of the spacecraft in the synodic frame can be written in dimensionless form using the true anomaly ν as the independent variable, see Appendix A

$$\boldsymbol{r}'' + 2\,\hat{\boldsymbol{k}} \times \boldsymbol{r}' = g\left[-\boldsymbol{f} + B\,\frac{1-\mu}{\rho_1}\,\hat{\boldsymbol{a}}_{\mathrm{P}} - e\,\cos\nu\,\left(\boldsymbol{r}\cdot\hat{\boldsymbol{k}}\right)\,\hat{\boldsymbol{k}}\right] \tag{5.2}$$

where $\boldsymbol{f}$ is the opposite of the sum of gravitational and centrifugal accelerations, that is

$$\boldsymbol{f} \triangleq \frac{1-\mu}{\rho_1^3}\,\boldsymbol{\rho}_1 + \frac{\mu}{\rho_2^3}\,\boldsymbol{\rho}_2 + \hat{\boldsymbol{k}} \times \left(\hat{\boldsymbol{k}} \times \boldsymbol{r}\right) \tag{5.3}$$

while $B \geq 0$ corresponds to the modified sail lightness number defined in Eq. (4.3) with $\eta = 1$

$$B \triangleq \beta\left(\frac{1-e^2}{1+e\,\cos\nu}\right) \tag{5.4}$$

Introduce now a Radial-Transversal-Normal (RTN) reference frame, whose unit vectors are defined as (see Fig. 5.2)

$$\hat{\boldsymbol{\rho}}_1 \triangleq \frac{\boldsymbol{\rho}_1}{\rho_1} \quad , \quad \hat{\boldsymbol{t}} \triangleq \frac{\hat{\boldsymbol{k}} \times \hat{\boldsymbol{\rho}}_1}{\|\hat{\boldsymbol{k}} \times \hat{\boldsymbol{\rho}}_1\|} \quad , \quad \hat{\boldsymbol{n}} \triangleq \hat{\boldsymbol{\rho}}_1 \times \hat{\boldsymbol{t}} \tag{5.5}$$

The orientation of the propulsive acceleration vector $\boldsymbol{a}_\mathrm{P}$ is defined by means of the cone angle α and the clock angle δ, where α is the angle between $\hat{\boldsymbol{a}}_\mathrm{P}$ and $\hat{\boldsymbol{\rho}}_1$, while δ is the angle between $\hat{\boldsymbol{t}}$ and the projection of $\hat{\boldsymbol{a}}_\mathrm{P}$ onto the $(\hat{\boldsymbol{t}}, \hat{\boldsymbol{n}})$-plane. Note that, according to Refs. [58, 59], the cone angle is upper constrained to prevent possible mechanical instabilities, and the maximum value of α is estimated to be about 30 deg. The thrust vectoring capability of an E-Sail is therefore described by two control variables, namely $\alpha \in [0,\, 30]$ deg and $\delta \in [0,\, 360]$ deg.

In what follows the study of AEPs will be performed under the assumption that the sail cone and clock angles are both maintained constant, that is $\alpha = \overline{\alpha}$ and $\delta = \overline{\delta}$, where the overbar symbol is added to emphasize a constant value. In this case, the direction of $\hat{\boldsymbol{a}}_\mathrm{P}$ remains constant with respect to the RTN reference frame, namely

$$\hat{\boldsymbol{a}}_\mathrm{P} = \cos\overline{\alpha}\,\hat{\boldsymbol{\rho}}_1 + \sin\overline{\alpha}\,\left(\cos\overline{\delta}\,\hat{\boldsymbol{t}} + \sin\overline{\delta}\,\hat{\boldsymbol{n}}\right) \tag{5.6}$$

This corresponds to a generalization of the results discussed in Chapter 4, where the propulsive acceleration was assumed to be always in the radial direction (that is, $\alpha \equiv 0$ deg).

5.3 Artificial Equilibrium Points

The positions of the AEPs are obtained, from Eq. (5.2), by enforcing the stationary conditions $\boldsymbol{r}'' = 0$ and $\boldsymbol{r}' = 0$. Therefore, the AEPs positions turn out to be the solutions of the vectorial equation

$$B\,\frac{1-\mu}{\rho_1}\,\hat{\boldsymbol{a}}_\mathrm{P} - e\,\cos\nu\,\left(\boldsymbol{r}\cdot\hat{\boldsymbol{k}}\right)\,\hat{\boldsymbol{k}} - \boldsymbol{f} = 0 \tag{5.7}$$

Recalling that, by assumption, the cone and clock angle are maintained constant, Eq. (5.7) states that AEPs are possible only if the two following conditions are met: 1) $e\,(\boldsymbol{r}\cdot\hat{\boldsymbol{k}}) = 0$, and 2) B is constant. The first condition states that, if $e \neq 0$, any AEP lies in the orbital plane of two attractors and $\hat{\boldsymbol{a}}_\mathrm{P} = \hat{\boldsymbol{f}} \triangleq \boldsymbol{f}/\|\boldsymbol{f}\|$, see Eq. (5.7). Such a constraint univocally defines the values of cone and clock angles, $\overline{\alpha} = \alpha_0$ and $\overline{\delta} = \delta_0$, necessary for maintaining an AEP, see Eqs. (5.6) and (5.3).

In other terms, an AEP is defined through the equations

$$\hat{\boldsymbol{a}}_{\mathrm{P}_0} = \hat{\boldsymbol{f}}_0 \qquad , \qquad B_0 = \frac{\rho_{1_0}}{1-\mu}\|\boldsymbol{f}_0\| \tag{5.8}$$

where the subscript 0 means that the corresponding variable is evaluated when $\boldsymbol{r} = \boldsymbol{r}_0$, $\overline{\alpha} = \alpha_0$, and $\overline{\delta} = \delta_0$. In particular, the second relation in Eq. (5.8) states that the modified lightness number B is a constant. Therefore, from Eqs. (5.1) and (5.4), the characteristic acceleration a_c is a function of the true anomaly

through the relationship

$$a_c = B_0 \frac{G\,m_1}{a^2}\left(\frac{1+e\cos\nu}{1-e^2}\right) \tag{5.9}$$

with a maximum value $a_{c_{\max}}$ given by

$$a_{c_{\max}} = B_0 \frac{G\,m_1}{a^2}\left(\frac{1+e}{1-e^2}\right) \tag{5.10}$$

Note that the (dimensionless) maximum variation in characteristic acceleration Δa_c is a function of the eccentricity e only, that is

$$\frac{\Delta a_c}{a_{c_{\max}}} = \frac{2\,e}{1+e} \tag{5.11}$$

From a practical point of view, the required variation of a_c for an E-Sail based spacecraft can be achieved by means of a suitable adjustment of the tethers' voltage [58]. Note that, in the special case of the CR3BP ($e = 0$), Eq. (5.7) does not depend on the true anomaly, and AEP may exist also outside the orbital plane of the two attractors (similarly to what happens for a Generalized Sail) with a constant value of a_c, see Eq. (5.9).

Figures 5.3 and 5.4 show the propulsive performance required to generate an AEP in a region close to the classical Lagrange point L_4 and L_1 for the Sun-(Earth+Moon) system. The solid lines represent the isocontour lines of the max-

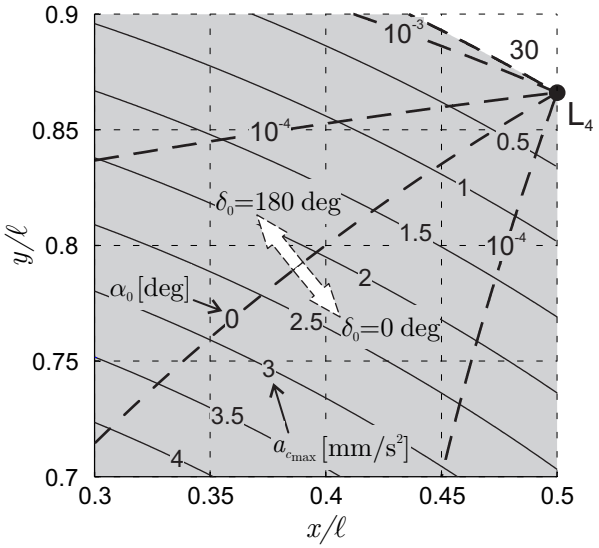

Figure 5.3: E-Sail performance for AEPs close to L_4 in the Sun-(Earth+Moon) system.

imum characteristic acceleration necessary to maintain an AEP, see Eq. (5.10),

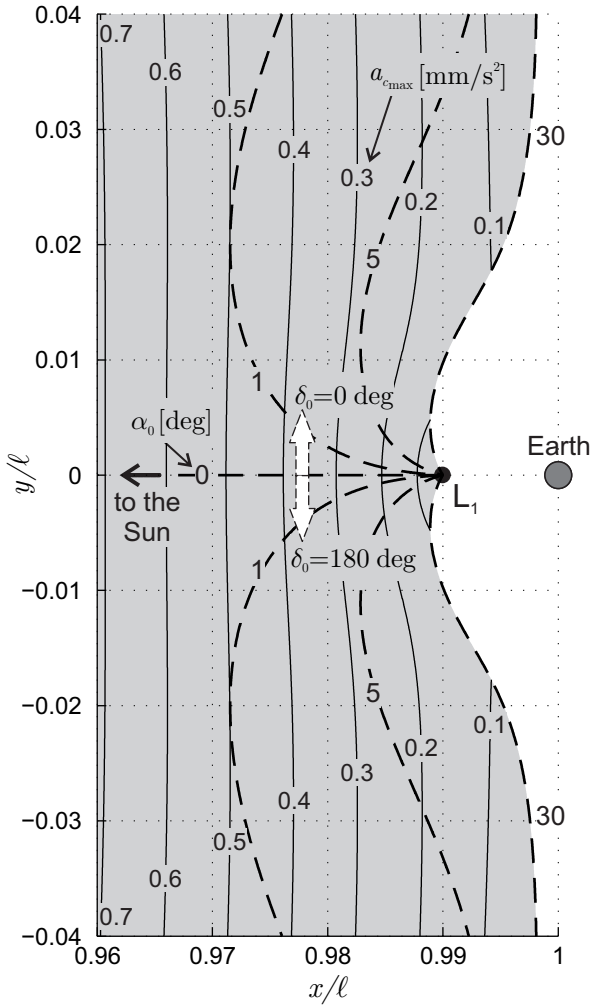

Figure 5.4: E-Sail performance for AEPs close to L_1 in the Sun-(Earth+Moon) system.

and dashed lines correspond to isocontour lines of the required sail cone angle α_0. The shaded region highlights the set of AEPs achievable with a sail cone angle $\alpha_0 \leq 30\,\text{deg}$. Because the propulsive acceleration direction must belong to the plane of motion of the attractors, the set of admissible values for δ_0 is restricted to be either 0 deg or 180 deg (arrows in Figs. 5.3 and 5.4 indicate the region corresponding to those values).

The results in Figs. 5.3 and 5.4 demonstrate that the creation of AEPs in the neighborhood of the L_4 and L_1 points in the Sun-(Earth+Moon) system is compatible with the characteristic acceleration of a first generation E-Sail. However, note how a very fine thrust vectoring capability is required, especially in the neighborhood of the L_4 point. Indeed, a small variation in the cone angle

results in a relevant displacement of the actual equilibrium point, thus causing large positioning error, which can affect the stability of the system.

5.4 Linear Stability Analysis

The linear stability of an AEP is now analyzed by introducing the transformation $\boldsymbol{r} = \boldsymbol{r}_0 + \delta\boldsymbol{r}$, where $\delta\boldsymbol{r}$ represents a perturbation in the spacecraft position vector. The variational equation of motion of an E-Sail based spacecraft, obtained by linearizing Eq. (5.2) around $\boldsymbol{r}_0$, is

$$\delta\boldsymbol{r}'' = g\boldsymbol{H}^{\mathrm{T}} \cdot \delta\boldsymbol{r} - 2\,\boldsymbol{E} \cdot \delta\boldsymbol{r}' \tag{5.12}$$

in which $\boldsymbol{E}$ is defined in Eq. (4.15), and $\boldsymbol{H}$ is the second order tensor defined as

$$\boldsymbol{H} = \nabla\left[-\boldsymbol{f} + B\,\frac{1-\mu}{\rho_1}\,\hat{\boldsymbol{a}}_p - e\,\cos\nu\,\left(\boldsymbol{r}\cdot\hat{\boldsymbol{k}}\right)\,\hat{\boldsymbol{k}}\right]\Bigg|_0 \tag{5.13}$$

Note that $\boldsymbol{H}$ is evaluated at the equilibrium condition. An expanded form of $\boldsymbol{H}$, suitable for analytical and numerical purposes, is discussed in Appendix C.

Introducing the state vector defined in Eq. (4.18), the linearized equation of motion takes the form

$$\left[\boldsymbol{\xi}'\right]_{\mathcal{T}_P} = \mathbb{A}_E\,\left[\boldsymbol{\xi}\right]_{\mathcal{T}_P} \tag{5.14}$$

with $\mathbb{E}$ given in Eq. (4.16) and

$$\mathbb{A}_E = \begin{bmatrix} \mathbb{O} & \mathbb{I} \\ g\,\mathbb{H}^{\mathrm{T}} & -2\,\mathbb{E} \end{bmatrix} \quad , \quad \mathbb{H} = \begin{bmatrix} h_{11} & h_{12} & h_{13} \\ h_{21} & h_{22} & h_{23} \\ h_{31} & h_{32} & h_{33} \end{bmatrix} \tag{5.15}$$

where $\mathbb{O}$ and $\mathbb{I}$ are the zero and identity 3×3 matrices, respectively, and h_{ij} is the generic component of the second order tensor $\boldsymbol{H}$ in the synodic reference frame. Equation (5.14) represents a system of first-order differential equation with periodic coefficients (of period 2π), and its stability analysis may be performed numerically with Floquet's theory, see Appendix D.

Numerical simulations show that stable AEPs exist in the plane of motion of the two attractors. For instance, Fig. 5.5 shows examples of those stability regions in the neighborhood of the classical Lagrange points L_4 and L_1 in the Sun-(Earth+Moon) system. In particular, the stability regions are not uniform due to the presence of instability stripes caused by the eccentricity of the Earth's orbit around the Sun. These instability stripes are consistent to those found in Chapter 4 in the special case of radial propulsive acceleration. In fact, when $\alpha = 0\,\mathrm{deg}$, Fig. 5.5(a) reveals the existence of stable triangular points, while Fig. 5.5(b) shows the instability of the L_1-type AEPs.

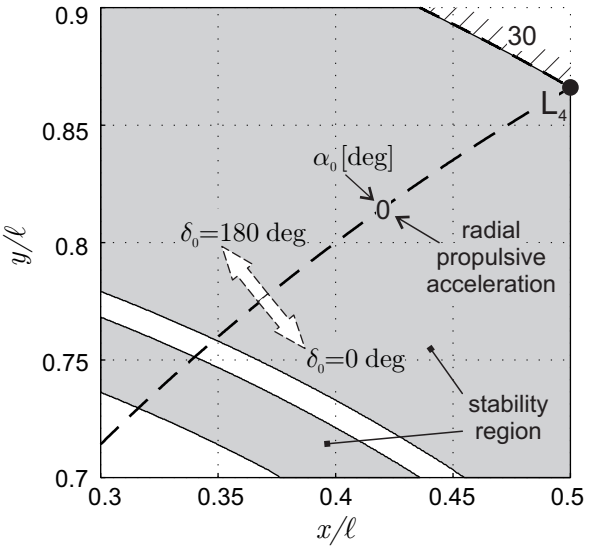

(a) Stability region close to L_4.

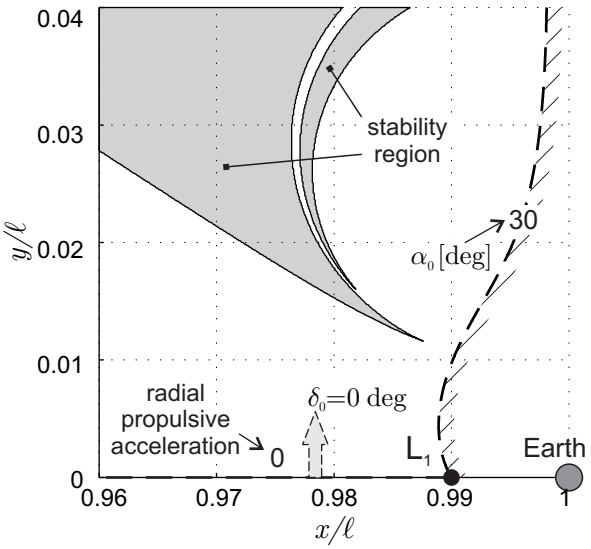

(b) Stability region close to L_1.

Figure 5.5: Stability regions close to the classical equilibrium points L_4 and L_1 in the Sun-(Earth+Moon) system.

Chapter 6

Stabilization and Control of L_1-type Points

The aim of this chapter is to study two techniques for the realization of the so-called *β-control* of the *Artificial Equilibrium Point*s belonging to the family of the L_1-type points obtained by means of Solar Sail based systems. The first technique consists of a purely passive control of the area of the exposed surface based on the inflation/deflation mechanism of a *Solar Balloon*, whereas the second one uses an active control based on the possibility of modifying the reflectivity of the surface by means of *Electrochromic Material Panels*. In both cases, the effect is a variation of the characteristic acceleration of the Solar Sail and, therefore, of the lightness number β.

6.1 Introduction

As shown in Chapters 3 and 4, the continuous radial thrust provided by a Generalized Sail may be used to generate AEPs belonging to well defined loci, see Figs 3.2 and 4.2. Particularly attractive positions for missions toward AEPs are the L_1-type points, which are close to the classical L_1 Lagrange Point. For example, in the Sun-(Earth+Moon) system, these AEPs were suggested as useful locations for space weather observation missions [9, 10, 60] or for geo-engineering missions [61–64].

However, it is known that L_1-type points are in general unstable, as shown in Figs. 3.14(b), 4.7(b), 4.8(b), and 4.9(b). Consequently, a suitable control strategy is necessary to maintain the desired location. From a theoretical point of view, two control strategies are possible: sail attitude control [35, 65] and sail lightness number control [64, 65].

The sail attitude control requires a variation of the sail thrust direction. This may be accomplished by applying a torque to the sail so that its attitude is varied. To this end, in case of Solar Sail, McInnes [19] suggested either to displace the center of mass of the spacecraft with respect to the center of pressure of the Solar

Sail, or to use small reflective rotating vanes at the Solar Sail tips. To the same aim, the Ikaros mission used successfully [66] a Reflectance Control Device based on the possibility of switching on or off liquid crystal devices placed at the sides of the square sail.

The sail lightness number control (usually referred to as β-control [64]) requires a variation of the sail characteristic acceleration. For Solar Sails, this may be accomplished by varying either the sail area or the sail reflectance properties. In case of E-Sails, a suitable variation of the voltage of the tethers may provide the needed variation of characteristic acceleration.

In the following, the concept of β-control for a Generalized Sail is briefly introduced. Then, two techniques fulfilling β-control for Solar Sail based spacecraft are studied.

6.2 The β-control of the L_1-type Points by means of a Generalized Sail

Assume it is possible to vary the modified lightness number B of a Generalized Sail, with the aim to stabilize a L_1-type equilibrium point in an ER3BP. To characterize the dynamical behavior of the spacecraft in presence of control, the equation of motion (4.2) in the pulsating rotating frame is linearized around the L_1-type equilibrium position defined by

$$\boldsymbol{r}_0 \triangleq (\rho_{1_0} - \mu)\hat{\boldsymbol{\imath}} \tag{6.1}$$

obtained by means of a modified sail lightness number B_0 given by Eq. (4.8)

$$B_0 = \frac{\mu \rho_{1_0}^{\eta}}{(1-\mu)} \left[1 - \frac{1}{(1-\rho_{1_0})^2}\right] + \rho_{1_0}^{\eta-2} - \frac{\rho_{1_0}^{\eta+1}}{1-\mu} \tag{6.2}$$

Introducing the transformations $\boldsymbol{r} = \boldsymbol{r}_0 + \delta\boldsymbol{r}$ and $B = B_0 + \delta B$ in Eq. (4.2), the variational equation of motion becomes

$$\delta\boldsymbol{r}'' = g(\boldsymbol{K} + \boldsymbol{K}_P)^{\mathrm{T}} \cdot \delta\boldsymbol{r} - 2\boldsymbol{E} \cdot \delta\boldsymbol{r}' + g\boldsymbol{u}\,\delta B \tag{6.3}$$

where $\boldsymbol{K}$, $\boldsymbol{K}_P$, and $\boldsymbol{E}$ are second-order tensors defined in Eqs.(4.13)–(4.15), while

$$\boldsymbol{u} \triangleq \frac{1-\mu}{\rho_{1_0}^{\eta}}\,\hat{\boldsymbol{\imath}} \tag{6.4}$$

Using the state vector defined in Eq. (4.18), the variational equation of motion in the pulsating coordinate frame is written as

$$\left[\boldsymbol{\xi}'\right]_{\mathcal{T}_P} = \begin{bmatrix} \mathbb{O}_{3\times3} & \mathbb{I}_{3\times3} \\ g\,(\mathbb{K} + \mathbb{K}_P)^{\mathrm{T}} & -2\,\mathbb{E} \end{bmatrix} [\boldsymbol{\xi}]_{\mathcal{T}_P} + \begin{bmatrix} \mathbb{O}_{3\times1} \\ g\,\mathbb{U} \end{bmatrix} \delta B \tag{6.5}$$

While $\mathbb{O}_{n\times m}$ and $\mathbb{I}_{n\times m}$ are the $n \times m$ null and identity matrix, the matrices $\mathbb{K}$, $\mathbb{K}_P$, and $\mathbb{E}$ are defined in Eqs. (4.16) and (4.17) with k_{ij} given in Eqs. (B.17)–(B.20), and the matrix $\mathbb{U}$ contains the components of the vector $\boldsymbol{u}$ in the synodic pulsating coordinate frame, that is

$$\mathbb{U} \triangleq [\boldsymbol{u}]_{\mathcal{T}_P} = \begin{bmatrix} \dfrac{1-\mu}{\rho_{1_0}^{\eta}} & 0 & 0 \end{bmatrix}^{\mathrm{T}} \tag{6.6}$$

Equation (6.5) represents the controlled linearized equations of motion of a Generalized Sail based spacecraft around[1] a L_1-type equilibrium point, where δB is the control variable (from which the name β-control, as B is related to the lightness number β, see Eq. (4.3)).

Note that with a β-control the system is not fully controllable [64]. In fact, the component along z of the linearized equation of motion (6.3) is

$$(\hat{\boldsymbol{k}} \cdot \delta\boldsymbol{r})'' + (1 - g\,k_{22})\hat{\boldsymbol{k}} \cdot \delta\boldsymbol{r} = 0 \tag{6.7}$$

because k_{33} is given in Eq. (B.19). The motion in the direction along $\hat{\boldsymbol{k}}$ is, then, uncoupled from that in the plane orthogonal to $\hat{\boldsymbol{k}}$ and is not affected by the control δB. Consequently, the motion along z cannot be driven to converge toward the equilibrium point. However, the equilibrium point may still be stabilizable, if the motion along z turns out to be stable[2].

Using a Proportional-Derivative (PD) feedback control, in the form

$$\delta B = -\boldsymbol{h}_P \cdot \delta\boldsymbol{r} - \boldsymbol{h}_D \cdot \delta\boldsymbol{r}' \tag{6.8}$$

Eq. (6.5) provides the closed loop system equations

$$\left[\boldsymbol{\xi}'\right]_{\mathcal{T}_P} = \begin{bmatrix} \mathbb{O}_{3\times3} & \mathbb{I}_{3\times3} \\ g\,\mathbb{K}_c^{\mathrm{T}} & \mathbb{E}_c \end{bmatrix} [\boldsymbol{\xi}]_{\mathcal{T}_P} \tag{6.9}$$

with

$$\mathbb{K}_c \triangleq \mathbb{K} + \mathbb{K}_P + \mathbb{H}_P\mathbb{U}^{\mathrm{T}} \quad , \quad \mathbb{E}_c \triangleq g\,\mathbb{U}\mathbb{H}_D^{\mathrm{T}} - 2\,\mathbb{E} \tag{6.10}$$

where $\mathbb{H}_P$ and $\mathbb{H}_D$ are the components of the gain vectors $\boldsymbol{h}_P$ and $\boldsymbol{h}_D$ in the pulsating frame, viz,

$$\mathbb{H}_P \triangleq [\boldsymbol{h}_P]_{\mathcal{T}_P} = \begin{bmatrix} h_{P_x} \\ h_{P_y} \\ h_{P_z} \end{bmatrix} \quad , \quad \mathbb{H}_D \triangleq [\boldsymbol{h}_D]_{\mathcal{T}_P} = \begin{bmatrix} h_{D_x} \\ h_{D_y} \\ h_{D_z} \end{bmatrix} \tag{6.11}$$

To show that the L_1-points are stabilizable, an analysis of the closed loop system in the circular case is now provided, when $\mathbb{H}_P$ and $\mathbb{H}_D$ are chosen so that only the x-components of $\delta\boldsymbol{r}$ and $\delta\boldsymbol{r}'$ are fed back (that is, $h_{P_y} = h_{P_z} = h_{D_y} = h_{D_z} = 0$).

[1] With the appropriate definition of both the $\mathbb{K}$-matrix entries and $\boldsymbol{u}$, the equation (6.5) may be used also for other families of AEPs.

[2] Note that the stability analysis for Eq. (6.7) is addressed with the aim of the Floquet theory. In case the problem is circular (viz $g = 1$), Eq. (6.7) is stable (not asymptotically), since $k_{33} = k_{22} - 1 < 0$ for L_1-type points.

6.2.1 Circular Case

For the circular problem (namely, $e = 0$, $g = 1$, $\ell = l$, and $B = \beta$), Eq. (6.2) gives

$$\beta_0 = \frac{\mu\rho_{1_0}^{\eta}}{(1-\mu)}\left[1 - \frac{1}{(1-\rho_{1_0})^2}\right] + \rho_{1_0}^{\eta-2} - \frac{\rho_{1_0}^{\eta+1}}{1-\mu} \tag{6.12}$$

Feeding back only the x-components of $\delta\boldsymbol{r}$ and $\delta\boldsymbol{r'}$, Eq. (6.9) may be rewritten as

$$\left[\boldsymbol{\xi}'\right]_{\mathcal{T}} = \begin{bmatrix} \mathbb{O}_{3\times3} & \mathbb{I}_{3\times3} \\ \mathbb{K}_c^{\mathrm{T}} & \mathbb{E}_c \end{bmatrix} \left[\boldsymbol{\xi}\right]_{\mathcal{T}} \tag{6.13}$$

with

$$\mathbb{K}_c = \begin{bmatrix} \bar{k}_{11} & 0 & 0 \\ 0 & k_{22} & 0 \\ 0 & 0 & k_{33} \end{bmatrix} \quad , \quad \mathbb{E}_c = \begin{bmatrix} \bar{e}_{11} & 2 & 0 \\ -2 & 0 & 0 \\ 0 & 0 & 0 \end{bmatrix} \tag{6.14}$$

where

$$\bar{k}_{11} \triangleq k_{11} - \frac{1-\mu}{\rho_{1_0}^{\eta}} h_{P_x} \quad , \quad \bar{e}_{11} \triangleq -\frac{1-\mu}{\rho_{1_0}^{\eta}} h_{D_x} \tag{6.15}$$

The study of the stability is based on the calculation of eigenvalues of Eq. (6.13). If λ is the generic eigenvalue of the system, the characteristic equation of the matrix of the system can be shown to be in the form

$$(\lambda^4 + a_c\,\lambda^3 + b_c\,\lambda^2 + c_c\,\lambda + d_c\,\lambda)(\lambda^2 - k_{33}) = 0 \tag{6.16}$$

with

$$a_c = -\bar{e}_{11} \quad , \quad b_c = 4 - k_{22} - \bar{k}_{11} \quad , \quad c_c = \bar{e}_{11}k_{22} \quad , \quad d_c = \bar{k}_{11}k_{22} \tag{6.17}$$

Taking into account that $k_{33} = k_{22} - 1$ and $k_{22} < 0$, the two eigenvalues corresponding to the dynamics in the z direction are imaginary, then the motion along z is marginally stable.

The Routh-Hurwitz criterion [67] applied to the fourth order polynomial in Eq. (6.17) gives the following conditions for stability

$$4 - k_{22} - \bar{k}_{11} > 0 \ \cap\ \bar{k}_{11}k_{22} > 0 \ \cap\ \bar{e}_{11} < 0 \ \cap\ \bar{e}_{11}k_{22} > 0 \ \cap\ 4 - \bar{k}_{11} > 0 \tag{6.18}$$

which are always fulfilled if

$$\bar{k}_{11} > 0 \quad \text{and} \quad \bar{e}_{11} < 0 \tag{6.19}$$

since $k_{22} < 0$.

Combining Eq. (6.19) with Eqs. (6.15) and (B.21), the concluding stability conditions for L_1-type equilibrium points are

$$h_{P_x} > h_{\min} \quad \text{and} \quad h_{D_x} > 0 \tag{6.20}$$

where

$$h_{\min} \triangleq -\frac{\partial \beta_0}{\partial \rho_{1_0}} = \frac{\rho_{1_0}^{\eta}}{(1-\mu)} \left[\frac{2\mu}{(1-\rho_{1_0})^3} - \frac{(\eta-2)(1-\mu)}{\rho_{1_0}^3} - \frac{\eta\mu(\rho_{1_0}-2)}{(\rho_{1_0}-1)^2} + \eta + 1 \right] \tag{6.21}$$

A feedback control system, whose gains satisfy the conditions in Eq. (6.20), makes asymptotically stable the motion of a spacecraft equipped with a Generalized Sail around a L_1-type AEP in the (x, y)-plane, according to Ref. [64] when $\eta = 2$.

Equation (6.21) implies that the value $h_{\min}$ is a function of both the propulsion system (η) and the celestial bodies masses (μ) as well as of the position of the AEP. Figure 6.1 shows the isocontour lines of the function $h_{\min} = h_{\min}(\rho_{1_0}, \eta)$ for the Sun-(Earth+Moon) and the Sun-(Jupiter+moons) systems, where $\mu = \mu_{\oplus} = 3.0404 \times 10^{-6}$ and $\mu = \mu_{♃} = 9.5388 \times 10^{-4}$, respectively. In general, the value of $h_{\min}$ is a decreasing function of η. However, when the equilibrium point approaches the classical Lagrangian point L_1, $h_{\min}$ becomes insensitive to a variation of η.

Note that in case a simple Proportional control is used (viz, $h_{D_x} = 0$), the characteristic equation (6.16) can be factorized similarly to Eq. (3.29). In this case, the stability conditions reduce to

$$h_{P_x} > h_{\min} \tag{6.22}$$

and the motion of the Generalized Sail based spacecraft results marginally stable.

6.3 Solar Balloon

According to Biggs and McInnes [64] a promising option to stabilize L_1-type points in a circular Sun-planet system is by means of a Solar Balloon[3], which is potentially able to passively generate a β-control.

The Solar Balloon may be thought of as being constituted by a thin spherical shell with a reflective surface, and inflated through a suitable gas. Under the effect of the photons incoming from the Sun, a Solar Balloon essentially behaves like a spherical Solar Sail [69,70] and provides a purely radial thrust with respect to the Sun.

The passive β-control actuated by the Solar Balloon is a consequence of its inflation/deflation when it moves from its equilibrium position. Indeed, assume the balloon is placed at a given L_1-type point, as in Fig. 6.2. The balloon has a radius that corresponds to an exposed area providing the acceleration needed to

[3]The original idea of a Solar Balloon comes from the balloon satellite concept developed in the early '60s. The first satellite of this class was Echo 1, launched in 1960, with its main purpose of passive communications experiments, but also useful for estimating the perturbative effect of the solar radiation pressure [68].

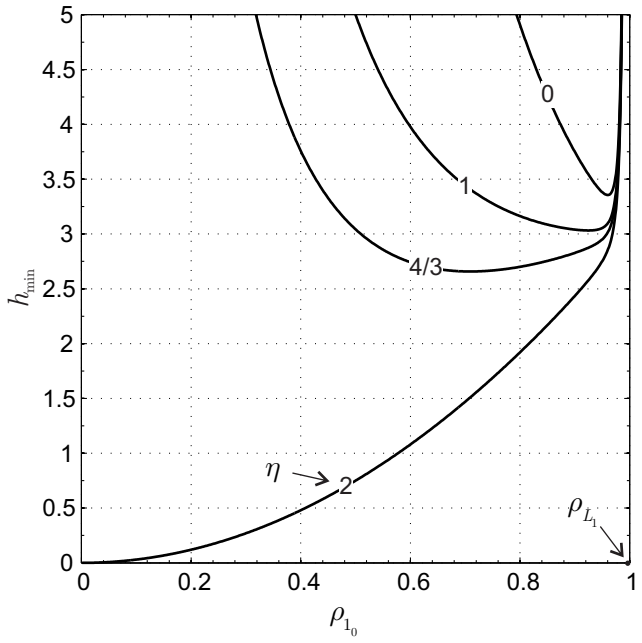

(a) Sun-(Earth+Moon) system.

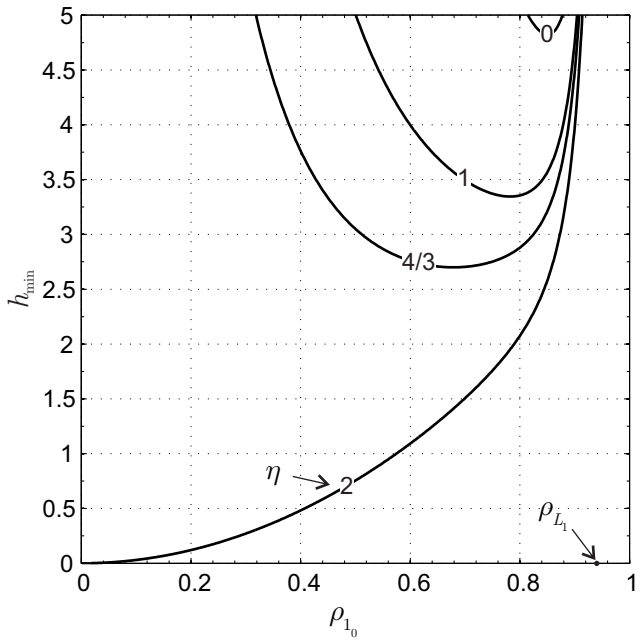

(b) Sun-(Jupiter+moons) system.

Figure 6.1: $h_{\min}$ in the circular problem as a function of ρ_{1_0} and η.

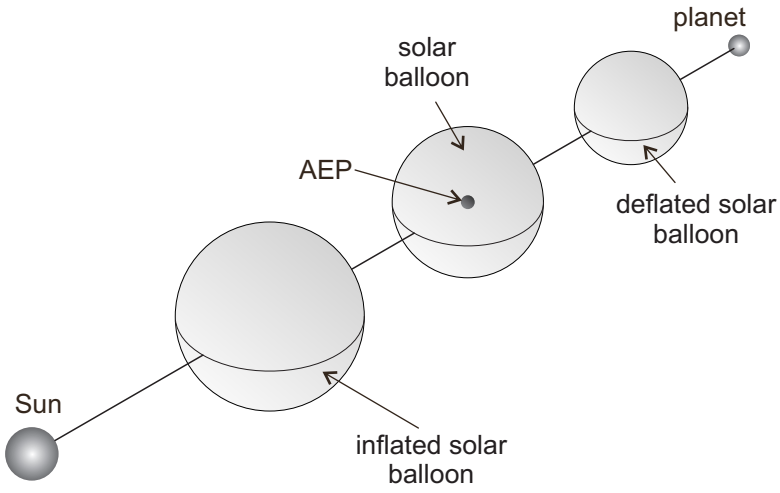

Figure 6.2: Inflation/Deflation mechanism of a Solar Balloon.

maintain the equilibrium point. If the balloon is perturbed toward the Sun and away from the AEP, it expands due to the increase in temperature. Consequently, the Sun-exposed area rises and the acceleration modulus increases along with the lightness number β, thus moving the balloon back toward the AEP. A similar but converse mechanism occurs when the balloon is perturbed away from the Sun. Therefore, the Solar Balloon intrinsically generates a passive β-control law [64], which only depends on the distance variation from the Sun.

Note that a balloon subjected to the inflation/deflation mechanism cannot be used to create AEPs in the ER3BP. In fact, for the elliptic problem, the Solar Balloon should maintain constant the radius (that is, constant β) to maintain an AEP, even though the distance AEP-Sun varies periodically, see Fig. 4.3.

Considering a circular problem, the first order variation of the balloon lightness number β at the equilibrium point $\boldsymbol{r}_0$ is

$$\delta\beta = \left.\frac{\partial\beta}{\partial\rho_1}\right|_{\boldsymbol{r}_0} \delta\rho_1 \tag{6.23}$$

where $\delta\rho_1$ is the corresponding variation of the Sun-spacecraft distance. Since $\delta\rho_1 = \nabla\rho_1|_{\boldsymbol{r}_0} \cdot \delta\boldsymbol{r}$, Eq. (6.1) yields

$$\delta\rho_1 = \delta\xi \tag{6.24}$$

where $\xi \triangleq \boldsymbol{r} \cdot \hat{\boldsymbol{\imath}}$ is the dimensionless distance along the x-axis.

Combining Eqs. (6.23) and (6.24), the lightness number variation $\delta\beta$ may be expressed as

$$\delta\beta = -h\,\delta\xi \qquad \text{where} \qquad h \triangleq -\left.\frac{\partial\beta}{\partial\rho_1}\right|_{\boldsymbol{r}_0} \tag{6.25}$$

Equation (6.25) states that the Solar Balloon behaves like a Proportional feedback controller of constant gain h.

As shown in Section 6.2.1, a Proportional β–control is potentially able to stabilize a spacecraft around an AEP. However, the linear stabilizability requires a minimum value of the gain to be used, so that the passively actuated Solar Balloon is able to make stable an AEP only if the gain h, which it provides, is bigger than a minimum value, see Eq. (6.22).

In the following, the gain h is related to the physical characteristics of the Solar Balloon by means of a simplified mathematical model, to show to what extent the Solar Balloon is actually able to maintain a L_1-type equilibrium point.

6.3.1 Solar Balloon Physical Model

A Solar Balloon, in terms of propulsive acceleration, may be thought of as being equivalent to a spherical Solar Sail with radius R. Let β_0, see Eq. (6.12) with $\eta = 2$, be the reference value of the lightness number when the balloon has to maintain an AEP placed at a distance ρ_{1_0} from the Sun, and let R_0 be the corresponding value of balloon's radius providing the needed exposed area. At the distance ρ_{1_0} the equilibrium temperature is T_0 and the internal pressure is p_0.

Since the Solar Sail lightness number is proportional to the exposed area of the reflective surface [19], for a spherical balloon β will be proportional to R^2. Accordingly, the first order variation of β as function of R is

$$\delta\beta = 2\,\beta_0\,\frac{\delta R}{R_0} \tag{6.26}$$

where δR is the radius variation due to an infinitesimal displacement from the equilibrium point.

The ratio $\delta R/R_0$ in Eq. (6.26) can be conveniently related to the physical and technological properties of the Solar Balloon through suitable simplifying hypotheses. To this end, the Solar Balloon is modeled as a thin spherical shell under internal pressure, due to a perfect gas. It is assumed that its inflation or deflation takes place by means of nearly steady-state transformations, and that both the external skin and the internal gas have the same uniform temperature.

The variation δR of the balloon's radius comes from the superposition effect of the internal pressure variation $\delta p \triangleq p - p_0$ and the skin's dilatation caused by its temperature variation $\delta T \triangleq T - T_0$, see Fig. 6.3(a).

The percentage variation $\delta R_p/R_0$, associated to an infinitesimal pressure increase δp, may be written as [71]

$$\frac{\delta R_p}{R_0} = \left(\frac{1-\nu_{\mathrm{P}}}{E}\right)\,\frac{R_0\,\delta p}{2\,t} \tag{6.27}$$

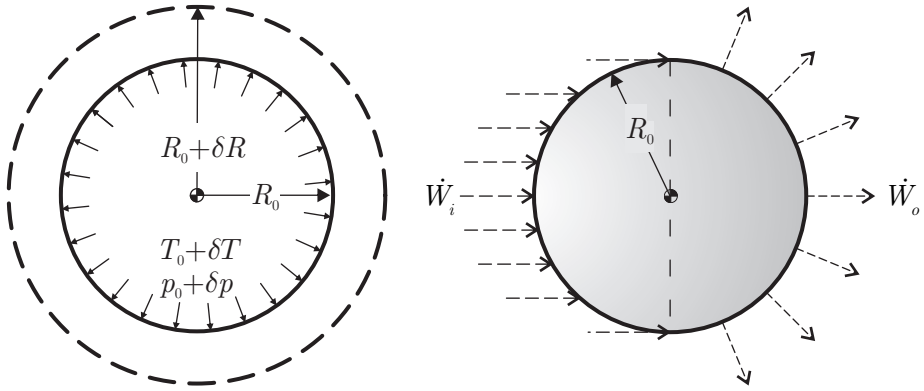

(a) Radius variation. (b) Power flux balance.

Figure 6.3: Solar Balloon simplified model.

where ν_{P} is the Poisson modulus, E is the Young modulus, and $t \ll R_0$ is the skin's thickness. On the other side, the percentage variation $\delta R_T/R_0$, due to a thermal expansion of the skin, is given by [72]

$$\frac{\delta R_T}{R_0} = \tau\, \delta T \tag{6.28}$$

where τ is the linear expansion coefficient of the skin.

The total radius variation is expressed as the superposition of the two previous effects [72], that is

$$\frac{\delta R}{R_0} = \frac{\delta R_p}{R_0} + \frac{\delta R_T}{R_0} \equiv k_0\, \frac{\delta p}{p_0} + \tau\, T_0\, \frac{\delta T}{T_0} \tag{6.29}$$

where

$$k_0 \triangleq \frac{1-\nu_{\mathrm{P}}}{E}\, \sigma_0 \tag{6.30}$$

and

$$\sigma_0 \triangleq \frac{p_0\, R_0}{2\, t} \tag{6.31}$$

is the skin's tensile stress calculated at the equilibrium point.

The percentage pressure variation $\delta p/p_0$, in Eq. (6.29), may be related to the percentage radius variation $\delta R/R_0$ and to the percentage temperature variation $\delta T/T_0$, under the assumption that the inner gas behaves like a perfect gas. Indeed, using the perfect gas law, it can be verified that an expansion of the pressure to the first order in T and R gives

$$\frac{\delta p}{p_0} = \frac{\delta T}{T_0} - 3\, \frac{\delta R}{R_0} \tag{6.32}$$

Substituting Eq. (6.32) into (6.33) yields

$$\frac{\delta R}{R_0} = \frac{k_0 + \tau\, T_0}{1 + 3\, k_0}\, \frac{\delta T}{T_0} \tag{6.33}$$

In its turn, the ratio $\delta T/T_0$ may be related to the distance ρ_1 by taking into account the Solar Balloon's thermal balance [19, 69]. In fact, δT depends on the variation of the power flux through the skin's surface. More precisely, assume that the illuminated hemisphere receives a solar power flux W_i and that the opposite half-sphere radiates a power flux W_o, see Fig. 6.3(b). Paralleling the procedure described by McInnes [19] for a flat solar sail, it is found that

$$W_i = \frac{\alpha\, W_\oplus\, (l_\oplus/l)^2\, A}{16\, \rho_1^2} \qquad , \qquad W_o = \frac{A}{2}\, \epsilon\, \widetilde{\sigma}\, T^4 \tag{6.34}$$

where α is the coefficient of absorptivity[4], ϵ is the coefficient of emissivity, $A = 4\pi R^2$ is the Solar Balloon's surface area, $W_\oplus = 1366\,\mathrm{W/m^2}$ is the solar constant, $l_\oplus \triangleq 1\,\mathrm{AU}$, and $\widetilde{\sigma} = 5.670373 \times 10^{-8}\,\mathrm{W/m^2/K^4}$ is the Stefan-Boltzmann constant.

The equilibrium temperature T at a distance ρ_1 from the Sun is obtained through Eqs. (6.34) from the balance between the incoming flux W_i and the outgoing flux W_o. The result is

$$\frac{T}{T_0} = \sqrt{\frac{\rho_{1_0}}{\rho_1}} \qquad , \qquad T_0 = \frac{T_P}{\sqrt{\rho_{1_0}}} \tag{6.35}$$

where

$$T_P \triangleq \sqrt[4]{\frac{\alpha\, W_\oplus\, (l_\oplus/l)^2}{8\, \epsilon\, \widetilde{\sigma}}} \tag{6.36}$$

Note that T_P depends on the reference distance l and on the optical properties of the reflective surface through the ratio α/ϵ.

An expansion to the first order in ρ_1 of Eq. (6.35) implies that

$$\frac{\delta T}{T_0} = -\frac{1}{2}\, \frac{\delta \rho_1}{\rho_{1_0}} \tag{6.37}$$

Substituting Eq. (6.37) into (6.33) and recalling Eq. (6.24) yields

$$\frac{\delta R}{R_0} = -\frac{1}{2}\, \frac{k_0 + \tau\, T_0}{1 + 3\, k_0}\, \frac{\delta \xi}{\rho_{1_0}} \tag{6.38}$$

Finally, combining Eq. (6.38) with (6.26) and comparing the result with Eq. (6.25), the following expression of h is obtained

$$h = \left(\frac{k_0 + \tau\, T_P/\sqrt{\rho_{1_0}}}{1 + 3\, k_0} \right) \frac{\beta_0}{\rho_{1_0}} \tag{6.39}$$

[4] To be not confused with the cone angle in Chapter 5.

Note how h implicitly depends on the optical parameters of the reflecting film (α and ϵ) through T_P, see Eq. (6.36). The skin's mechanical properties also appear in Eq. (6.39) both explicitly, by means of τ, and implicitly, through k_0, see Eq. (6.30).

Note also that the previous expression of the gain h totally neglects secondary aspects such as any variation of skin's mechanical and thermal characteristics due to a temperature variation [73], any influence of a nonuniform temperature distribution [74], and any variation of optical properties of the reflecting surface due to either stretching or degradation phenomena [75, 76].

6.3.2 Solar Balloon Effectiveness

The expression of the gain h, see Eq. (6.39), is the starting point to investigate whether or not a Solar Balloon is actually able to stabilize a L_1-type AEP in the circular problem.

In Section 6.2.1, the linear stability analysis shows that the condition for dynamical stability with a Proportional feedback of the x-component of position is $h > h_{\min}$, see Eq. (6.22), where, using Eq. (6.21) with $\eta = 2$,

$$h_{\min} = \frac{\rho_{1_0}^2 \left(-3\rho_{1_0}^3 + 9\rho_{1_0}^2 + 2\mu\,\rho_{1_0}^2 - 9\rho_{1_0} - 6\mu\,\rho_{1_0} + 6\mu + 3\right)}{(1-\mu)\,(1-\rho_{1_0})^3} \tag{6.40}$$

Note that assuming a Sun-(Earth+Moon) system and considering a L_1-type AEP with $\rho_{1_0} = 0.9804$, Eqs (6.12) and (6.40) provide $\beta_0 = 0.05$ and $h_{\min} = 3.677$, results that are in accordance to those obtained by Biggs and McInnes [64]. Note also that using the properties of Kapton®, see Table 6.1, and assuming a pre-tensioning value of $\sigma_0 = 70\,\text{kPa}$ [77], the gain provided by a Solar Balloon is $h = 2.9676 \times 10^{-4}$, from Eq.(6.39). Such gain is much less than the minimum value necessary to obtain a stable collinear point.

Property	Value	Ref.
E	$2.5\,\text{GPa}$	[78]
ν_{P}	0.34	[78]
τ	$2 \times 10^{-5}\,\text{K}^{-1}$	[77]
α	0.09	[77]
ϵ	0.04	[77]

Table 6.1: Mechanical, thermal, and optical properties of Kapton®.

From Eq. (6.39) it is clear that h is a monotonic increasing function of k_0, τ and T_P (equivalently, of α/ϵ, see Eq. (6.36)). This implies that, for a given

value of ρ_{1_0} (therefore, for a given value of β_0), the gain h is between two extreme values, h_a and h_b, given by

$$h_a \triangleq \lim_{k_0 \to 0} h = \frac{\tau\, T_P\, \beta_0}{\sqrt{\rho_{1_0}^3}} \qquad , \qquad h_b \triangleq \lim_{k_0 \to \infty} h = \frac{\beta_0}{3\,\rho_{1_0}} \tag{6.41}$$

Figure 6.4 shows, in the plane $(\rho_{1_0},\, h)$, the value of $h_{\min}$ obtained from Eq. (6.40) along with the values of h_a and h_b, given by Eqs. (6.41), for the Sun-(Earth+Moon) and the Sun-(Jupiter+moons) systems when Kapton® is used (see Table 6.1 for Kapton® properties). The value of h is not shown because k_0 is on the order of 10^{-5} when a pre-tensioning value of $\sigma_0 = 70\,\text{kPa}$ is used. Consequently, the value of h is well approximated by the value of h_a.

Note that for a fixed system of attractors (that is, for a given value of μ) and a given skin's material, it is possible to detect a plane region containing all possible pairs $(\rho_{1_0},\, h)$ corresponding to a stable L_1-type equilibrium point. In this region, a given pre-tensioning value sets univocally the pairs $(\rho_{1_0},\, h)$.

This region is bounded, along the axis of abscissae, by the maximum admissible distance from the Sun, referred to as $\rho^\star_{1_0}$, corresponding to the distance at which[5] $h_{\min} = h_b$. Equating Eq. (6.40) and the second relation of Eq. (6.41), $\rho^\star_{1_0}$ is the only real root less than one of the following sixth order equation in the variable ρ_{1_0}

$$10\rho_{1_0}^6 - (30+7\mu)\,\rho_{1_0}^5 + (30+21\mu)\,\rho_{1_0}^4 - (11+19\mu)\,\rho_{1_0}^3 + (1-\mu)\,\left(3\,\rho_{1_0}^2 - 3\,\rho_{1_0} + 1\right) = 0 \tag{6.42}$$

Because in the Solar System the dimensionless mass μ does not exceed 10^{-5} (in case of Jupiter), a reasonable approximation for $\rho^\star_{1_0}$ is obtained substituting $\mu = 0$ into Eq. (6.42). The result is $\rho^\star_{1_0} \simeq \sqrt[3]{0.1} \simeq 0.4642$, which is in good agreement with what is shown in Fig. 6.4. Note that, when $\rho_{1_0} = \rho^\star_{1_0}$, the required lightness number is $\beta_0 \simeq 0.9$ for both Earth and Jupiter, which corresponds to a very high characteristic acceleration, that is, a maximum propulsive acceleration (at a distance of 1 AU from the Sun) of about $5.3\,\text{mm/s}^2$.

Unfortunately, the current technology permits to reach values of h that are less than h_b. Therefore, according to Figure 6.4, the AEPs theoretically maintained by means of Solar Balloons cannot be farther than $0.2\,l - 0.3\,l$ from the Sun. However, even within this scenario, Eq. (6.12) states that the required lightness number is $\beta_0 > 0.95$, a performance value which is well beyond the current or near-term Solar Sail capabilities.

As an alternative, the only reasonable option is related to the development

[5] Clearly $k_0 \to +\infty$ in Eq. (6.41) is a purely theoretical condition because it would correspond to an infinitely large value of σ_0, see Eq. (6.30).

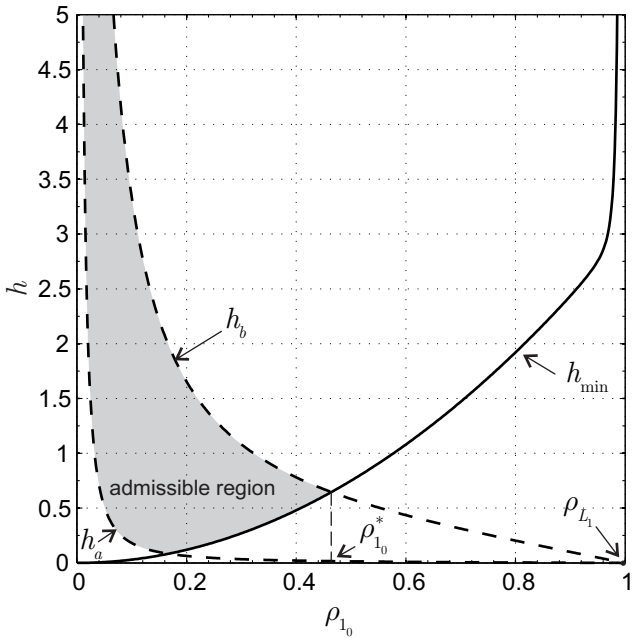

(a) Sun-(Earth+Moon) system.

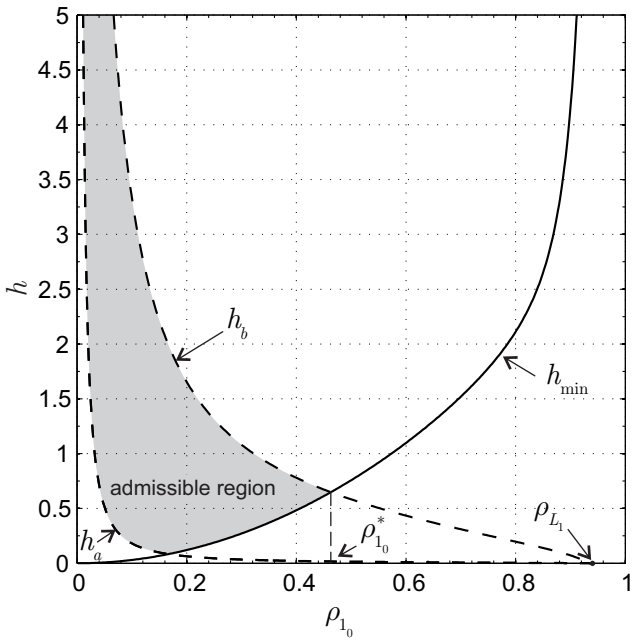

(b) Sun-(Jupiter+moons) system.

Figure 6.4: Solar Balloon's gain as a function of ρ_{1_0} using Kapton®.

of materials with an increased value of linear expansion coefficient[6] τ. Indeed, recalling Eq. (6.41), an increase of τ would correspond to an upward shift of the boundary line[7] associated to h_a. Assume that suitably high values of τ can be reached such that, unlike the situation depicted in Fig. 6.4, the curve $h_a = h_a(\rho_{1_0})$ is now above the curve $h_b = h_b(\rho_{1_0})$. In this case the maximum admissible distance from the Sun would be obtained by intersecting h_a with $h_{\min}$.

The value of τ, required to place the intersection at a given ρ_{1_0}, can be found by enforcing the condition $h_a = h_{\min}$. Equating (6.40) and the first of (6.41), yields

$$\tau = \frac{\sqrt{\rho_{1_0}^7}}{(1-\rho_{1_0})\,T_P}\,\frac{3\,\rho_{1_0}^3 - (9+2\,\mu)\,\rho_{1_0}^2 + (9+6\,\mu)\,\rho_{1_0} - 3 - 6\,\mu}{\rho_{1_0}^5 - (2+\mu)\,\rho_{1_0}^4 + (1+2\,\mu)\,\rho_{1_0}^3 - (1-\mu)\,\rho_{1_0}^2 + (2-2\,\mu)\,\rho_{1_0} - 1 + \mu} \tag{6.43}$$

which is valid as long as $\rho_{1_0} \in (0,\, \rho_{L_1})$. Note that when $\rho_{1_0} \simeq 0.15$ the previous relationship provides $\tau \simeq 10^{-5}$, in accordance to the results shown in Fig. 6.4, both for the Sun-(Earth+Moon) and Sun-(Jupiter+Moons) systems.

Return now to the previous example in the Sun-(Earth+Moon) system. Equation (6.43) states that a passive control of a Solar Balloon placed at a distance $\rho_{1_0} = 0.9804$ [64] requires a material with a coefficient of linear expansion on the order of $0.25\,\mathrm{K}^{-1}$, a value well beyond the current technological limits.

In conclusion, the passive control mechanism provided by a Solar Balloon is able to stabilize only L_1-type points close to the Sun, which means points that are not accessible with the current or near-term Solar Sails. Of course, the possibility of an active control of either the inflation/deflation mechanism of the balloon or the employment of varying reflectance surface of the balloon could improve the stability of these spacecraft configurations.

6.4 Electrochromic Material Panels on a Solar Sail

Electrochromic materials are a particular class of materials able to experience and maintain reversible changes of their optical properties (in particular, of their reflectivity) upon the application of a suitable electric voltage [79].

Similar materials have been already employed in space missions, notably Liquid Crystals for the attitude control of the Japanese Solar Sail demonstrator Ikaros [80, 81], see Fig. 6.5. An interesting implementation of a β-control, which makes use of *Electrochromic Material Panel*s (EMPs), has been recently suggested by Lücking et al. [82, 83], even if in Refs. [82, 83] the mission application

[6] Increasing the value of α/ϵ could be another option, however this would correspond to an increase of T_P and of T_0, which could be well beyond the maximum operating temperature of the spacecraft.

[7] Remember that h_b is not a function of the skin's properties, therefore cannot be varied.

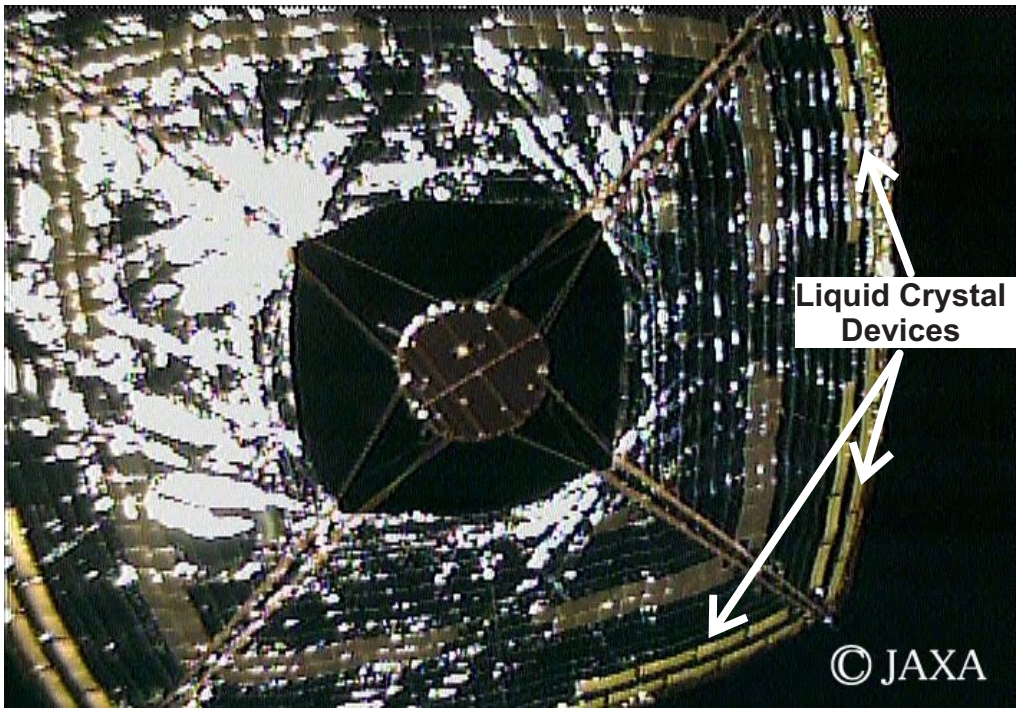

Figure 6.5: Ikaros captured by its deployable cameras in June 2010 (Courtesy of JAXA).

is confined to micro-scale spacecraft (in an Earth-centered orbit) with a simple bang-bang control logic.

In the following, the capabilities of the emerging EMPs technology for the active stabilization of L_1-type AEPs are explored, when a square Solar Sail with a fixed attitude is used. The problem is addressed within an elliptic restricted framework, which is a more realistic model with respect to the classical circular case [64]. The main spacecraft parameters, including the sail side and the total spacecraft mass, are defined, by means of a simplified mathematical model, as a function of the main mission requirements in terms of maximum allowed sail lightness number variation and AEP position. In addition, a simple control logic that encompasses the negative effects of both an (unavoidable) uncertainty and a saturation in the actual sail lightness number is discussed.

6.4.1 Spacecraft Model

Consider a spacecraft of total mass m, whose primary propulsion system is constituted by a square Solar Sail of total area[8] A, with a slightly conical shape and

[8]Note that, in principle, the useful sail area A is strictly related to the sail conical angle. However, in this simplified analysis a slight conical angle is assumed, such that the area of each reflecting surface is substantially coincident with the area projected in the sunward direction.

whose apex is directed sunward, see Fig. 6.6. With such a sail configuration a radial thrust with respect to the Sun is maintained in a pure passive way [84].

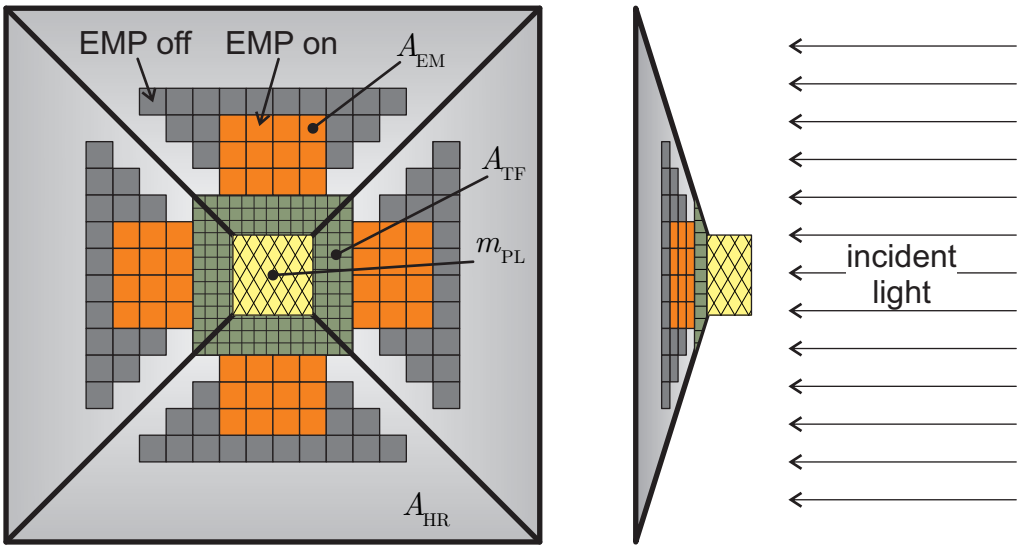

(a) Front View. (b) Side View.

Figure 6.6: Spacecraft schematic model.

The sail surface can be thought of as being constituted by three parts. The first part, of area A_{HR}, is covered with high reflectivity material. Its main purpose is that of exploiting the solar radiation pressure to produce a propulsive thrust. A second part is covered by electrochromic material, which is used to modulate the thrust (within a moderate range) without varying the sail attitude [82]. In analogy to the design solution adopted for Ikaros [80, 81], this second part is constituted by N panels. Each panel, with area A_{EM}, varies its reflectivity as it changes its state. The latter can assume two values, either power-off (low reflectivity), or power-on state (high reflectivity), depending on the amount of voltage applied to the panel [80]. Finally, the third part, of area A_{TF}, is covered with flexible thin-film solar cells [85], whose purpose is to guarantee the electric power required by the payload and the EMPs.

Each reflective surface contributes to the total spacecraft acceleration by converting, with different efficiencies, the solar radiation pressure into propulsive thrust. According to the literature [19, 86], the reflectivity of a generic sail element can be modeled by introducing an efficiency factor η_{surf}. The latter is a dimensionless coefficient that can assume a value ranging from 0.5 (perfectly absorbing surface) to 1 (perfectly reflecting surface). In particular, the efficiency value of an EMP can be set equal to either η_{ON} or $\eta_{\mathrm{OFF}} < \eta_{\mathrm{ON}}$ according to

whether the corresponding EMP is switched on or off.

The total sail's area is written as

$$A \triangleq A_{\mathrm{HR}} + A_{\mathrm{TF}} + N\, A_{\mathrm{EM}} \tag{6.44}$$

while the total spacecraft mass can be expressed by adapting the simplified model described in Ref. [37]:

$$m = \sigma_{\mathrm{HR}}\, A_{\mathrm{HR}} + \sigma_{\mathrm{TF}}\, A_{\mathrm{TF}} + N\, \sigma_{\mathrm{EM}}\, A_{\mathrm{EM}} + m_{\mathrm{PL}} \tag{6.45}$$

where m_{PL} is the payload mass (including the spacecraft bus), and σ_{surf} is the areal density, defined as the mass per area unit for each element. Note that σ_{HR} includes the supporting structures as, for example, booms and deployment module [37].

Assume that, at a given time instant, a number $N_{\mathrm{ON}} \leq N$ of EMPs are switched on. To guarantee that the EMPs provide a pure thrust contribution (without introducing any additional torque on the spacecraft) it is necessary that a symmetry exists in the distribution of switched on/off panels with respect to the spacecraft's center of mass[9].

Let $n \geq 2$ the minimum number of EMPs that simultaneously can vary their state. For example, if $n = 4$, these four panels are placed at the vertexes of a rectangle whose center coincides with the spacecraft's center of mass. Observe that both N and N_{ON} must be integer multiples of n. In particular, the number $N_{\mathrm{ON}} \in \mathbb{N}$ represents the only thrust control variable, since the spacecraft thrust variation is obtained by simply setting on (or off) a suitable number of EMPs.

Because, by assumption, the mean Solar Sail plane is orthogonal to the direction of incoming solar rays, the total propulsive acceleration provided by the Solar Sail can be written as the sum of the acceleration provided by each surface constituting the sail

$$\boldsymbol{a}_{\mathrm{P}} = \left(\sum_{\mathrm{surf}} A_{\mathrm{surf}} \eta_{\mathrm{surf}} \right) \frac{\sigma^{\star}}{m} \frac{G m_1}{\ell^2 \rho_1^2} \hat{\boldsymbol{\rho}}_1 \tag{6.46}$$

where $\sigma^{\star} \simeq 1.53\,\mathrm{g/m^2}$ is the critical sail loading parameter [19]. With the aid of Eqs. (4.1) and (6.45) the total sail lightness number may be written as

$$\beta \triangleq \frac{\sigma^{\star}\, [\eta_{\mathrm{HR}}\, A_{\mathrm{HR}} + \eta_{\mathrm{TF}}\, A_{\mathrm{TF}} + N_{\mathrm{ON}}\, \eta_{\mathrm{ON}}\, A_{\mathrm{EM}} + (N - N_{\mathrm{ON}})\, \eta_{\mathrm{OFF}}\, A_{\mathrm{EM}}]}{(\sigma_{\mathrm{HR}}\, A_{\mathrm{HR}} + \sigma_{\mathrm{TF}}\, A_{\mathrm{TF}} + N\, \sigma_{\mathrm{EM}}\, A_{\mathrm{EM}} + m_{\mathrm{PL}})} \tag{6.47}$$

The presence of EMPs is useful to vary the sail lightness number between a minimum value β_{min}, when all of EMPs are switched off ($N_{\mathrm{ON}} = 0$) and a

[9] In this simplified analysis, a failure of part of the EMPs (with a consequent loss of symmetry) is not considered. However, in that case the symmetry could be restored by simply excluding both the broken EMPs and their symmetric counterpart. This solution, of course, reduces the maximum available variation of the sail lightness number.

maximum value $\beta_{\max}$, when $N_{\rm ON} = N$. From Eq. (6.47), $\beta_{\min}$ and $\beta_{\max}$ are given by

$$\beta_{\min} = \frac{\sigma^\star \left[\eta_{\rm HR}\, A_{\rm HR} + \eta_{\rm TF}\, A_{\rm TF} + N\, \eta_{\rm OFF}\, A_{\rm EM}\right]}{\left(\sigma_{\rm HR}\, A_{\rm HR} + \sigma_{\rm TF}\, A_{\rm TF} + N\, \sigma_{\rm EM}\, A_{\rm EM} + m_{\rm PL}\right)} \tag{6.48}$$

$$\beta_{\max} = \frac{\sigma^\star \left[\eta_{\rm HR}\, A_{\rm HR} + \eta_{\rm TF}\, A_{\rm TF} + N\, \eta_{\rm ON}\, A_{\rm EM}\right]}{\left(\sigma_{\rm HR}\, A_{\rm HR} + \sigma_{\rm TF}\, A_{\rm TF} + N\, \sigma_{\rm EM}\, A_{\rm EM} + m_{\rm PL}\right)} \tag{6.49}$$

Note that β can only take a finite number (equal to $N/n+1$) of values within its variation interval. Therefore β is actually chosen from a "thrust setting table", similar to what happens for solar electric propulsion systems [87].

The mean sail lightness number $\overline{\beta} \triangleq (\beta_{\min} + \beta_{\max})/2$ is obtained when one half of EMPs are switched on, that is, when $N_{\rm ON} = N/2$. The quantity $\overline{\beta}$ can be thought of as a reference sail lightness number and its value is chosen to be as close as possible to β_0 given by Eq. (6.2), when $\eta = 2$.

The maximum allowable variation with respect to the mean value will be referred to as $\Delta\beta \triangleq (\beta_{\max} - \beta_{\min})/2$ and represents an index of the maximum spacecraft capability of varying its thrust performance during the mission. Combining Eqs. (6.48) and (6.49) it is found that

$$\overline{\beta} = \frac{\sigma^\star \left[2\, \eta_{\rm HR}\, A_{\rm HR} + 2\, \eta_{\rm TF}\, A_{\rm TF} + N\, (\eta_{\rm ON} + \eta_{\rm OFF})\; A_{\rm EM}\right]}{2\left(\sigma_{\rm HR}\, A_{\rm HR} + \sigma_{\rm TF}\, A_{\rm TF} + N\, \sigma_{\rm EM}\, A_{\rm EM} + m_{\rm PL}\right)} \tag{6.50}$$

$$\Delta\beta = \frac{\sigma^\star\, N\, (\eta_{\rm ON} - \eta_{\rm OFF})\; A_{\rm EM}}{2\left(\sigma_{\rm HR}\, A_{\rm HR} + \sigma_{\rm TF}\, A_{\rm TF} + N\, \sigma_{\rm EM}\, A_{\rm EM} + m_{\rm PL}\right)} \tag{6.51}$$

The term $A_{\rm TF}$ in the previous equations will now be expressed as a function of $m_{\rm PL}$ and $A_{\rm EM}$. This is possible by observing that the surface covered with flexible thin-film solar cells must generate an electric power sufficient for supplying power to both the payload and the EMPs. More precisely, introduce a payload specific power $\alpha_{\rm PL}$, defined as the electric power per unit mass required by the payload, and a solar array efficiency $\epsilon_{\rm TF}$ [88], which coincides with the ratio between the solar arrays output electric power per area unit and the local solar irradiance.

The power generation system is designed in a conservative way under the following assumptions: 1) end life conditions (when the degradation effects are maximum), 2) maximum solar distance during the mission (when the solar irradiance is minimum), and 3) maximum required power condition. Assuming that the degradation effects are all included in a single coefficient $\epsilon_{\rm TF}$ and that the maximum Sun-spacecraft distance is equal to one Astronomical Unit, a simplified electric power balance between the power generated by the solar cells and that absorbed by EMPs and payload provides the required value of $A_{\rm TF}$:

$$A_{\rm TF} = \frac{\phi_{\rm EM}\, N\, A_{\rm EM} + \alpha_{\rm PL}\, m_{\rm PL}}{\epsilon_{\rm TF}\, W_\oplus} \tag{6.52}$$

where $W_\oplus \triangleq 1366\,\mathrm{W/m^2}$ is the solar constant, and ϕ_{EM} is the electric power per area unit required by the EMPs.

Spacecraft Sizing

When Eq. (6.52) is substituted into Eq. (6.47) and the spacecraft physical characteristics are fixed, β is shown to depend linearly on the control variable $N_{\mathrm{ON}} \in \{0,\, n,\, 2n, ...,\, N\}$, that is

$$\beta = \beta_{\min} + k_\beta\, N_{\mathrm{ON}} \tag{6.53}$$

where

$$k_\beta \triangleq \frac{\sigma^\star\, A_{\mathrm{EM}}\, (\eta_{\mathrm{ON}} - \eta_{\mathrm{OFF}})}{\sigma_{\mathrm{HR}}\, A_{\mathrm{HR}} + \sigma_{\mathrm{TF}}\, A_{\mathrm{TF}} + N\, \sigma_{\mathrm{EM}}\, A_{\mathrm{EM}} + m_{\mathrm{PL}}} \tag{6.54}$$

The sail lightness number also depends, in a more involved way, on the four design parameters N, m_{PL}, A_{HR}, and A_{EM}. However, by means of Eqs. (6.50) and (6.51), N and A_{HR} are more conveniently expressed as a function of two other mission parameters, that is, β_0 and $\Delta\beta$. Indeed, assuming that $\overline{\beta} = \beta_0$, the result is

$$N = \mathrm{round}\left[\left(\frac{m_{\mathrm{PL}}/A_{\mathrm{EM}}}{n\,\sigma^\star}\right)\frac{\Delta\beta}{c_1\,\beta_0 + c_2\,\Delta\beta + c_3}\right] n \tag{6.55}$$

$$A_{\mathrm{HR}} = \frac{m_{\mathrm{PL}}}{\sigma^\star}\left(\frac{c_4}{c_1\,\beta_0 + c_2\,\Delta\beta + c_3} - c_6\right) - c_5\, N\, A_{\mathrm{EM}} \tag{6.56}$$

where the round function is introduced in Eq. (6.55) because N can only take integer values. The coefficient c_i (with $i = 1, 2, \ldots, 6$) are dimensionless, independent of the design parameters but dependent on the physical characteristic of

the system, defined as

$$c_1 \triangleq \frac{\epsilon_{\mathrm{TF}}\, W_{\oplus}\, (\eta_{\mathrm{ON}} - \eta_{\mathrm{OFF}})\, (\sigma_{\mathrm{HR}}/\sigma^{\star})}{2\,(\sigma_{\mathrm{HR}}\,\eta_{\mathrm{TF}}\,\alpha_{\mathrm{PL}} - \sigma_{\mathrm{TF}}\,\alpha_{\mathrm{PL}}\,\eta_{\mathrm{HR}} - \epsilon_{\mathrm{TF}}\,W_{\oplus}\,\eta_{\mathrm{HR}})} \tag{6.57a}$$

$$c_2 \triangleq \frac{2\,\sigma_{\mathrm{EM}}\,\epsilon_{\mathrm{TF}}\,W_{\oplus}\,\eta_{\mathrm{HR}} + 2\,\phi_{\mathrm{EM}}(\sigma_{\mathrm{TF}}\,\eta_{\mathrm{HR}} - \sigma_{\mathrm{HR}}\,\eta_{\mathrm{TF}}) - \sigma_{\mathrm{HR}}\,\epsilon_{\mathrm{TF}}\,W_{\oplus}(\eta_{\mathrm{ON}} + \eta_{\mathrm{OFF}})}{2\,\sigma^{\star}\,(\sigma_{\mathrm{HR}}\,\eta_{\mathrm{TF}}\,\alpha_{\mathrm{PL}} - \sigma_{\mathrm{TF}}\,\alpha_{\mathrm{PL}}\,\eta_{\mathrm{HR}} - \epsilon_{\mathrm{TF}}\,W_{\oplus}\,\eta_{\mathrm{HR}})} \tag{6.57b}$$

$$c_3 \triangleq \frac{-\eta_{\mathrm{HR}}\,\epsilon_{\mathrm{TF}}\,W_{\oplus}\,(\eta_{\mathrm{ON}} - \eta_{\mathrm{OFF}})}{2\,(\sigma_{\mathrm{HR}}\,\eta_{\mathrm{TF}}\,\alpha_{\mathrm{PL}} - \sigma_{\mathrm{TF}}\,\alpha_{\mathrm{PL}}\,\eta_{\mathrm{HR}} - \epsilon_{\mathrm{TF}}\,W_{\oplus}\,\eta_{\mathrm{HR}})} \tag{6.57c}$$

$$c_4 \triangleq \frac{\sigma^{\star}\,(\eta_{\mathrm{ON}} - \eta_{\mathrm{OFF}})}{2\,\sigma_{\mathrm{HR}}} \tag{6.57d}$$

$$c_5 \triangleq \frac{\sigma_{\mathrm{EM}}}{\sigma_{\mathrm{HR}}} + \frac{\sigma_{\mathrm{TF}}\,\phi_{\mathrm{EM}}}{\sigma_{\mathrm{HR}}\,\epsilon_{\mathrm{TF}}\,W_{\oplus}} \tag{6.57e}$$

$$c_6 \triangleq \frac{\sigma^{\star}}{\sigma_{\mathrm{HR}}}\left(\frac{\sigma_{\mathrm{TF}}\,\alpha_{\mathrm{PL}}}{\epsilon_{\mathrm{TF}}\,W_{\oplus}} + 1\right) \tag{6.57f}$$

Note that, as a consequence of the discretization process induced by the finite area of each EMP, in Eq. (6.55), the attainable value of $\overline{\beta}$ is actually different from the required value β_0.

For a given mission scenario (that is, β_0 and $\Delta\beta$ are given) and for a prescribed set of coefficients c_i, Eqs. (6.55) and (6.56) can be used to estimate the required values of N and A_{HR} as a function of the payload mass m_{PL} and the area A_{EM} of a single panel. It is worth noting that in the limiting case in which $\Delta\beta = 0$ (when the sail is unable to perform a β-control) Eq. (6.55) states that, as expected, $N = 0$. Moreover, combining Eq. (6.56) with (6.57a), (6.57c), and (6.57d), it can be shown that when $\Delta\beta = 0$, A_{HR} is independent of the optical characteristics of the electrochromic material.

To summarize, for a given set of data β_0, $\Delta\beta$, m_{PL}, A_{EM}, and n, the value of N is calculated from Eq. (6.55), A_{HR} from Eq. (6.56), A_{TF} from Eq. (6.52), A from Eq. (6.44), m from Eq. (6.45) and, finally, $\beta_{\min}$ and $\beta_{\max}$ from Eqs. (6.48)-(6.49).

6.4.2 Choice of the Control Logic

As stated in Section 6.2.1 for the circular problem, a PD control logic is able to guarantee an asymptotical stability of a L_1-type point in the (x, y) plane. Similarly, in the elliptical problem it can be shown that a PD feedback control law gives the same results. Assume, for example, the following β-control law for a Solar Sail

$$\delta\beta_{\mathrm{PD}} = -h_P\,(\delta\boldsymbol{r}\cdot\hat{\boldsymbol{\imath}}) - h_D\,(\delta\boldsymbol{r}'\cdot\hat{\boldsymbol{\imath}}) \tag{6.58}$$

where h_P, h_D are the Proportional and Derivative gains, respectively. An analysis by means of the Floquet theory of Eq. (6.9) provides the pairs (h_P, h_D) necessary to guarantee an asymptotical stability for a L_1-type point. For example for a L_1-type equilibrium at $r_0 = \|\boldsymbol{r}_0\| = 0.980$ in the Sun-(Earth+Moon) system, the PD gains are given in Fig. 6.7.

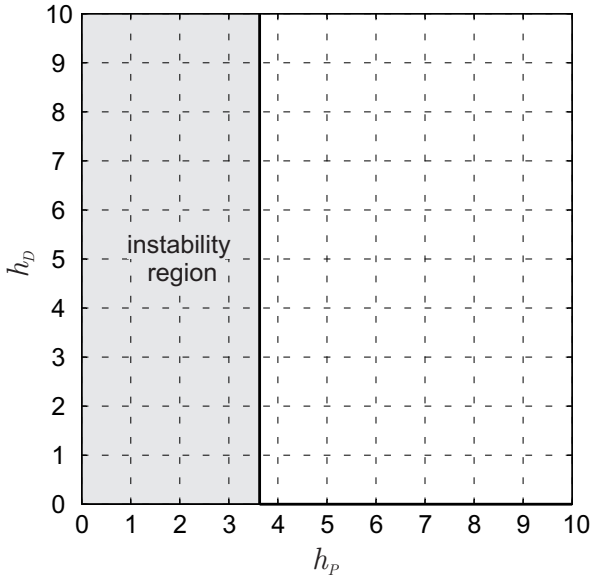

Figure 6.7: PD gains for a Solar Sail in the Sun-(Earth+Moon) when $r_0 = 0.980$.

A PD control logic, however, could produce unacceptable errors in the final spacecraft position when an uncertainty in the actual sail lightness number occurs. Indeed, if the actual value of the sail lightness number is (slightly) different from the nominal value β_0 given by Eq. (6.2) with $\eta = 2$, the spacecraft trajectory converges to an AEP different from the desired one.

To get over this problem, a classical Proportional-Integral-Derivative (PID) control law can be used. More precisely, an ideal[10] control law can be assumed in the form

$$\delta\beta_{\text{PID}} = -h_P\,(\delta\boldsymbol{r}\cdot\hat{\boldsymbol{\imath}}) - h_D\,(\delta\boldsymbol{r}'\cdot\hat{\boldsymbol{\imath}}) - h_I\int_0^{\nu}(\delta\boldsymbol{r}\cdot\hat{\boldsymbol{\imath}})\,\mathrm{d}\nu \tag{6.59}$$

where h_P, h_D and h_I are the Proportional, Derivative, and Integral gains, respectively. The introduction of the integral term modifies the stability region of Fig. 6.7. For example, Fig. 6.8 summarizes the new stability regions. Each isocontour line in the figure is drawn for a fixed value of h_I, and represents the

[10] The term "ideal" is used above to emphasize that the practical implementation of the control law requires some differences to be introduced with respect to Eq. (6.59), as will be discussed later.

lower-left boundary region of pairs (h_P, h_D) for which the L_1-type AEP is stable.

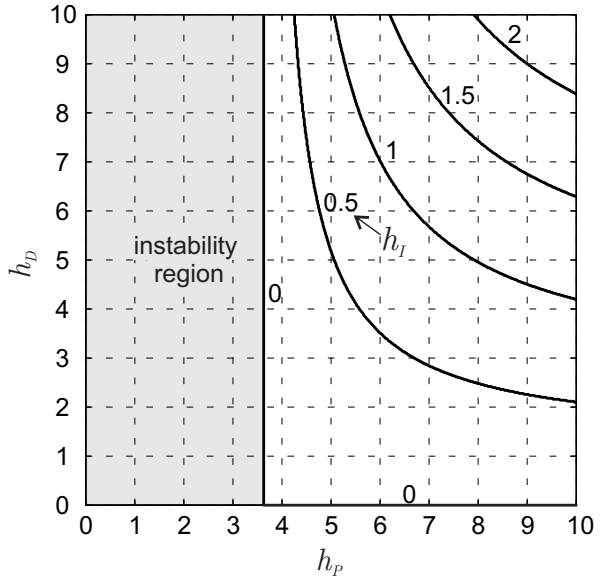

Figure 6.8: PID gains for a Solar Sail in the Sun-(Earth+Moon) when $r_0 = 0.980$.

To appreciate the usefulness of the PID control logic, consider a L_1-type AEP with $r_0 = 0.980$, and assume $h_P = h_D = 10$. Figure 6.9 compares the spacecraft trajectories with and without Integral control, when the reference value of the sail lightness number is $\overline{\beta} = 1.01\,\beta_0$, with $\beta_0 = 0.051497$, and the injection position error is $|\delta \boldsymbol{r}| \approx 14.3 \times 10^{-5}$ (corresponding to approximately 20000 km). Note that the Integral control with $h_I = 1$ eliminates any asymptotical error.

The actual implementation of a PID logic for a β-control will now be discussed assuming that the sail lightness number may be varied, within a specified range, by means of EMPs, whose reflectivity changes depending on the amount of voltage applied to the panels.

Control Law Implementation

From the previous discussion, the sail lightness number can be effectively controlled, through a PID control logic, in the interval $\beta \in [\beta_{\min}, \beta_{\max}]$ according to Eq. (6.53). However, unlike the ideal steering law described by Eq. (6.59), two other aspects must be taken into account. In fact, the propulsive acceleration is both subjected to a discretization effect due to the presence of EMPs of finite size, and to a possible control saturation.

In particular, the quantization error introduced by the discretization process is $n\,k_\beta$, which corresponds to the minimum sail lightness number variation ob-

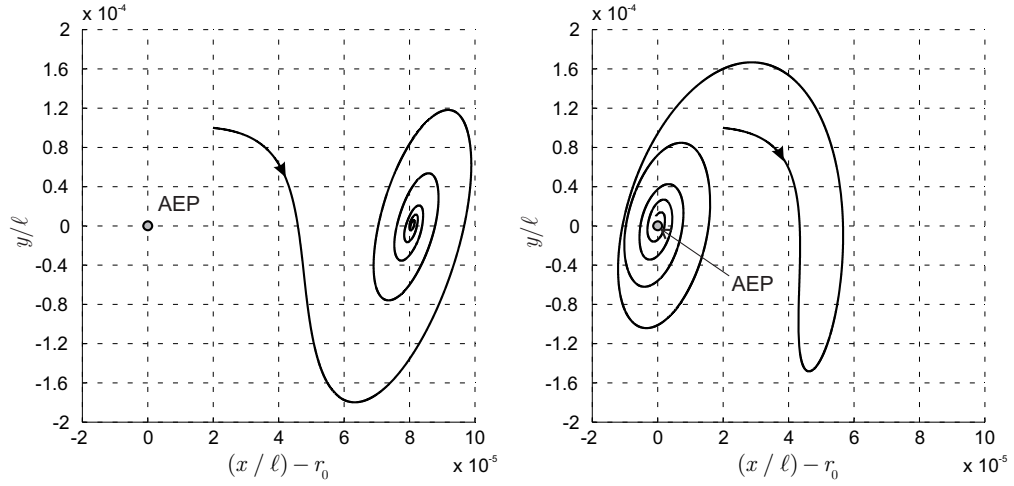

(a) $\overline{\beta} = 1.01\,\beta_0$ and $h_I = 0$.

(b) $\overline{\beta} = 1.01\,\beta_0$ and $h_I = 1$.

Figure 6.9: Effect of the Integral control on the asymptotical error when $r_0 = 0.980$ in the Sun-(Earth+Moon).

tained when a single group of n EMPs changes its state. Such a discretization effect can be reduced by using EMPs of smaller area. On the other hand, a saturation occurs (and a windup behavior takes place) when the EMPs are unable to provide the sail lightness number variation $\delta\beta_{\text{PID}}$ commanded by the control logic described in Eq. (6.59). This phenomenon can have a fundamental influence on the behavior of the controlled system and, in some cases, it can cause instability. To effectively counteract the saturation effect, an anti-windup compensator is therefore introduced. Its main purpose is to reduce the integral action when the β-control saturates [89]. A block diagram for the β-control logic, including the anti-windup compensator (with a gain $h_{\text{AW}} \geq 0$), is shown in Fig. 6.10.

Recall that $\overline{\beta}$ is the reference sail lightness number provided by the Solar Sail. If the current spacecraft position (x/ℓ) does not coincide with the desired AEP, an error $\delta\boldsymbol{r} \cdot \hat{\boldsymbol{\imath}} \neq 0$ occurs. This error signal is processed by the PID controller block whose output is first translated into a (discrete) lightness number variation, and then compared to the minimum/maximum obtainable values. When a saturation takes place, the integral of the difference between the lightness value required by the control logic and the saturated value is integrated by the anti-windup block and the result is eventually added to the PID output. Note that the contribution from the anti-windup block is different from zero only when the control system is saturated, that is, when $\delta\beta = \pm k_\beta\, N/2$.

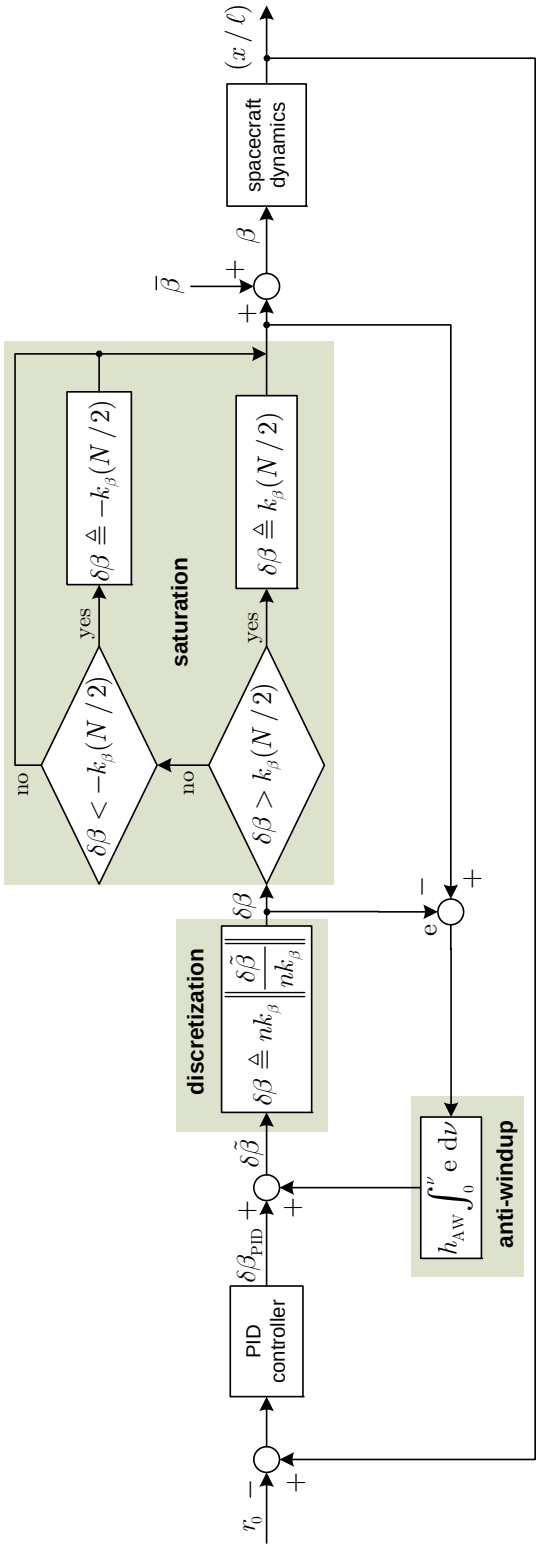

Figure 6.10: Block diagram for the β-control logic.

6.4.3 Numerical Simulations

The previous mathematical model will now be used to illustrate the preliminary design of a Solar Sail based spacecraft, whose mission requirement is to maintain an L_1-type AEP in the neighborhood of a classical L_1 Lagrange point in the Sun-(Earth+Moon) system. Within this mission scenario the AEP position is, at any time instant, along the Sun-Earth line at a dimensionless distance $r_0 = 0.980$ from the center of mass of the system (equivalently, at a distance $\rho_{1_0} = 0.980 + \mu_\oplus$ from the Sun).

Some spacecraft characteristics, as for example a payload mass of 91 kg, have been extrapolated from the Heliostorm Warning Mission (a variant of the Geostorm Warning Mission [9], see Fig. 1.4(a)), using tables and plots taken from Ref. [90]. For the high-reflectivity element, a film with an aluminium-coated

Parameter	Value	Units	Ref.
m_{PL}	91	kg	[90]
A_{EM}	1	m^2	
n	8		
α_{PL}	8	W/kg	[90]
σ_{HR}	5.68	$\mathrm{g/m}^2$	[90]
σ_{EM}	80	$\mathrm{g/m}^2$	[91]
σ_{TF}	80	$\mathrm{g/m}^2$	[88]
η_{ON}	0.908		
η_{OFF}	0.5		[82]
η_{HR}	0.908		[92]
η_{TF}	0.5		
ϕ_{EM}	20	$\mathrm{W/m}^2$	
ϵ_{TF}	0.1		[88]

Table 6.2: Physical reference data for spacecraft with EMPs.

front side and a chromium-coated back side is assumed [92]. As far as the electrochromic part is concerned, $A_{\mathrm{EM}} = 1\,\mathrm{m}^2$ and $n = 8$ are assumed. Moreover, according to Ref. [82], and in the absence of additional data, η_{ON} is taken equal to η_{HR} and $\eta_{\mathrm{OFF}} = 0.5$, which corresponds to a complete absorption of the incoming photons. Finally, thin-film solar cells with Cu(In,Ga)Se2 as an absorber layer and Kapton® as a substrate are assumed [85,88]. A conservatively small value of

$\epsilon_{\mathrm{TF}} = 10\%$ is used to model the effects of a performance degradation with time. The physical data necessary to calculate the coefficients c_i in Eqs. (6.57a)–(6.57f) are summarized in Table 6.2, along with the corresponding bibliographical information from which those data have been derived. The values of the six coefficients are given in Table 6.3.

Coefficient	c_1	c_2	c_3	c_4	c_5	c_6
Value	-0.8303	-56.5111	0.2031	0.0550	16.1467	0.2706

Table 6.3: Value of coefficients c_i in Eq. (6.57) with data from Table (6.2).

The maximum allowable variation $\Delta\beta$ must be chosen depending on the estimated perturbations magnitude that will affect the spacecraft dynamics at the desired AEP. The spacecraft characteristic parameters, obtained with the methodology outlined above, have been summarized in Table 6.4 for $\Delta\beta/\beta_0 = \{1\%, 2\%, 3\%, 4\%\}$.

Parameter	$\Delta\beta/\beta_0$				Eq.
	1%	2%	3%	4%	#
N	232	600	1256	2792	(6.55)
$A_{\mathrm{HR}}\,[\mathrm{m}^2]$	5064	6219.3	8381.6	13236.7	(6.56)
$A_{\mathrm{TF}}\,[\mathrm{m}^2]$	39.3	93.2	189.2	414.1	(6.52)
$A\,[\mathrm{m}^2]$	5335.3	6912.5	9826.8	16442.8	(6.44)
$m\,[\mathrm{kg}]$	141.5	181.8	254.2	422.7	(6.45)
$\beta_{\min} \times 10^2$	5.119646	5.044816	5.015082	4.930915	(6.48)
$\beta_{\max} \times 10^2$	5.222018	5.250858	5.323488	5.343261	(6.49)
$\overline{\beta} \times 10^2$	5.170832	5.147837	5.169285	5.137088	
$k_\beta \times 10^6$	4.412614	3.434037	2.45546	1.476883	(6.53)
$n\,k_\beta \times 10^5$	3.530091	2.747230	1.964368	1.181506	

Table 6.4: Spacecraft parameters for $r_0 = 0.980$ and $\beta_0 = 0.051497$.

The table shows a rapid growth of N with an increase of $\Delta\beta/\beta_0$, which implies an increase of the sail side (roughly proportional to $\sqrt{A}$) and of the total mass of the system.

For illustrative purposes assume that $\Delta\beta/\beta_0 = 1\%$ and use the spacecraft parameters from Table 6.4. To discuss the β-control effectiveness, two cases have

been considered, with and without ($h_{\mathrm{AW}} = 0$) the effect of the anti-windup logic. In both cases the PID parameters are chosen to be $h_P = 10$, $h_D = 10$, and $h_I = 1$ (this corresponds to a stable configuration, see Fig. 6.8). An initial spacecraft position error of 20000 km and a velocity error of 150 m/s has been simulated.

Firstly, the anti-windup gain h_{AW} is set equal to zero, and the simulation results are shown in Figs. 6.11(a) and 6.12(a). Due to a rapid saturation of the control system, the number of switched on EMPs is either $N_{\mathrm{ON}} = 0$ or $N_{\mathrm{ON}} = 232$, and the control system is unable to drive the spacecraft toward the desired L_1-type AEP.

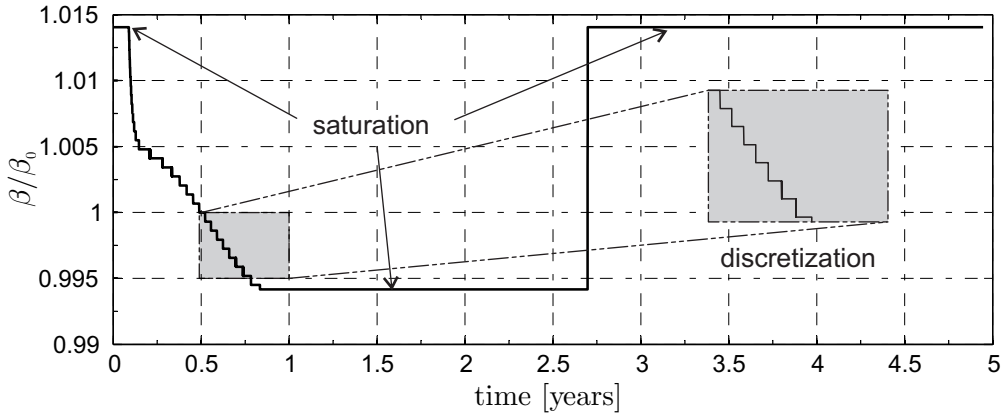

(a) Without anti-windup filter ($h_{\mathrm{AW}} = 0$).

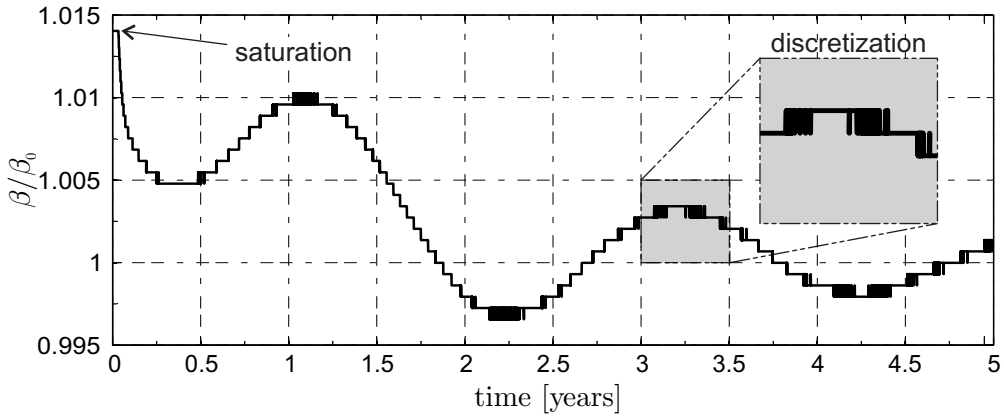

(b) With anti-windup filter ($h_{\mathrm{AW}} = 10$).

Figure 6.11: Time variation of the sail lightness number for a spacecraft moving around the L_1-type AEP at $r_0 = 0.980$.

However, when the anti-windup controller is engaged, with $h_{\mathrm{AW}} = 10$, the sail lightness number is quickly steered within its linear variation range, see Fig. 6.11(b), and the spacecraft dynamics remains bounded around the desired

L_1-type AEP, see Fig. 6.12(b).

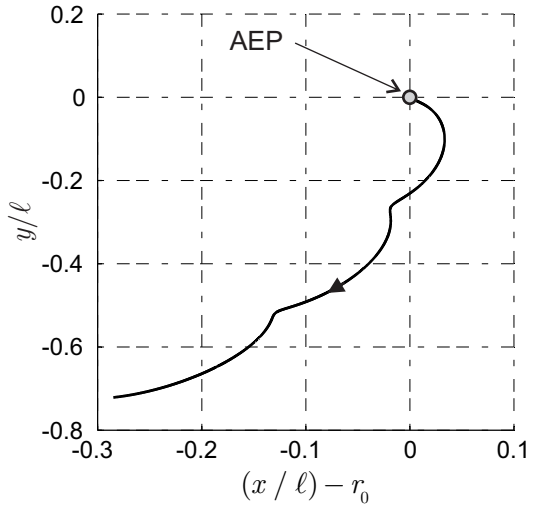

(a) Without anti-windup filter ($h_{\mathrm{AW}} = 0$).

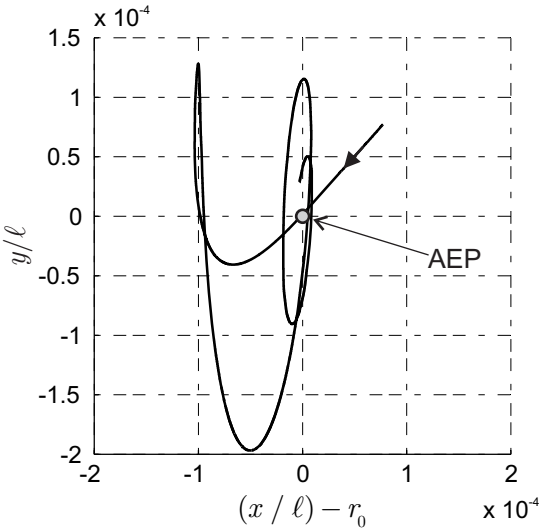

(b) With anti-windup filter ($h_{\mathrm{AW}} = 10$).

Figure 6.12: Spacecraft trajectory in the synodic pulsating frame around the L_1-type AEP at $r_0 = 0.980$.

In conclusion, EMPs can be effectively used as a simple control means to stabilize a Solar Sail based spacecraft with a fixed radial attitude about an L_1-type AEP. Indeed, the EMPs can be used to vary the sail lightness number by changing their state from on to off (and vice versa) in such a way to provide a propulsive acceleration variation and stabilize the spacecraft. Simulations show the importance of the Integral control to remove the negative effects of an uncertainty in

the actual value of the lightness number and the usefulness of an anti-windup system to counteract the integral action when the control system saturates.

Part II

Displaced Frozen Orbits

Chapter 7

Displaced Frozen Orbits

In this chapter the dynamics of a spacecraft equipped with a Solar Sail in orbit around an oblate planet is studied, taking into account the perturbing effects of the Sun with the aim of finding new *frozen orbits*. The problem is handled by means of an analytical method based on the averaging technique of the Hamiltonian describing the motion of the spacecraft. With such a method new families of frozen orbits (called *displaced*) are found. Moreover, such new frozen orbits are inspected using numerical integration of the equations of motion for a spacecraft in orbit around Mercury and a comparison with the analytical results is provided.

7.1 Introduction

The Keplerian model of gravitation confines the motion of a spacecraft with respect to a primary body to a conical trajectory, whose plane is fixed with respect to an inertial reference system. The true motion of a spacecraft is however different from the Keplerian model due to the presence of perturbing forces, such as the forces induced by the inhomogeneity of the gravitational field of the primary, atmospheric resistance or the force exerted by other bodies [93].

The effects of these perturbing forces are usually undesirable, especially for observation and communication spacecraft that require accurate pointing capabilities. For this reason such spacecraft have sophisticated systems on board dedicated to orbit control and, generally, their orbits are chosen to minimize the effects of perturbations hence, reducing the required action of the control system. Indeed, with a suitable choice of the initial orbital elements of the osculating orbit it is possible either to obtain an orbital motion that in average maintains some of the initial orbital elements (*frozen orbits*), or to use the perturbations to generate a desirable time-variation of an orbital element. Typical examples of such orbits are the Molniya orbits or the Sun-synchronous orbits, obtained when

only the effects of the primary body oblateness are considered [94].

More general mathematical models including other perturbation effects also show the existence of frozen orbits. For example, Coffey et al. [95], using a Lie transformation to average the Hamiltonian of the system, studied frozen orbits within a model including zonal perturbations up to J_9. Within the same gravitational model, Lara et al. [96] used a numerical continuation method of periodic orbits to find new families of frozen orbits. The effects of the J_2 coefficient along with of the effects of a third body on a circular orbit was studied by Scheeres et al. [97], using both analytical averaging and numerical technique. Later, Paskowitz and Scheeres [98] also added the effect of J_3. Abad et al. [99] have shown that families of frozen orbits exist for a lunar orbiter when the gravitational force of the Earth and the zonal perturbations of the Moon up to J_7 are considered. Using a power series expansion of the Hamiltonian function, Lara et al. [100] have studied frozen orbits around Mercury in the ER3BP, including both the J_2 and J_3 terms in the gravity field of Mercury. Delsate et al. [101] have developed an analytical theory based on an averaging method of the Hamiltonian to find frozen orbits around an oblate primary body, including the effect of a third body on elliptic orbit around the primary.

All the above mentioned works concern the effect of *natural* perturbations on spacecraft motion. Typically, the obtained results show the existence of a number of frozen orbits or families of frozen orbits whose orbital elements are constrained to belong to a small set of values. To extend such a set of values, a possible solution is the use of a continuous-thrust propulsion system that guarantees an increased set of achievable values of orbital elements by frozen or Sun-synchronous orbits, see Refs. [102–104].

Through an extension of the work of Delsate et al. [101], the frozen orbits achievable by a Solar Sail based spacecraft are studied in the following. It is shown how assuming that the propulsive acceleration provided by the Solar Sail is radial permits the application of the averaging technique developed by Tremaine et al. in Ref. [105] to the Hamiltonian of the system. Then, the achievable frozen orbits are analyzed, and an application to the orbits around Mercury is presented to show the effects of the propulsive acceleration provided by a Solar Sail. Finally, numerical simulations of orbits around Mercury are presented, and some limitations of the theoretical results are discussed.

7.2 Mathematical Preliminaries

Consider a spacecraft orbiting around a planet with a gravitational parameter μ_P. Assume that the spacecraft motion is perturbed by the gravitational effects of the Sun and by the propulsive acceleration provided by a Solar Sail, whose

thrust is assumed to be always radial with respect to the Sun. Note that this can be achieved by a suitable design of the sail shape (e.g., conical shaped Solar Sails or Solar Balloons) and is representative of a situation in which the sail attitude can be maintained in a passive manner [64, 84, 106].

The motion of the spacecraft is therefore described by the following Hamiltonian:

$$\mathcal{H} = \frac{1}{2}v^2 - \phi_P - \phi_S - \phi_T \tag{7.1}$$

where v is the velocity of the spacecraft with respect to the planet and ϕ_P, ϕ_S and ϕ_T represent the potentials induced by the planet, the Sun and the Solar Sail, respectively.

The gravitational potential of the planet is usually written [93, 107] by means of an expansion in terms of associated Legendre functions $P_{lm}(\sin\delta)$ and spherical harmonic coefficients C_{lm} and S_{lm} as

$$\phi_P = \frac{\mu_P}{r}\sum_{l=0}^{\infty}\sum_{m=0}^{l}\left(\frac{R_P}{r}\right)^l P_{lm}(\sin\delta)\left[C_{lm}\cos(m\lambda) + S_{lm}\sin(m\lambda)\right] \tag{7.2}$$

where R_P is the mean equatorial radius of the planet, (r, λ, δ) the spherical planetocentric coordinates of the spacecraft. The remaining potentials ϕ_S and ϕ_T can be written as [107]

$$\phi_S = \mu_S\left(\frac{1}{\|\boldsymbol{r}-\boldsymbol{r}_S\|} - \frac{\boldsymbol{r}\cdot\boldsymbol{r}_S}{\|\boldsymbol{r}_S\|^3}\right) \quad \text{and} \quad \phi_T = -\beta\frac{\mu_S}{\|\boldsymbol{r}-\boldsymbol{r}_S\|} \tag{7.3}$$

where $\boldsymbol{r}$ and $\boldsymbol{r}_S$ are the position vectors of spacecraft and Sun with respect to the planet, $\mu_S = 132\,712\,442\,099\,\mathrm{km}^3/\mathrm{s}^2$ [56] is the gravitational parameter of the Sun and β is the sail lightness number, assumed less than one in the following.

According to Tremaine et al. [105], Farago et al. [108], and Delsate et al. [101], the three potentials in Eqs. (7.2)–(7.3) can be conveniently approximated to obtain a simplified form of the Hamiltonian, which is well suited for mathematical analysis. The planet's gravitational potential ϕ_P can be expanded up to the $C_{20} \equiv -J_2$ term to obtain the approximated gravitational potential

$$\phi_P = \frac{\mu_P}{r} - J_2\frac{\mu_P R_P^2}{2r^5}\left[3(\boldsymbol{r}\cdot\hat{\boldsymbol{n}}_P)^2 - r^2\right] \tag{7.4}$$

which corresponds to the potential of an ellipsoidal planet, where $\hat{\boldsymbol{n}}_P$ is the unit vector parallel to the spin axis of the planet in the direction of the north pole of rotation. For the Sun and the Solar Sail potentials, a Laplace expansion of $\|\boldsymbol{r}-\boldsymbol{r}_S\|^{-1}$ is used. Because $r \ll r_S$, the expansion can be limited to the second order Legendre polynomial [107]. With such an assumption the sum of Sun and Solar Sail potentials is approximated by

$$\phi_S + \phi_T = (1-\beta)\mu_S\left\{\frac{1}{r_S} + \frac{1}{2r_S^5}\left[3(\boldsymbol{r}\cdot\boldsymbol{r}_S)^2 - (r\,r_S)^2\right]\right\} - \beta\frac{\mu_S}{r_S^3}(\boldsymbol{r}\cdot\boldsymbol{r}_S) \tag{7.5}$$

Now, using the averaging relations introduced by Kozai [109] and Boué et al. [110], firstly average the simplified Hamiltonian over the apparent motion of the Sun around the planet (with eccentricity e_P and semi-major axis a_P), using the mean anomaly as the independent variable. Then, average over the spacecraft orbit, assuming constant[1] eccentricity e and semi-major axis a over an orbit.

By virtue of the orbit averaging, the semi-major axis a results a constant of motion, hence it is possible to obtain an averaged dimensionless Hamiltonian $\mathcal{H}_{\text{av}}$, dividing the averaged Hamiltonian by $\mu_P J_2 R_P^2/a^3$, which is a constant. The result is

$$\begin{aligned}\mathcal{H}_{\text{av}} = &-\frac{a^2}{2J_2R_P^2}+\frac{1-3(\hat{\boldsymbol{n}}\cdot\hat{\boldsymbol{n}}_P)^2}{4(1-e^2)^{3/2}}+\\ &\frac{3}{8}\gamma(1-\beta)\left[5(\boldsymbol{e}\cdot\hat{\boldsymbol{n}}_S)^2-\left(1-e^2\right)(\hat{\boldsymbol{n}}\cdot\hat{\boldsymbol{n}}_S)^2-2e^2+3-\frac{8a_P^2(1-e_P^2)^{3/2}}{3a^2}\right]\end{aligned} \tag{7.6}$$

In Eq. (7.6) the eccentricity vector $\boldsymbol{e}$, the unit vector $\hat{\boldsymbol{n}}$ of the angular momentum of the osculating orbit, and the unit vector $\hat{\boldsymbol{n}}_S$ of the angular momentum of the Sun's orbit have been introduced together with the coefficient γ, defined as [101],

$$\gamma \triangleq \frac{\mu_S a^5}{\mu_P a_P^3\left(1-e_P^2\right)^{3/2}J_2R_P^2} \tag{7.7}$$

As a is constant, and under the assumption that $\hat{\boldsymbol{n}}_S = \hat{\boldsymbol{n}}_P$, a dimensionless set of canonical Delaunay variables $\{\omega, \Omega, G, H\}$ is now introduced. The variables ω and Ω are the argument of the pericenter and longitude of the ascending node of the osculating orbit of the spacecraft, respectively, while $G = \sqrt{1-e^2}$ and $H = G\cos i$ are the corresponding conjugate momenta, where i is the inclination of the orbit with respect to $\hat{\boldsymbol{n}}_P$.

With such variables, the Hamiltonian in Eq. (7.6) can be written as

$$\begin{aligned}\overline{\mathcal{H}} = \frac{1}{4G^3}-\frac{3H^2}{4G^5}+\frac{3}{8}\gamma(1-\beta)\left[5\left(1-G^2\right)\left(1-\frac{H^2}{G^2}\right)\sin^2\omega-H^2+2G^2\right]+\\ \frac{3}{8}(1-\beta)\gamma\left[1-\frac{8a_P^2(1-e_P^2)^{3/2}}{3a^2}\right]-\frac{a^2}{2J_2R_P^2}\end{aligned} \tag{7.8}$$

which is the same Hamiltonian found by Delsate et al. [101] when $\beta = 0$ (no propulsive acceleration) apart from some constant terms. Note that such constant

[1]Note that the averaging technique requires that the non Keplerian forces acting on the spacecraft must be regarded as perturbations, that is, several orders of magnitude less than the pure Keplerian gravitational force. This assumption will later be seen to have important consequences and will be better explained when the obtained orbits are considered using numerical simulation techniques.

terms are not necessary to describe the motion of the spacecraft because the equations of motion (derived from the Hamiltonian in Eq. (7.8)) are invariant under the addition of a constant term to the Hamiltonian. That means that when $\beta = 0$ all of the results in Ref. [101] are recovered. It is explicitly stated that $0 \leq H \leq G \leq 1$, and all of the unnecessary constants will be set to zero in the following.

7.3 Frozen Orbits

In general, due to perturbations, the altitude of a spacecraft relative to its given subsatellite point on the planet varies with time, from one orbit to the next. If the orbit is chosen such that the altitude depends (apart from short period oscillations) only on the latitude of the subsatellite point, without any variation with time, that orbit is said to be *frozen* [93]. Such an orbit has constant a, e, i and ω on average or, equivalently, constant a, ω, G and H.

Since the equations of variation of the orbital parameters of the spacecraft are derived from the Hamiltonian in Eq. (7.8), a and H are constants of motion (because $\overline{\mathcal{H}}$ is independent of mean anomaly and longitude of ascending node). The remaining parameters ω and G are constants of motion if they are equilibrium points of $\overline{\mathcal{H}}$. Therefore, the possible frozen orbits are found as the equilibrium points of the Hamiltonian in Eq. (7.8) and their stability depends on the sign definiteness of the Hessian matrix associated to the Hamiltonian, according to the Lagrange-Dirichlet Criterion [111].

Taking the first derivatives of $\overline{\mathcal{H}}$ with respect to ω and G, the frozen orbits are found as the solutions of the equations:

$$\left(1 - G^2\right)\left(1 - \frac{H^2}{G^2}\right)\sin\omega\cos\omega = 0 \tag{7.9a}$$

$$\frac{1}{G^4}\left(\frac{5H^2}{G^2} - 1\right) + \gamma(1-\beta)\left[5\sin^2\omega\left(\frac{H^2}{G^3} - G\right) + 2G\right] = 0 \tag{7.9b}$$

and the stability of the orbits depends on the second derivatives of $\overline{\mathcal{H}}$:

$$\frac{\partial^2\overline{\mathcal{H}}}{\partial\omega^2} = \frac{15}{4}\gamma(1-\beta)\left(1-G^2\right)\left(1-\frac{H^2}{G^2}\right)\left(\cos^2\omega - \sin^2\omega\right) \tag{7.10a}$$

$$\frac{\partial^2\overline{\mathcal{H}}}{\partial G^2} = \frac{3}{2G^5}\left(2 - \frac{15H^2}{G^2}\right) + \frac{3}{4}\gamma(1-\beta)\left[2 - 5\sin^2\omega\left(1 + \frac{3H^2}{G^4}\right)\right] \tag{7.10b}$$

$$\frac{\partial^2\overline{\mathcal{H}}}{\partial\omega\partial G} = \frac{15}{2}\gamma(1-\beta)\sin\omega\cos\omega\left(\frac{H^2}{G^3} - G\right) \tag{7.10c}$$

Equation (7.9a) is the same found in Ref. [101] and its solutions are $G = 1$ (or $e = 0$), $\sin\omega\cos\omega = 0$ (or $\omega = 0,\ \pm\pi/2,\ \pi$) and $H = G$ (or $i = 0,\ \pi$).

In the following, the solutions of the remaining equation (7.9b) will be studied along with the stability properties for the cases $G = 1$ and $\sin\omega\cos\omega = 0$. The results of the analysis will be converted in terms of classical orbital parameters using Mercury as primary body and assuming the physical data of Table 7.1.

Parameter	Value	Units	Ref.
$\mu_S/\mu_{\mercury}$	6.0236×10^6		[56]
$R_{\mercury}$	2439.7	km	[112]
$J_{2_{\mercury}}$	6×10^{-5}		[113]
$e_{\mercury}$	0.20563593		[114]
$a_{\mercury}$	0.38709927	AU	[114]

Table 7.1: Physical data of Mercury.

7.3.1 Case $e = 0$: Circular Orbits

For $G = 1$, that is $e = 0$, the argument of pericenter ω is not defined so Eq. (7.9b) cannot be used to study the circular case. By means of the following canonical transformation

$$x = \sqrt{2(1-G)}\cos\omega \quad , \quad X = \sqrt{2(1-G)}\sin\omega \tag{7.11}$$

it is possible to eliminate the indetermination, so that the Hamiltonian in Eq. (7.8) becomes

$$\overline{\mathcal{H}}_{\mathrm{c}} = \frac{\left(1-\dfrac{x^2+X^2}{2}\right)^2 - 3H^2}{4\left(1-\dfrac{x^2+X^2}{2}\right)^5} + \frac{3}{8}\gamma(1-\beta)\left\{\frac{5X^2}{2}\left(2-\frac{x^2+X^2}{2}\right)\times \left[1-\frac{H^2}{\left(1-\dfrac{x^2+X^2}{2}\right)^2}\right] - H^2 + 2\left(1-\frac{x^2+X^2}{2}\right)^2\right\} \tag{7.12}$$

The Hamiltonian in Eq. (7.12) has an equilibrium point for $x = 0$ and $X = 0$ (that is, for $G = 1$ or $e = 0$), independent of the value of H. Hence, circular orbits are always frozen for all inclinations. However, by means of the Lagrange-Dirichlet Criterion, it can be shown that they are stable only when

$$\cos^2 i < \frac{1-2\gamma(1-\beta)}{5} \quad \text{or} \quad \cos^2 i > \frac{1+3\gamma(1-\beta)}{5\left[1+\gamma(1-\beta)\right]} \tag{7.13}$$

Fig. 7.1 shows the stability regions in terms of orbital parameters obtained from Eq. (7.13) for different values of β when the primary body is Mercury. The gray regions in figure represents the pair altitude–inclination for which the orbit is stable when $\beta = 0$.

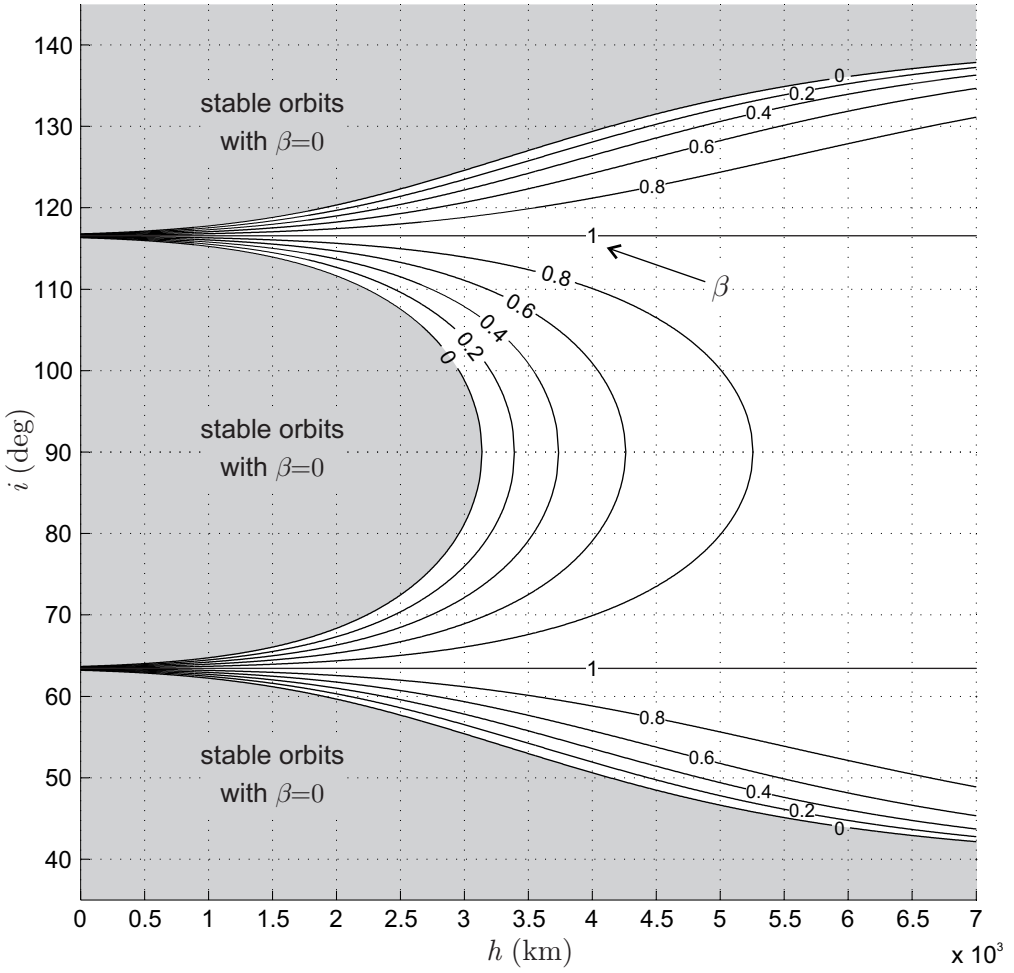

Figure 7.1: Stable circular frozen orbits for Mercury as a function of the inclination i and the altitude $h = a - R_P$.

The use of a Solar Sail (viz, $\beta \neq 0$) results in a stretching of the stability regions, giving the possibility of having stable frozen orbits at higher altitudes for a given inclination.

7.3.2 Case $\omega = 0$ or $\omega = \pi$

Keeping in mind that $H = G\cos i$, the condition to satisfy Eq. (7.9b) with $\omega = 0$ or $\omega = \pi$ is

$$\cos^2 i = \frac{1 - 2\,\gamma(1-\beta)G^5}{5} \tag{7.14}$$

Note that, being $G > 0$ and $\beta < 1$, is $\cos^2 i < 1/5$. Consequently, when $\omega = 0$ or $\omega = \pi$ frozen orbits exist only for $63.435\,\text{deg} < i < 116.565\,\text{deg}$.

Substituting Eq. (7.14) with the condition $\sin\omega = 0$ into Eqs. (7.10), the following stability condition is recovered

$$G > \sqrt[5]{\frac{1}{7\,\gamma(1-\beta)}} \tag{7.15}$$

Indeed, the derivative (7.10c) is trivially zero and the derivative (7.10a) is always positive, then for orbit stability the derivative (7.10b) is required to be positive too. Substituting Eq. (7.15) into Eq. (7.14), a further limitation of the inclination is obtained, whereby it is found that the frozen orbits are stable when $\cos^2 i < 1/7$, corresponding to $67.792\,\text{deg} < i < 112.208\,\text{deg}$.

Figure 7.2 gives the possible frozen orbits for Mercury with $\omega = 0$ or $\omega = \pi$ when the eccentricity is 0.1 or 0.3. Each curve corresponds to a fixed value of the sail lightness number β and gives all the frozen orbits obtainable with that fixed value of β when ω is 0 or π. Note that also unstable orbits are represented according to Eq. (7.15).

The presence of a Solar Sail permits the natural frozen orbits ($\beta = 0$) to be displaced, thus giving more freedom in choosing the pericenter altitude when the remaining orbital parameters are fixed.

7.3.3 Case $\omega = \pm\pi/2$

In this case, Eq. (7.9b) is satisfied by

$$\cos^2 i = \frac{1 + 3\,\gamma(1-\beta)G^5}{5\,[1 + \gamma(1-\beta)G^3]} \tag{7.16}$$

It can be shown that, for $\beta < 1$, $\cos^2 i$ is an increasing function of γ if $G > \sqrt{1/3}$ or, equivalently, if $e < \sqrt{2/3} \approx 0.8165$.

Assuming the eccentricity is less than 0.8165, the limitation $1/5 < \cos^2 i < 3/5G^2$ is found. Therefore, in this case, frozen orbits exist only for $i < 63.435\,\text{deg}$ or $i > 116.565\,\text{deg}$.

To guarantee stability, the derivative (7.10c) is again trivially zero and the derivative (7.10a) is always negative for $\cos^2 i < 3/5G^2 < 3/5$. Therefore, the derivative (7.10b) is required to be negative. It can be shown that such a derivative is negative if

$$2 + 21\,\gamma(1-\beta)G^5 - 15\,\gamma(1-\beta)G^3\cos^2 i > 0 \tag{7.17}$$

which is always satisfied for $\cos^2 i < 3/5G^2$.

If the eccentricity is greater than 0.8165, a frozen orbit exists only for $\cos^2 i < 1/5$, or equivalently for $63.435\,\text{deg} < i < 116.565\,\text{deg}$, and the stability condition of Eq. (7.17) has to be checked on a case-by-case basis.

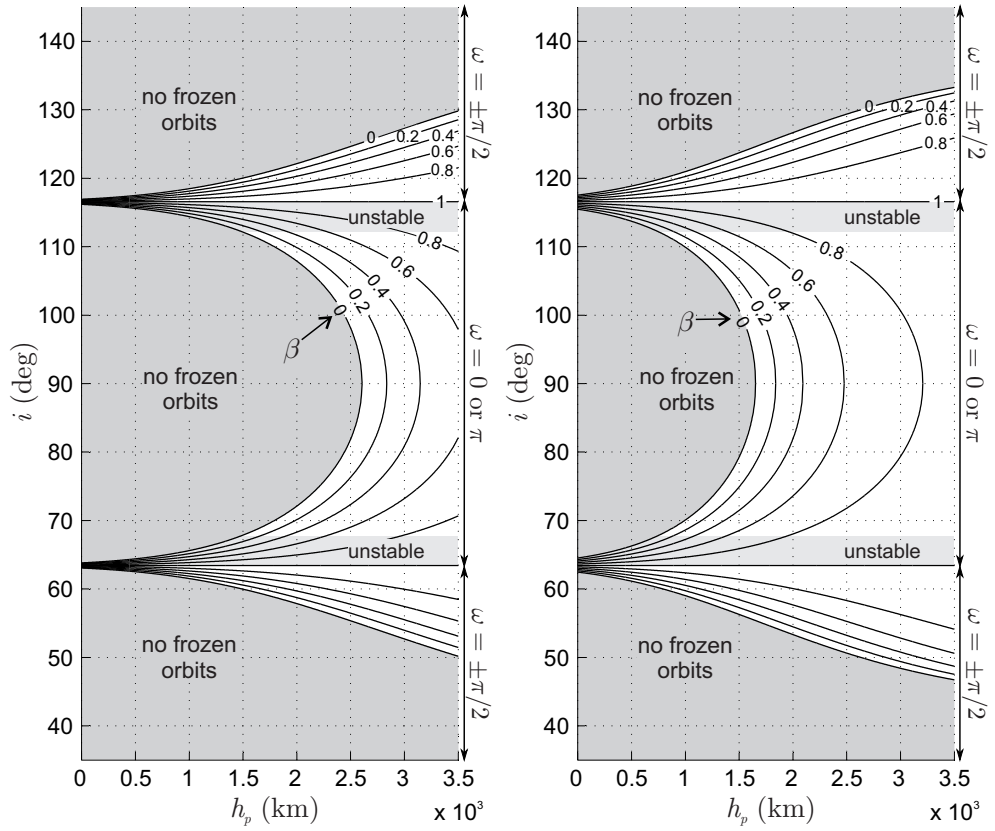

(a) $e = 0.1$ (b) $e = 0.3$

Figure 7.2: Elliptical frozen orbits for Mercury as a function of the inclination i and the pericenter altitude $h_p = a(1-e) - R_P$.

In Fig. 7.2 the frozen orbits when $\omega = \pm\pi/2$ and the eccentricity is 0.1 or 0.3 are shown as a function of the lightness number β. Once more, the natural frozen orbits are displaced towards higher pericenter altitude for a fixed value of the inclination.

7.4 Period of the Frozen Orbits

The Hamiltonian in Eq. (7.8), considered as a function of the two variables ω and G, can be approximated in the neighborhood of an equilibrium point using a Taylor expansion up to the second order as

$$\overline{\mathcal{H}} = \overline{\mathcal{H}}_{\text{eq}} + \frac{1}{2}\left.\frac{\partial^2\overline{\mathcal{H}}}{\partial\omega^2}\right|_{\text{eq}}(\omega-\omega_{\text{eq}})^2 + \frac{1}{2}\left.\frac{\partial^2\overline{\mathcal{H}}}{\partial G^2}\right|_{\text{eq}}(G-G_{\text{eq}})^2 \tag{7.18}$$

where the subscript "eq" stands for evaluated at the equilibrium point, that is for a frozen orbit. Note that in Eq. (7.18) the first derivatives with respect to G

and ω and the mixed second derivatives are omitted since they are zero for the problem under consideration since Eqs. (7.9) and (7.10) hold.

If a stable frozen orbit is taken into account, Eq. (7.18) is the Hamiltonian of a harmonic oscillator with the period of the oscillations given by

$$\tau = \frac{2\pi}{\sqrt{\left.\frac{\partial^2 \overline{\mathcal{H}}}{\partial \omega^2}\right|_{\text{eq}} \left.\frac{\partial^2 \overline{\mathcal{H}}}{\partial G^2}\right|_{\text{eq}}}} \tag{7.19}$$

A similar expression involving second derivatives with respect to x and X is obtained, if the Hamiltonian in Eq. (7.12) for the circular case is expanded.

The period given by Eq. (7.19) is dimensionless. The corresponding dimensional period can be written as

$$T = \frac{\tau\, a^{7/2}}{J_2 R_P^2 \sqrt{\mu_P}} \tag{7.20}$$

since $\overline{\mathcal{H}}$ and G are made non dimensional using $\mu_P J_2 R_P^2/a^3$ and $\sqrt{\mu_P a}$, respectively.

Finally, Eq. (7.20) represents the period of oscillation of a point around an equilibrium of the Hamiltonian in the $\omega - G$ plane or, equivalently, the period of oscillation of the eccentricity vector of a frozen orbit.

7.5 Numerical Simulations

The analytical results obtained by means of the averaging technique described in the previous sections are based on the assumption that non-Keplerian forces acting on the spacecraft can be considered as perturbations with respect to the main force, that is, the gravitational force of the planet. Under that assumption, the instantaneous effect of non-Keplerian forces can be neglected, and the mean motion of the spacecraft is well approximated by considering the average effect over an orbit and over the apparent motion of the Sun.

As the concept of perturbation cannot be well defined quantitatively a priori, numerical investigations of the behavior of the frozen orbits are required to understand when the analytical model is adequate. In the following, the non averaged equations of motion of the satellite are integrated with the aim to understand what are the limitations of the theoretical results.

Simulations are performed with reference to the model of the system illustrated in Fig. 7.3. The model takes into account the accelerations due to the gravitational force of planet (including the J_2 term) and Sun (whose apparent motion is assumed to be elliptical and to lie in the equatorial plane of the planet, that is $\hat{\boldsymbol{n}}_S = \hat{\boldsymbol{n}}_P$) and the acceleration $\boldsymbol{a}_T$ provided by the Solar Sail. Mercury is

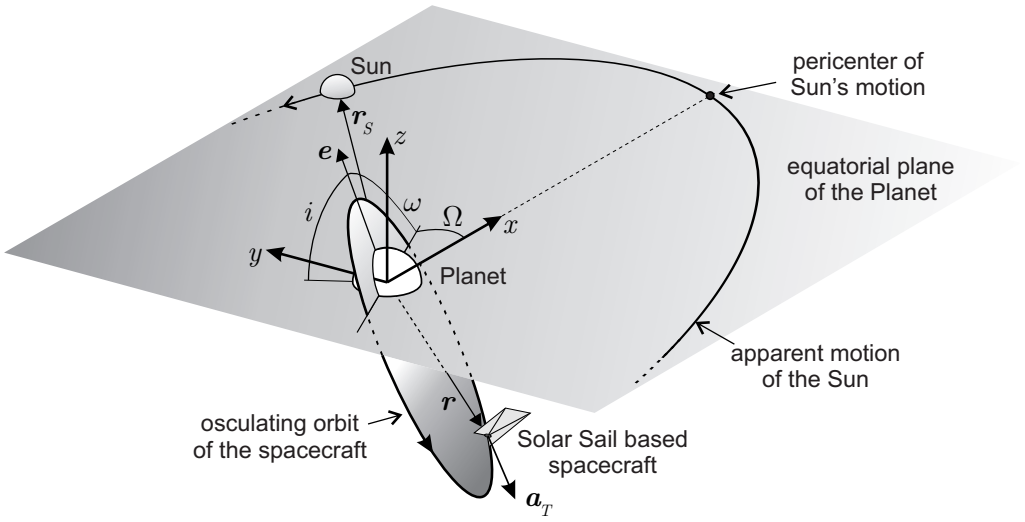

Figure 7.3: Model of the system used for numerical integrations.

used as the reference planet in simulations, so that a non-negligible effect of the planet eccentricity is also included. Note that the considered model neglects the shadowing effect of the planet, the effect of the inclination of the planet rotational axis with respect to the normal of its orbit around the Sun and the effect of all the terms of Eq. (7.2) apart form the C_{00} and C_{20} terms.

To improve the numerical accuracy, the Gauss form of the equations of motion in terms of modified equinoctial elements [115–117] has been integrated, using a variable order Adams-Bashforth-Moulton PECE solver[2].

The initial state of the spacecraft, given in terms of modified equinoctial elements of the osculating orbit, is obtained starting from the Keplerian orbital elements for a spacecraft on a frozen orbit. Four of those orbital elements (a_0, e_0, i_0, ω_0) are calculated using the analytical model discussed previously. The true anomaly ν_0 and the ascending node Ω_0 can be freely chosen as well as the initial mean anomaly of the Sun M_{S_0}. Indeed, they are not defined by the analytical model as they disappear during the averaging process. When not differently stated, they are all set equal to zero. Note that the frame with respect to which the orbits are described is the planet equatorial frame with z-axis along the spin axis of the planet, x-axis in the equatorial plane and pointing toward the pericenter of the apparent motion of the Sun, and y-axis forming a right-handed frame, see Fig. 7.3.

For comparison purposes, simulations are run for frozen orbits with given values e_0, i_0, ω_0 and different values of the sail lightness number β, to which

[2]Implemented in the MATLAB® function `ode113`

correspond different values of the semi-major axes a_0. The data for the simulated frozen orbits are reported in Table 7.2 together with the period of oscillation of the eccentricity vector from Eq. (7.20).

a_0 (km)	e_0	i_0 (deg)	ω_0 (deg)	β	T (years)
6439.86	0.5	90	0	0	29.58
6465.93	0.5	90	0	0.02	30.00
6479.21	0.5	90	0	0.03	30.21

Table 7.2: Initial orbital parameters for numerical simulations.

The simulation results are plotted in Figs. 7.4, 7.5, and 7.7. For each of the simulations of Figs. 7.4–7.7, it is possible to recognize the superimposition of three oscillations at different frequencies. The highest frequency oscillation is on the order of the inverse of the orbital period and corresponds to the variation of orbital elements due to the variation of the perturbing force experienced by the spacecraft during one orbit. The medium frequency oscillation, whose period is on the order of the revolution period of Mercury, is an effect of the motion of the orbit together with Mercury around the Sun. The lowest oscillation frequency corresponds to the oscillation of a harmonic oscillator around its equilibrium point, see Eq. (7.18).

Figure 7.4 shows the simulation of a natural frozen orbit ($\beta = 0$). It presents very small oscillations of the orbital parameters, with a low frequency component having a period of about 30 years, in agreement with Eq. (7.20).

Increasing the lightness number to $\beta = 0.02$ and maintaining the same value of eccentricity and inclination, the semi-major axis of the new frozen orbit tends to increase. In Fig. 7.5 the simulation for that new frozen orbit is shown. Even though the average value of the orbital elements is constant, the amplitude of the oscillations is now large and eventually results in a crash of the spacecraft on Mercury's surface, see Fig. 7.6.

Furthermore, the period of oscillation is of about 50 years with an error of 20 years with respect the value of Table 7.2. Therefore, Eq. (7.20) is inadequate for this case, thus implying that the theoretical model based on the averaging technique is not able to correctly describe the average behavior of such an orbit.

For a greater lightness number ($\beta = 0.03$) the argument of pericenter is continuously increasing, see Fig. 7.7. The orbit is not frozen, and the analytical model fails.

In general, a similar trend characterizes all of the orbit with fixed e_0, i_0, ω_0 when β is increased. Typically, the analytical model fails to predict the right

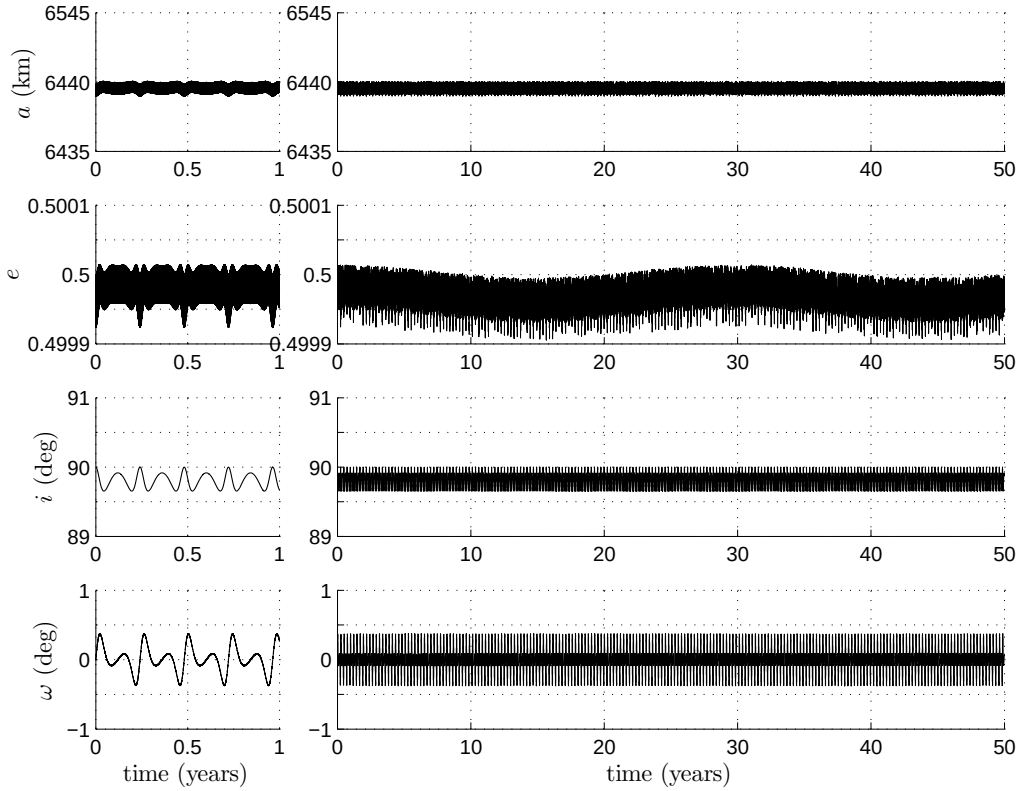

Figure 7.4: Numerical simulation for an orbit (frozen when $\beta = 0$) with initial orbital parameters $a_0 = 6439.86\,\mathrm{km}$, $e_0 = 0.5$, $i_0 = 90\,\mathrm{deg}$, and $\omega_0 = 0\,\mathrm{deg}$, see Table 7.2.

behavior of an orbit when values of β of order 0.01–0.02 are considered, thus suggesting that frozen orbits cannot be found using the proposed method for values of β beyond those limits.

The main reason for such a discrepancy between analytical model and numerical simulations seems to be that the mean behavior predicted by the averaging analysis cannot be considered as a good approximation of the real behavior when the lightness number becomes greater than a value beyond which the effect of the Solar Sail cannot be considered as a simple perturbation effect. Furthermore, the analytical model does not take into account the effects of the initial position of the planet with respect to the Sun, which is lost due to the orbit averaging.

Simulations show that significant effects can be associated with the initial condition in some cases. Figure 7.8 shows the evolution of an orbit, when two different initial position of Mercury with respect to the Sun are set. With Mercury starting at the perihelion, see Fig. 7.8(a), the orbit is not frozen. By setting the initial position of Mercury at the aphelion, where the initial sail acceleration is

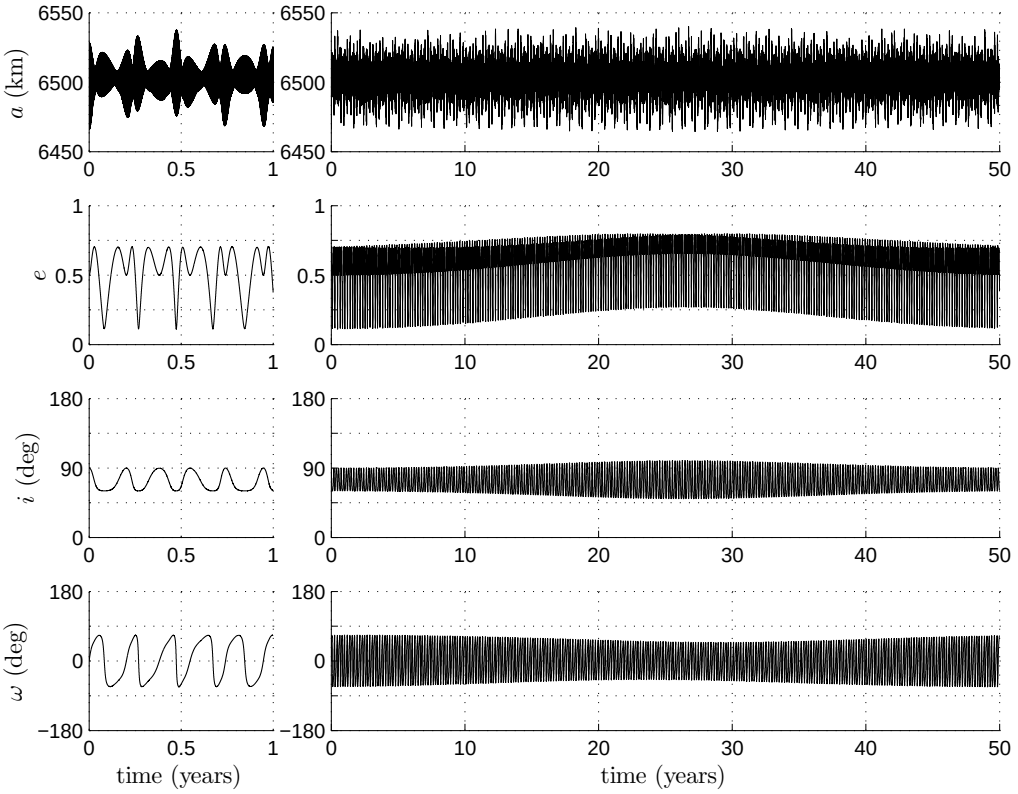

Figure 7.5: Numerical simulation for an orbit (frozen when $\beta = 0.02$) with initial orbital parameters $a_0 = 6465.93\,\mathrm{km}$, $e_0 = 0.5$, $i_0 = 90\,\mathrm{deg}$, and $\omega_0 = 0\,\mathrm{deg}$, see Table 7.2.

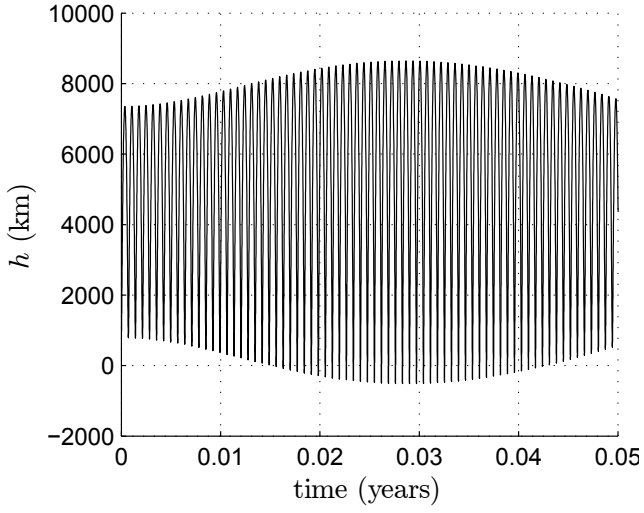

Figure 7.6: Altitude variation for a frozen orbit with $\beta = 0.02$.

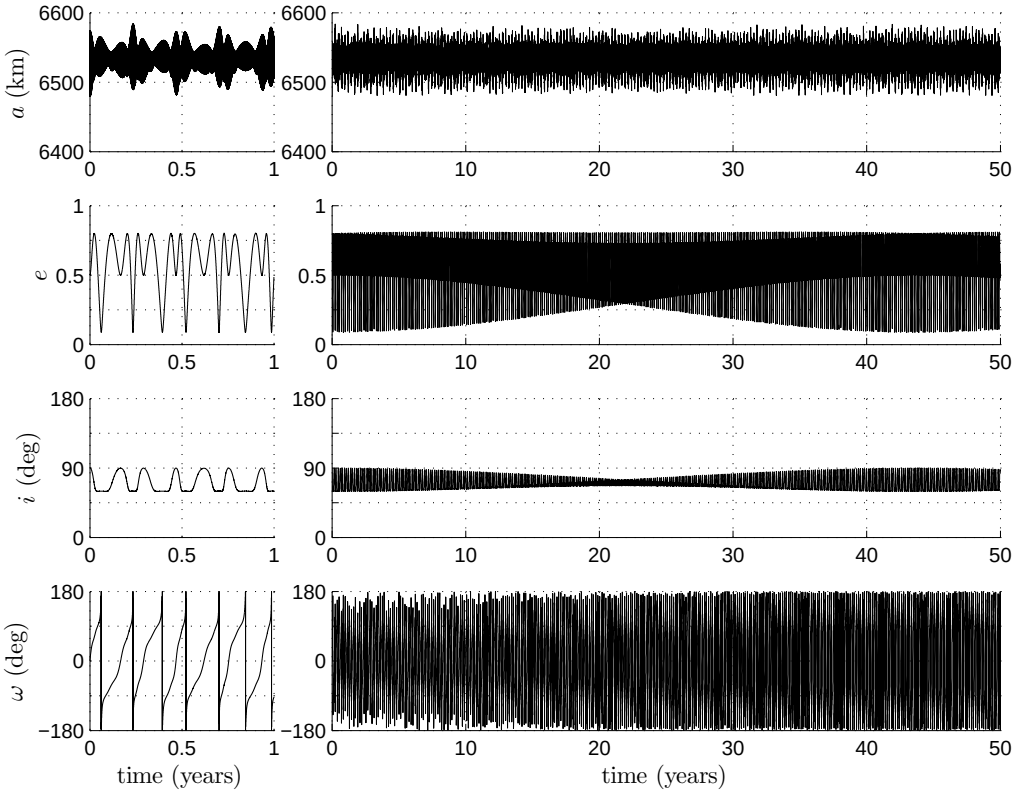

Figure 7.7: Numerical simulation for an orbit (frozen when $\beta = 0.03$) with initial orbital parameters $a_0 = 6479.21\,\mathrm{km}$, $e_0 = 0.5$, $i_0 = 90\,\mathrm{deg}$, and $\omega_0 = 0\,\mathrm{deg}$, see Table 7.2.

minimized, the orbit turns out to be frozen, see Fig. 7.8(b). Other notable effects regard the different amplitudes of oscillation and the different starting slopes in the time evolution of the orbital parameters, resulting in a shift of the mean values of the parameters with respect to the desired ones.

Ultimately, feasible frozen orbits, determined by means the proposed model, can be obtained only for small lightness numbers (on the order of 0.001, corresponding to a characteristic acceleration at 1 AU of about $5.9 \times 10^{-3}\,\mathrm{mm/s^2}$). That implies that the orbital parameters can be modified only by a small amount with respect to the natural frozen orbits. Consequently, the use of a radial Solar Sail to obtain displace frozen orbits is not justified against the complications introduced in the spacecraft design.

However, note that small lightness number are representative of the force due to the solar radiation pressure on a generic spacecraft (even without Solar Sail). From this point of view, the analytical model represents an improvement of previous works regarding natural frozen orbits and permits an estimation of

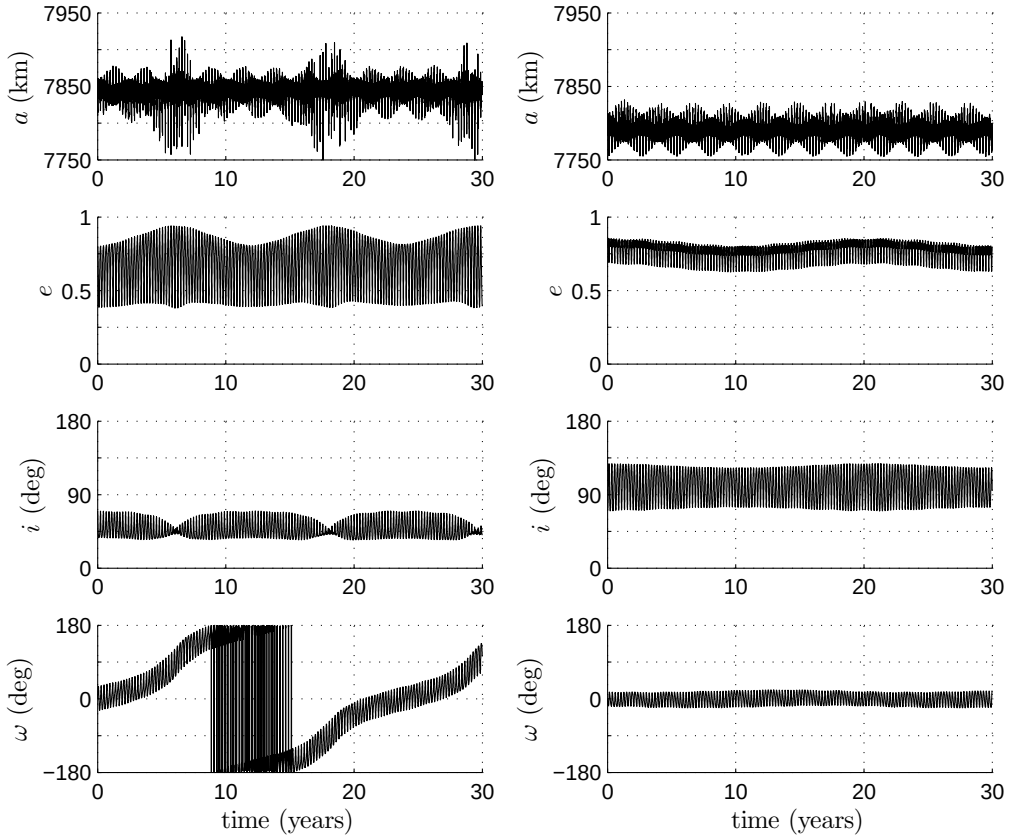

(a) Mercury starting at the perihelion.

(b) Mercury starting at the aphelion.

Figure 7.8: Effect of the initial conditions on the orbital parameters for a frozen orbit with $\beta = 0.01$ defined by $a_0 = 7811.99$, $e_0 = 0.8$, $i_0 = 70\,\mathrm{deg}$, $\omega_0 = 0\,\mathrm{deg}$.

the effect of solar radiation pressure on the natural frozen orbits.

Conclusions

Mission applications for continuous-thrust spacecraft within a Restricted Three-Body Problem have been discussed in this Thesis.

The concept of Generalized Sail has been introduced, explaining its capability of describing different continuous-thrust and purely radial propulsion systems, by means of a unified mathematical model involving only two parameters. The parameters used here are η and β, the first one defining the propulsion system type, and the other quantifying the propulsion system performance.

The introduction of the Generalized Sail propulsive acceleration, as an additional acceleration in a (Circular or Elliptic) Three-Body Problem, is useful for obtaining a parametric approach to the analysis of Artificial Equilibrium Points and studying their stability. The rationales behind the parametric approach is to provide a certain degree of flexibility in dealing with future thrusters and space missions. Moreover, the proposed approach allows one to compare, either in an analytical or graphical form, the performance required by a given propulsion system to produce and maintain a prescribed Artificial Equilibrium Point located on a well-defined locus. Accordingly, it is possible to quickly obtain information about different propulsion systems and decide upon which one could better suited for a particular mission.

A Generalized Sail based spacecraft has also shown its theoretical capability of stabilizing a particular class of Artificial Equilibrium Points (the L_1-type points), by means of a Proportional-Derivative closed loop β-control. However, the gains required to the controller could be not so easily achieved by currently available systems. Indeed, a passively actuated Solar Balloon has shown (within the limitations of the simplified model adopted) its inability of stabilizing L_1-type points using the current technology of Solar Sail materials. An alternative could be offered by materials with sufficiently high values of linear expansion coefficient, even if these values are not currently reachable. On the other hand, Electrochromic Material Panels technology for Solar Sail based spacecraft has been shown to

be able to stabilize L_1-type points by means of an active Proportional-Integral-Derivative closed loop β-control with an anti-windup compensator for control saturation. A simplified mathematical model has been developed to define the main spacecraft parameters, including the sail dimension and the total spacecraft mass, as a function of the desired equilibrium point position and of the desired saturation limits.

When the assumption of radial thrust is left, the existence and stability of Artificial Equilibrium Points for an E-Sail based spacecraft have been investigated within an Elliptical Restricted Three-Body Problem. For mathematical tractability the problem has been solved under the assumption of constant orientation of the E-sail nominal plane with respect to an orbital reference frame. The propulsive acceleration required to generate equilibrium points in the neighborhood of either the L_1 or the L_4 point in the Sun-(Earth+Moon) system are compatible with the capabilities of an E-Sail propulsion system of first generation. Indeed, the amount of propulsive acceleration fluctuation depending on the true anomaly of the planet is moderate and may be compensated through a suitable variation of the E-sail tethers' voltage. The linear stability analysis for the Sun-(Earth+Moon) system has also shown the existence of stable regions of Artificial Equilibrium Points close to the classical equilibrium points L_1 and L_4.

The existence of displaced frozen orbits in a Sun-planet system has been also studied. An analytical derivation of frozen orbits by means of the Hamiltonian averaging technique has been shown to be extendable to a spacecraft equipped with a Solar Sail providing a radial thrust with respect to the Sun. The analytical model points out that new frozen orbits can be created using Solar Sails. To validate the theoretical results, high precision numerical simulations of frozen orbits have been performed for the Sun-Mercury system. Simulations revealed substantial differences between the numerical results and those expected on the basis of the theoretical model. In contrast with the analytical results, no frozen orbits have been found when the lightness number becomes larger than a value on the order of 0.01–0.02.

Appendix

Appendix A

Dimensionless Equation of Motion

A dimensionless form of the equation of motion for a spacecraft with a continuous-thrust propulsion system is here derived, both in the *Elliptic Restricted Three-Body Problem* and in the *Circular Restricted Three-Body Problem*.

Consider a spacecraft under the gravitational effects of two celestial bodies (of mass m_1 and $m_2 < m_1$) and the propulsive acceleration $\boldsymbol{a}_{\mathrm{P}}$ provided by a continuous-thrust propulsion system. The two celestial bodies move on elliptical orbits at an angular velocity $\boldsymbol{\omega} = \omega\hat{\boldsymbol{k}}$ and their reciprocal variable distance is

$$\ell = a(1 - e^2)g \tag{A.1}$$

where

$$g \triangleq \frac{1}{1 + e\cos\nu} \tag{A.2}$$

with a, e and ν semimajor axis, eccentricity and true anomaly of the orbit of smaller celestial body with respect to the bigger one.

Following Szebehely [11] and Battin [14], the equation of motion of the spacecraft in a frame rotating with the two celestial bodies is written as

$$\frac{\mathrm{d}^2(\ell\boldsymbol{r})}{\mathrm{d}t^2} + 2\boldsymbol{\omega}\times\frac{\mathrm{d}(\ell\boldsymbol{r})}{\mathrm{d}t} + \ell\frac{\mathrm{d}\boldsymbol{\omega}}{\mathrm{d}t}\times\boldsymbol{r} + \ell\boldsymbol{\omega}\times(\boldsymbol{\omega}\times\boldsymbol{r}) = -\frac{Gm_1}{\ell^2\rho_1^3}\boldsymbol{\rho}_1 - \frac{Gm_2}{\ell^2\rho_2^3}\boldsymbol{\rho}_2 + \boldsymbol{a}_{\mathrm{P}} \tag{A.3}$$

where $\boldsymbol{\rho}_1$, $\boldsymbol{\rho}_2$, and $\boldsymbol{r}$ (with $\rho_1 \triangleq \|\boldsymbol{\rho}_1\|$ and $\rho_2 \triangleq \|\boldsymbol{\rho}_2\|$) are the dimensionless position vectors of the spacecraft with respect to the two celestial bodies and their center of mass, respectively, while G is the universal gravitational constant.

Using the the angular coordinate ν as independent variable, the equation of

motion becomes

$$\ell\omega^2\left(\boldsymbol{r}'' + 2\hat{\boldsymbol{k}}\times\boldsymbol{r}'\right) + \left(\ell\dot{\omega} + 2\omega\dot{\ell}\right)\left(\boldsymbol{r}'' + \hat{\boldsymbol{k}}\times\boldsymbol{r}\right) + \left(\ddot{\ell} - \ell\omega^2\right)\boldsymbol{r} + \\ + \ell\omega^2(\boldsymbol{r}\cdot\hat{\boldsymbol{k}})\hat{\boldsymbol{k}} = -\frac{Gm_1}{\ell^2\rho_1^3}\boldsymbol{\rho}_1 - \frac{Gm_2}{\ell^2\rho_2^3}\boldsymbol{\rho}_2 + \boldsymbol{a}_{\mathrm{P}} \quad \text{(A.4)}$$

where the prime symbol denotes a derivative taken with respect to ν.

Since the distance ℓ is the solution of the two-body problem involving the two celestial bodies, the following relations are valid:

$$\ddot{\ell} - \ell\omega^2 = -\frac{G(m_1+m_2)}{\ell^2} \quad \text{(A.5a)}$$

$$\ell^2\omega = \sqrt{a(1-e^2)\,G(m_1+m_2)} \quad \text{(A.5b)}$$

$$\ell\dot{\omega} + 2\omega\dot{\ell} = 0 \quad \text{(A.5c)}$$

Using Eq. (A.5) and dividing by $\ell\omega^2$, the equation of motion (A.4) is written as

$$\boldsymbol{r}'' + 2\hat{\boldsymbol{k}}\times\boldsymbol{r}' = -\frac{Gm_1}{\ell^3\omega^2\rho_1^3}\boldsymbol{\rho}_1 - \frac{Gm_2}{\ell^3\omega^2\rho_2^3}\boldsymbol{\rho}_2 + \frac{\boldsymbol{a}_{\mathrm{P}}}{\ell\omega^2} + \frac{G(m_1+m_2)}{\ell^3\omega^2}\boldsymbol{r} - (\boldsymbol{r}\cdot\hat{\boldsymbol{k}})\hat{\boldsymbol{k}} \quad \text{(A.6)}$$

Moreover, using

$$\ell^3\omega^2 = \frac{G(m_1+m_2)}{g} \quad \text{(A.7)}$$

and

$$\boldsymbol{r} = -\hat{\boldsymbol{k}}\times(\hat{\boldsymbol{k}}\times\boldsymbol{r}) + (\boldsymbol{r}\cdot\hat{\boldsymbol{k}})\hat{\boldsymbol{k}} \quad \text{(A.8)}$$

from Eq. (A.6), the dimensionless equation of motion for the *Elliptic Restricted Three-Body Problem* can be written as

$$\boldsymbol{r}'' + 2\hat{\boldsymbol{k}}\times\boldsymbol{r}' = g\left[-\frac{1-\mu}{\rho_1^3}\boldsymbol{\rho}_1 - \frac{\mu}{\rho_2^3}\boldsymbol{\rho}_2 + \frac{\ell^2\boldsymbol{a}_{\mathrm{P}}}{G(m_1+m_2)} - \hat{\boldsymbol{k}}\times\left(\hat{\boldsymbol{k}}\times\boldsymbol{r}\right) - e\cos\nu\left(\boldsymbol{r}\cdot\hat{\boldsymbol{k}}\right)\hat{\boldsymbol{k}}\right] \quad \text{(A.9)}$$

where $\mu = m_2/(m_1+m_2)$ is the dimensionless mass of the smaller celestial body.

In case the two celestial bodies move on circular orbits, their reciprocal distance is constant ($\ell = l$) and the parameter g is unitary. Therefore, the dimensionless equation of motion for the *Circular Restricted Three-Body Problem* is written from Eq. (A.9) as

$$\boldsymbol{r}'' + 2\hat{\boldsymbol{k}}\times\boldsymbol{r}' = -\frac{1-\mu}{\rho_1^3}\boldsymbol{\rho}_1 - \frac{\mu}{\rho_2^3}\boldsymbol{\rho}_2 + \frac{l^2\boldsymbol{a}_{\mathrm{P}}}{G(m_1+m_2)} - \hat{\boldsymbol{k}}\times\left(\hat{\boldsymbol{k}}\times\boldsymbol{r}\right) \quad \text{(A.10)}$$

Appendix B

Entries of $\mathbb{K}$-matrix

The tensor $\boldsymbol{K}$, arising from the linearization of the equation of motion of a spacecraft in the *Circular Restricted Three-Body Problem*, is here expanded. Moreover, the components of $\boldsymbol{K}$ in the rotating frame are derived for each family of *Artificial Equilibrium Point*s.

B.1 Expansion of $\boldsymbol{K}$

Consider the second-order tensor $\boldsymbol{K}$ defined by means of Eq. (3.19), which is here rewritten for convenience

$$\boldsymbol{K} \triangleq \nabla \left[-\frac{1-\mu}{\rho_1^3}\boldsymbol{\rho}_1 - \frac{\mu}{\rho_2^3}\boldsymbol{\rho}_2 + \beta\frac{1-\mu}{\rho_1^{\eta+1}}\boldsymbol{\rho}_1 - \hat{\boldsymbol{k}} \times \left(\hat{\boldsymbol{k}} \times \boldsymbol{r}\right) \right] \Bigg|_{\boldsymbol{r}_0} \tag{B.1}$$

According to Szebehely [11] and Battin [14], the expression defining the tensor $\boldsymbol{K}$ can be expanded as follows

$$\boldsymbol{K} = \Bigg\{ \frac{1-\mu}{\rho_1^5}\left(3\boldsymbol{\rho}_1\boldsymbol{\rho}_1 - \rho_1^2\,\boldsymbol{I}\right) + \frac{\mu}{\rho_2^5}\left(3\boldsymbol{\rho}_2\boldsymbol{\rho}_2 - \rho_2^2\boldsymbol{I}\right) + \\ -\beta\frac{1-\mu}{\rho_1^{\eta+3}}\left[(\eta+1)\boldsymbol{\rho}_1\boldsymbol{\rho}_1 - \rho_1^2\boldsymbol{I}\right] - \boldsymbol{E}^2 \Bigg\} \Bigg|_{\boldsymbol{r}_0} \tag{B.2}$$

The entries of the symmetric matrix $\mathbb{K}$, corresponding to the components of $\boldsymbol{K}$ in the rotating frame $\mathcal{T}\,(C;\ x, y, z)$, are obtained observing that

$$\mathbb{K} = \Bigg\{ \frac{1-\mu}{\rho_1^5}\left(3\left[\boldsymbol{\rho}_1\right]_{\mathcal{T}}\left[\boldsymbol{\rho}_1\right]_{\mathcal{T}}^{\mathrm{T}} - \rho_1^2\,\mathbb{I}\right) + \frac{\mu}{\rho_2^5}\left(3\left[\boldsymbol{\rho}_2\right]_{\mathcal{T}}\left[\boldsymbol{\rho}_2\right]_{\mathcal{T}}^{\mathrm{T}} - \rho_2^2\mathbb{I}\right) + \\ -\beta\frac{1-\mu}{\rho_1^{\eta+3}}\left[(\eta+1)\left[\boldsymbol{\rho}_1\right]_{\mathcal{T}}\left[\boldsymbol{\rho}_1\right]_{\mathcal{T}}^{\mathrm{T}} - \rho_1^2\mathbb{I}\right] - \mathbb{E}^2 \Bigg\} \Bigg|_{\boldsymbol{r}_0} \tag{B.3}$$

where $\mathbb{E}$ is given by Eq. (3.24), and β takes that particular value for which $\boldsymbol{r}_0$ corresponds to an equilibrium position. As a result, the entries of $\mathbb{K}$ take different expressions for the distinct families of AEPs.

B.1.1 Triangular Points

The triangular-type points are characterized by means of the vectors

$$[\boldsymbol{\rho}_1]_{\mathcal{T}} = \begin{bmatrix} \rho_1^2/2 \\ \pm\sqrt{\rho_1^2 - \rho_1^4/4} \\ 0 \end{bmatrix} \quad , \quad [\boldsymbol{\rho}_2]_{\mathcal{T}} = \begin{bmatrix} \rho_1^2/2 - 1 \\ \pm\sqrt{\rho_1^2 - \rho_1^4/4} \\ 0 \end{bmatrix} \tag{B.4}$$

Because β is given by Eq. (3.10), from Eq. (B.3) one obtains

$$k_{11} = \frac{1-\mu}{\rho_1^3}\left(\frac{3\rho_1^2}{4} - 1\right) + \mu\left[3\left(\frac{\rho_1^2}{2} - 1\right)^2 - 1\right] + 1 + \\ - (1-\mu)\left(\frac{1}{\rho_1^3} - 1\right)\left(\frac{\eta+1}{4}\rho_1^2 - 1\right) \tag{B.5}$$

$$k_{22} = \eta(1-\mu) + 1 + 2\mu - \frac{(1-\mu)(\eta-2)}{\rho_1^3} - k_{11} \tag{B.6}$$

$$k_{33} = -1 \tag{B.7}$$

$$k_{12} = k_{21} = \pm\sqrt{\rho_1^2 - \frac{\rho_1^4}{4}}\left[\frac{3\,(1-\mu)}{2\,\rho_1^3} + 3\mu\left(\frac{\rho_1^2}{2} - 1\right) - \frac{(1-\mu)(\eta+1)}{2}\left(\frac{1}{\rho_1^3} - 1\right)\right] \tag{B.8}$$

$$k_{13} = k_{31} = k_{23} = k_{32} = 0 \tag{B.9}$$

where the sign of the terms containing $\pm$ is $+$ for points with $y > 0$ ad $-$ for points with $y < 0$.

B.1.2 Collinear Points

L_3-type

The expression for β is obtained by combining Eq. (3.13) and

$$[\boldsymbol{\rho}_1]_{\mathcal{T}} = -[\rho_1 \quad 0 \quad 0]^{\mathrm{T}} \quad , \quad [\boldsymbol{\rho}_2]_{\mathcal{T}} = -[(\rho_1 + 1) \quad 0 \quad 0]^{\mathrm{T}} \tag{B.10}$$

Therefore, Eq. (B.3) gives the following results

$$k_{11} = (2-\eta)\left(\frac{1-\mu}{\rho_1^3} + \frac{\mu}{(\rho_1+1)^3}\right) + \eta\,(1 - k_{22}) + 1 \tag{B.11}$$

$$k_{22} = \frac{\mu}{\rho_1}\left[\frac{1}{(\rho_1+1)^3} - 1\right] \tag{B.12}$$

$$k_{33} = k_{22} - 1 \tag{B.13}$$

$$k_{12} = k_{21} = k_{23} = k_{32} = k_{13} = k_{31} = 0 \tag{B.14}$$

Note that Eq. (B.11) can also be rearranged into the following equivalent expression:

$$k_{11} = -\frac{\partial \beta}{\partial \rho_1} \left(\frac{1-\mu}{\rho_1^{\eta}} \right) \tag{B.15}$$

L_1-type and L_2-type

In this case

$$[\boldsymbol{\rho}_1]_{\mathcal{T}} = [\rho_1 \quad 0 \quad 0]^{\mathrm{T}} \quad , \quad [\boldsymbol{\rho}_2]_{\mathcal{T}} = [(\rho_1 - 1) \quad 0 \quad 0]^{\mathrm{T}} \tag{B.16}$$

and Eq. (B.3) with Eq. (3.13) provide

$$k_{11} = (2-\eta) \left(\frac{1-\mu}{\rho_1^3} \pm \frac{\mu}{(\rho_1 - 1)^3} \right) + \eta \, (1 - k_{22}) + 1 \tag{B.17}$$

$$k_{22} = \frac{\mu}{\rho_1} \left[1 \pm \frac{1}{(1-\rho_1)^3} \right] \tag{B.18}$$

$$k_{33} = k_{22} - 1 \tag{B.19}$$

$$k_{12} = k_{21} = k_{23} = k_{32} = k_{13} = k_{31} = 0 \tag{B.20}$$

where the sign of the terms containing $\pm$ is $+$ for L_2-type points and $-$ for L_1-type points.

Similarly to the L_3-type points, Eq. (B.17) can be rearranged as follows

$$k_{11} = -\frac{\partial \beta}{\partial \rho_1} \left(\frac{1-\mu}{\rho_1^{\eta}} \right) \tag{B.21}$$

B.1.3 Displaced Points

In this last case one has

$$[\boldsymbol{\rho}_1]_{\mathcal{T}} = [\rho_{1_x} \quad 0 \quad \rho_{1_z}]^{\mathrm{T}} \quad , \quad [\boldsymbol{\rho}_2]_{\mathcal{T}} = [\rho_{2_x} \quad 0 \quad \rho_{1_z}]^{\mathrm{T}} \tag{B.22}$$

where

$$\rho_{1_x} = \rho_{2_x} + 1 = \mu(1 - 1/\rho_2^3) \quad , \quad \rho_{1_z} = \pm \sqrt{\rho_2^2 - \left(-\mu/\rho_2^3 + \mu - 1 \right)^2} \tag{B.23}$$

Substituting the expression (3.15) for β into Eq. (B.3) provides:

$$k_{11} = \frac{1-\mu}{\rho_1^5}\left(3\rho_{1_x}^2 - \rho_1^2\right) + \frac{\mu}{\rho_2^5}\left(3\rho_{2_x}^2 - \rho_2^2\right) + 1 - \frac{\left[(\eta+1)\rho_{1_x}^2 - \rho_1^2\right]}{\rho_1^2}\left(\frac{1-\mu}{\rho_1^3} + \frac{\mu}{\rho_2^3}\right) \tag{B.24}$$

$$k_{22} = 1 \tag{B.25}$$

$$k_{33} = \frac{1-\mu}{\rho_1^5}\left(3\rho_{1_z}^2 - \rho_1^2\right) + \frac{\mu}{\rho_2^5}\left(3\rho_{2_z}^2 - \rho_2^2\right) + 1 - \frac{\left[(\eta+1)\rho_{1_z}^2 - \rho_1^2\right]}{\rho_1^2}\left(\frac{1-\mu}{\rho_1^3} + \frac{\mu}{\rho_2^3}\right) \tag{B.26}$$

$$k_{13} = k_{31} = \rho_{1_z}\left[3\frac{1-\mu}{\rho_1^5}\rho_{1_x} + \frac{3\,\mu\,\rho_{2_x}}{\rho_2^5} - \frac{(\eta+1)\rho_{1_x}}{\rho_1^2}\left(\frac{1-\mu}{\rho_1^3} + \frac{\mu}{\rho_2^3}\right)\right] \tag{B.27}$$

$$k_{12} = k_{21} = k_{23} = k_{32} = 0 \tag{B.28}$$

where $\rho_1 = \sqrt{\rho_2^2 - 1 + 2\,\mu\,\left(1 - 1/\rho_2^3\right)}$ and the sign of the terms containing $\pm$ is $+$ for points with $z > 0$ ad $-$ for points with $z < 0$.

Appendix C

Expansion of Tensor $\boldsymbol{H}$

The second order tensor $\boldsymbol{H}$ arising from the linearization of the equation of motion for an E-Sail in the *Elliptic Restricted Three-Body Problem* is here expanded. The result is an expression suitable for evaluating the component of such a tensor in a synodic reference frame.

C.1 Expansion of $\boldsymbol{H}$

From Eq. (5.13), the tensor $\boldsymbol{H}$ is written as

$$\boldsymbol{H} = \left\{ \nabla(-\boldsymbol{f}) + B\,(1-\mu)\,\nabla\left(\frac{\hat{\boldsymbol{a}}_{\mathrm{P}}}{\rho_1}\right) - e\,\cos\nu\,\nabla\left[\left(\boldsymbol{r}\cdot\hat{\boldsymbol{k}}\right)\,\hat{\boldsymbol{k}}\right] \right\}\Bigg|_0 \tag{C.1}$$

where $\hat{\boldsymbol{a}}_{\mathrm{P}}$ is given by Eq. (5.6). According to Szebehely [11] and Battin [14]

$$\nabla(-\boldsymbol{f}) = \frac{1-\mu}{\rho_1^5}\left(3\,\boldsymbol{\rho}_1\,\boldsymbol{\rho}_1 - \rho_1^2\,\boldsymbol{I}\right) + \frac{\mu}{\rho_2^5}\left(3\,\boldsymbol{\rho}_2\,\boldsymbol{\rho}_2 - \rho_2^2\,\boldsymbol{I}\right) - \boldsymbol{E}^2 \tag{C.2}$$

$$\nabla\left[\left(\boldsymbol{r}\cdot\hat{\boldsymbol{k}}\right)\,\hat{\boldsymbol{k}}\right] = \hat{\boldsymbol{k}}\,\hat{\boldsymbol{k}} \tag{C.3}$$

where $\boldsymbol{I}$ is the identity second order tensor. The term including the acceleration unit vector becomes

$$\nabla\left(\frac{\hat{\boldsymbol{a}}_{\mathrm{P}}}{\rho_1}\right) = \frac{1}{\rho_1}\left(\nabla\hat{\boldsymbol{a}}_{\mathrm{P}} - \frac{\hat{\boldsymbol{\rho}}_1\hat{\boldsymbol{a}}_{\mathrm{P}}}{\rho_1}\right) \tag{C.4}$$

where

$$\nabla\hat{\boldsymbol{a}}_{\mathrm{P}} = \cos\overline{\alpha}\,\nabla\hat{\boldsymbol{\rho}}_1 + \sin\overline{\alpha}\,\left(\cos\overline{\delta}\,\nabla\hat{\boldsymbol{t}} + \sin\overline{\delta}\,\nabla\hat{\boldsymbol{n}}\right) \tag{C.5}$$

The gradients of the unit vectors $\hat{\boldsymbol{\rho}}_1$, $\hat{\boldsymbol{t}}$ and $\hat{\boldsymbol{n}}$ can be further expanded to yield:

$$\nabla\hat{\boldsymbol{\rho}}_1 = \frac{\boldsymbol{I} - \hat{\boldsymbol{\rho}}_1\hat{\boldsymbol{\rho}}_1}{\rho_1} \tag{C.6}$$

$$\nabla\hat{\boldsymbol{t}} = \frac{\boldsymbol{E}\cdot\left(\hat{\boldsymbol{t}}\hat{\boldsymbol{t}} - \boldsymbol{I}\right)}{\rho_1\|\boldsymbol{E}\cdot\hat{\boldsymbol{\rho}}_1\|} \tag{C.7}$$

$$\nabla\hat{\boldsymbol{n}} = \frac{\boldsymbol{T} - \hat{\boldsymbol{\rho}}_1\hat{\boldsymbol{n}}}{\rho_1} + \frac{\boldsymbol{E}\cdot\left(\hat{\boldsymbol{t}}\hat{\boldsymbol{n}} + \boldsymbol{P}\right)}{\|\boldsymbol{E}\cdot\hat{\boldsymbol{\rho}}_1\|} \tag{C.8}$$

where $\boldsymbol{E}$ is defined in Eq. (4.15), whereas $\boldsymbol{T}$ and $\boldsymbol{P}$ are defined by

$$\boldsymbol{T}\cdot\boldsymbol{r} = \hat{\boldsymbol{t}}\times\boldsymbol{r} \quad \text{and} \quad \boldsymbol{P}\cdot\boldsymbol{r} = \hat{\boldsymbol{\rho}}_1\times\boldsymbol{r} \tag{C.9}$$

Appendix D

Floquet Theory for Linear Ordinary Differential Equations with Periodic Coefficients

The Floquet theory[1] for a system of linear, homogeneous, ordinary differential equations with T-periodic coefficient is here presented to address the study of linear stability in the *Elliptic Restricted Three-Body Problem*.

D.1 Definition of the Solution

Consider a system of linear, homogeneous, ordinary differential equations

$$\dot{\boldsymbol{x}} = \mathbb{A}(t)\boldsymbol{x} \tag{D.1}$$

where $\mathbb{A}(t)$ is a complex-valued, piecewise continuous $n \times n$ matrix such that $\mathbb{A}(t+T) = \mathbb{A}(t)$ with $T > 0$.

Theorem D.1 Floquet Theorem
Every fundamental matrix solution $\mathbb{F}(t)$ of the system (D.1) has the form

$$\mathbb{F}(t) = \mathbb{P}(t)e^{\mathbb{B}t} \tag{D.2}$$

where $\mathbb{P}$ and $\mathbb{B}$ are $n \times n$ matrices with $\mathbb{P}(t+T) = \mathbb{P}(t)$ and $\mathbb{B}$ is constant.

Definition D.1 Monodromy matrix.
A monodromy matrix associated to a fundamental solution $\mathbb{F}(t)$ is a nonsingular, constant, $n \times n$ matrix $\mathbb{M}$ that satisfies the relation

$$\mathbb{F}(t+T) = \mathbb{F}(t)\mathbb{M} \tag{D.3}$$

Note that the monodromy matrix associated to the fundamental solution $\mathbb{F}(t)$ is associated to the matrix $\mathbb{B}$ through the relation $\mathbb{M} = e^{\mathbb{B}T}$. Moreover, a particular

[1] This appendix has been adapted from Ref. [12].

monodromy matrix is $\mathbb{M} = \mathbb{F}(T)$ obtained when $\mathbb{F}(t)$ is the fundamental matrix solution with initial condition $\mathbb{F}(0) = \mathbb{I}$, where $\mathbb{I}$ is the $n \times n$ identity matrix.

In principle, to obtain a monodromy matrix, the differential equation

$$\mathbb{F}' = \mathbb{A}(t)\,\mathbb{F} \qquad , \qquad \mathbb{F}(0) = \mathbb{I} \tag{D.4}$$

needs to be numerically integrated over the interval $t \in [0, T]$. However, for a chosen numerical method, it is possible to reduce the calculation volume of about 50% [118] if matrix $\mathbb{A}(t)$ satisfies the so-called Hale's property-E [12]:

$$\mathbb{A}(-t) = -\mathbb{S}\,\mathbb{A}(t)\,\mathbb{S} \qquad \text{with} \qquad \mathbb{S}^2 = \mathbb{I} \tag{D.5}$$

In accordance to Meire and Vanderbauwhede [118], the monodromy matrix associated to the fundamental matrix solution with initial condition $\mathbb{F}(0) = \mathbb{I}$ can be found using the relationship:

$$\mathbb{M} = \mathbb{S}\,\mathbb{F}^{-1}(T/2)\,\mathbb{S}\,\mathbb{F}(T/2) \tag{D.6}$$

In other terms, using the Hale's property-E the differential system (D.4) can be integrated over the interval $\nu \in [0, T/2]$, thus reducing the computational time and increasing the computational accuracy (due to a lower propagation of integration errors).

Definition D.2 Characteristic (or Floquet) multipliers.
The eigenvalues λ of a monodromy matrix are called the characteristic multipliers of the system of differential equations.

The characteristic multipliers do not depend on the particular fundamental matrix chosen to determine a monodromy matrix. In fact, if $\mathbb{F}_1(t)$ and $\mathbb{F}_2(t)$ are two fundamental matrix of the system, then there is a nonsingular matrix $\mathbb{C}$ such that $\mathbb{F}_1(t) = \mathbb{F}_2(t)\mathbb{C}$. If $\mathbb{F}_1(t+T) = \mathbb{F}_1(t)\mathbb{M}$, then $\mathbb{F}_2(t+T) = \mathbb{F}_1(t+T)\mathbb{C} = \mathbb{F}_1(t)\mathbb{M}\mathbb{C} = \mathbb{F}_2(t)\mathbb{C}^{-1}\mathbb{M}\mathbb{C}$ and $\mathbb{C}^{-1}\mathbb{M}\mathbb{C}$ is the monodromy matrix for the fundamental matrix solution $\mathbb{F}_2(t)$. Consequently, the two monodromy matrices associated to the two fundamental matrices are similar, and similar matrices have the same eigenvalues.

Definition D.3 Characteristic (or Floquet) exponents.
Any ρ such that $\lambda = e^{\rho T}$ is called the characteristic exponents of the system of differential equations.

Note that the characteristic exponents are the eigenvalues of the matrix $\mathbb{B}$, since $\mathbb{M} = e^{\mathbb{B}T}$.

D.2 Stability of the Solution

Based on Eq. (D.2), the stability of the system (D.1) depends only on the real part of the eigenvalues ρ of the matrix $\mathbb{B}$, since $\mathbb{P}(t)$ is bounded. Consequently, stability depends on characteristic multipliers.

Theorem D.2 (Stability of periodic systems)
A periodic linear system is stable if all characteristic (or Floquet) multipliers satisfy $|\rho| \leq 1$ (respectively all characteristic exponents have negative real part) and for all characteristic multipliers with $|\rho| = 1$ (respectively all characteristic exponents with null real part) the algebraic and geometric multiplicities are equal.

Bibliography

[1] Stuhlinger, E., *Ion propulsion for space flight*, chap. 1, McGraw-Hill series in missile and space technology, McGraw-Hill, New York, 1964, pp. 1–10.

[2] Choueiri, E. Y., "A critical history of electric propulsion: the first 50 years (1906–1956)," *Journal of Propulsion and Power*, Vol. 20, No. 2, March–April 2004, pp. 193–203. doi: 10.2514/1.9245.

[3] Tsiolkovskiy, K. E., *Works on rocket technology*, chap. 3, NASA TT F-243, 1965, p. 95, Translation of "Труды по ракетной технике", Publishing House of the Defense Ministry, Moscow, 1947.

[4] Tsander, F. A., *From a scientific heritage*, chap. 7, NASA TT F-541, 1969, p. 29, Translation of "Из научного наследия", Nauka Press, Moscow, 1967.

[5] Andrews, D. G. and Zubrin, R. M., "Magnetic sails and interstellar travel," *Journal of The British Interplanetary Society*, Vol. 43, No. 6, June 1990, pp. 265–272.

[6] Janhunen, P., "Electric sail for spacecraft propulsion," *Journal of Propulsion and Power*, Vol. 20, No. 4, July-August 2004, pp. 763–764. doi: 10.2514/1.8580.

[7] Frisbee, R. H., "Advanced space propulsion for the 21st century," *Journal of Propulsion and Power*, Vol. 19, No. 6, November–December 2003, pp. 1129–1154.

[8] McKay, R. J., Macdonald, M., Biggs, J., and McInnes, C. R., "Survey of highly non-keplerian orbits with low-thrust propulsion," *Journal of Guidance, Control and Dynamics*, Vol. 34, No. 3, May-June 2011, pp. 645–666. doi: 10.2514/1.52133.

[9] West, J. L., "The Geostorm warning mission: enhanced opportunities based on new technology," *14th AAS/AIAA Space Flight Mechanics Conference*, Maui, HI, February 8–12 2004, Paper AAS 04-102.

[10] Sauer, Jr., C. G., "The L1 diamond affair," *14th AAS/AIAA Space Flight Mechanics Conference*, Maui, HI, February 8–12 2004, Paper AAS 04-278.

[11] Szebehely, V., *Theory of orbits: the restricted problem of three bodies*, chap. 1, 5, 10, Academic Press, New York, 1967, pp. 7–25, 250, 587–602, ISBN: 0126806500.

[12] Hale, J. K., *Ordinary differential equations*, chap. 8, Dover Publications, Inc., 2009, pp. 117–121, 280, ISBN: 0–486–47211–6.

[13] Eastham, M. S. P., *The spectral theory of periodic differential equations*, chap. 1, Scottish Acedemic Press, 1973, pp. 1–15.

[14] Battin, R. H., *An Introduction to the mathematics and methods of Astrodynamics*, chap. 8, AIAA, New York, 1987, pp. 371–381, ISBN: 1563473429.

[15] Dusek, H. M., "Motion in the vicinity of libration points of a generalized restricted three body model," AIAA/ION Astrodynamics Specialist Conference, AIAA, Monterey, California, September 16-17 1965, AIAA Paper 65-682.

[16] Morimoto, M., Yamakawa, H., and Uesugi, K., "Artificial equilibrium points in the low-thrust restricted three-body problem," *Journal of Guidance, Control and Dynamics*, Vol. 30, No. 5, September-October 2007, pp. 1563–1567. doi: 10.2514/1.26771.

[17] Bombardelli, C. and Peláez, J., "On the stability of artificial equilibrium points in the circular restricted three-body problem," *Celestial Mechanics and Dynamical Astronomy*, Vol. 109, No. 1, January 2011, pp. 13–26. doi: 10.1007/s10569-010-9317-z.

[18] Zubrin, R. M. and Andrews, D. G., "Magnetic sails and interplanetary travel," *Journal of Spacecraft and Rockets*, Vol. 28, No. 2, March-April 1991, pp. 197–203. doi: 10.2514/3.26230.

[19] McInnes, C. R., *Solar sailing: technology, dynamics and mission applications*, Springer-Praxis Series in Space Science and Technology, Springer-Verlag, 1999, ISBN: 1-852-33102-X.

[20] Janhunen, P., "The electric solar wind sail status report," Vol. 5, European Planetary Science Congress, September 19–24 2010, Paper EPSC 2010-297.

[21] Winglee, R. M., Slough, J., Ziemba, T., and Goodson, A., "Mini-magnetospheric plasma propulsion: tapping the energy of the solar wind for spacecraft propulsion," *Journal of Geophysical Research*, Vol. 105, No. A9, September 2000, pp. 21,067–21,077.

[22] Hunt, M. E., "High efficiency dynamic radioisotope power system for space exploration - a status report," *IEE AES System Magazine*, Vol. 8, No. 12, December 1993, pp. 18–23. doi: 10.1109/62.246037.

[23] Lyngvi, A. E., van den Berg, M. L., and Falkner, P., "Study overview of the interstellar heliopause probe," Tech. Rep. 3 (revision 4), ESA, 17 April 2007, reference: SCI-A/2006/114/IHP. Available online `http://esagrid.esa.int/science-e/www/object/index.cfm?fobjectid=40926`.

[24] Jahn, R. G., *Physics of electric propulsion*, chap. 1, Dover Publications, Inc., 1968, pp. 2–11, ISBN: 0-486-45040-6.

[25] Sauer, Jr., C. G., "Modeling of thruster and solar array characteristics in the JPL low-thrust trajectory analysis," 13th International Electric Propulsion Conference, San Diego, CA, USA, April 25–27 1978, paper AIAA 78-645.

[26] Rayman, M. D. and Williams, S. N., "Design of the first interplanetary solar electric propulsion mission," *Journal of Spacecraft and Rockets*, Vol. 39, No. 4, July-August 2002, pp. 589–595. doi: 10.2514/2.3848.

[27] Richardson, A. J. and Warren, J. W., "Solar array degradation due to meteoroid impacts during extended planetary missions," *Journal of Spacecraft and Rockets*, Vol. 8, No. 6, June 1971, pp. 681–683. doi: 10.2514/3.59713.

[28] Bourke, R. D. Sauer, G. G. J., "The effect of solar array degradation on electric propulsion spacecraft performance," *AIAA 9th Electric Propulsion Conference*, Bethesda, MD, USA, April 17–19 1972, Paper AIAA 72-444.

[29] Radzievskii, V. V., "The restricted problem of three bodies taking account of light pressure," *Akad. Nauk. USSR Astron. Journal*, Vol. 27, 1950, pp. 250.

[30] Perezhogin, A. A., "Stability of the sixth and seventh libration points in the photogravitational restricted circular three-body problem," *Soviet Astronomy Letters*, Vol. 2, September 1976, pp. 174–175.

[31] Kunitsyn, A. L. and Perezhogin, A. A., "On the stability of triangular libration points of the photogravitational restricted circular three–body problem," *Celestial Mechanics*, Vol. 18, November 1978, pp. 395–408. doi: 10.1007/BF01230352.

[32] Schuerman, D. W., "The restricted three-body problem including radiation pressure," *Astrophysical Journal, Part 1*, Vol. 238, No. 1, May 1980, pp. 337–342. doi: 10.1086/157989.

[33] Simmons, J. F. L., McDonald, A. J. C., and Brown, J. C., "The restricted 3-body problem with radiation pressure," *Celestial Mechanics*, Vol. 35, No. 2, February 1985, pp. 145–187. doi: 10.1007/BF01227667.

[34] Perezhogin, A. A. and Tureshbaev, A. T., "Stability of coplanar libration points in the photogravitational restricted three–body problem," *Soviet Astronomy Letters ASTR.*, Vol. 33, No. 4, July 1989, pp. 445–448.

[35] McInnes, C. R., McDonald, A. J. C., Simmons, J. F. L., and MacDonald, E. W., "Solar sail parking in restricted three-body systems," *Journal of Guidance, Control, and Dynamics*, Vol. 17, No. 2, March-April 1994, pp. 399–406. doi: 10.2514/3.21211.

[36] McInnes, C. R., "Artificial Lagrange points for a partially reflecting flat solar sail," *Journal of Guidance, Control, and Dynamics*, Vol. 22, No. 1, January-February 1999, pp. 185–187. doi: 10.2514/2.7627.

[37] Baig, S. and McInnes, C. R., "Artificial three-body equilibria for hybrid low-thrust propulsion," *Journal of Guidance, Control, and Dynamics*, Vol. 31, No. 6, November-December 2008, pp. 1644–1654. doi: 10.2514/1.36125.

[38] Abramowitz, M. and Stegun, I. A., *Handbook of mathematical functions: with formulas, graphs, and mathematical tables*, chap. 3, Dover Publications, June 1965 1965, p. 17, ISBN: 0486612724.

[39] Henrici, P., *Applied and computational complex analysis, power series integration conformal mapping location of zero*, Vol. 1, chap. 6, Wiley-Interscience, February 23 1988, p. 442, ISBN: 0471608416.

[40] Danby, J. M. A., "Stability of the Ttiangular points in the elliptic restricted problem of the three bodies," *The Astronomical Journal*, Vol. 69, No. 2, March 1964, pp. 165–172. doi: 10.1086/109254.

[41] Bennet, A., "Characteristic exponents of the five equilibrium solutions in the elliptically restricted problem," *Icarus*, Vol. 4, No. 2, May 1965, pp. 177–187. doi: 10.1016/0019-1035(65)90060-6.

[42] Alfriend, K. T. and Rand, R. H., "Stability of the triangular Points in the elliptic restricted problem of three bodies," *AIAA Journal*, Vol. 7, No. 6, June 1969, pp. 1024–1028. doi: 10.2514/3.5270.

[43] Deprit, A. and Rom, A., "Characteristic exponents at L_4 in the elliptic restricted problem," *Astronomy and Astrophysics*, Vol. 5, No. 3, 1970, pp. 416–425.

[44] Giacaglia, G. E. O., "Characteristic exponents al L_4 and L_5 in the elliptic restricted problem of three bodies," *Celestial Mechanics*, Vol. 4, No. 3–4, December 1971, pp. 468–489. doi: 10.1007/BF01231404.

[45] Tschauner, J., "Die Bewegung in der Nähe der Dreieckspunkte des elliptischen eingeschränkten Dreikörperproblems," *Celestial Mechanics*, Vol. 3, No. 2, June 1971, pp. 189–196. doi: 10.1007/BF01228032.

[46] Vinh, N., "Sur la stabilité des points d'équilibre triangulaires dans le problème restreint elliptique." *Celestial Mechanics*, Vol. 6, No. 3, November 1972, pp. 305–321. doi: 10.1007/BF01231474.

[47] Tschauner, J., "Die Bewegung in der Nähe der Dreieckspunkte des elliptischen eingeschränkten Dreikörperproblems II," *Celestial Mechanics*, Vol. 9, No. 4, July 1974, pp. 419–435. doi: 10.1007/BF01329324.

[48] Meire, R., "The stability of triangular equilibrium points in the elliptic restricted problem," *Celestial Mechanics*, Vol. 23, No. 1, October 1981, pp. 89–95. doi: 10.1007/BF01228547.

[49] Meire, R., "On the stability of the triangular points in the elliptic restricted problem," *Astronomy and Astrophysics*, Vol. 110, June 1982, pp. 152–155.

[50] Kumar, V. and Choudhry, R. K., "Nonlinear stability of the triangular libration points for the photogravitational elliptic restricted problem of three bodies," *Celestial Mechanics and Dynamical Astronomy*, Vol. 48, No. 4, December 1990, pp. 299–317. doi: 10.1007/BF00049387.

[51] Markellos, V. V., Perdios, E., and Labropoulou, P., "Linear stability of the triangular points in the photogravitational elliptic restricted problem, I," *Astrophysics and Space Science*, Vol. 194, No. 2, August 1992, pp. 207–213. doi: 10.1007/BF00643991.

[52] Markellos, V. V., Perdios, E., and Georghiou, C., "Linear stability of the triangular equilibrium points in the photogravitational elliptic restricted problem, II," *Astrophysics and Space Scienc*, Vol. 199, No. 1, January 1993, pp. 23–33. doi: 10.1007/BF00612974.

[53] Markellos, V. V., Perdios, E., and Papadakis, K., "The stability of inner collinear equilibrium points in the photogravitational elliptic restricted

problem," *Astrophysics and Space Science*, Vol. 199, No. 1, January 1993, pp. 139–146. doi: 10.1007/BF00612984.

[54] Baoyin, H. and McInnes, C. R., "Solar sail equilibria in the elliptical restricted three-body problem." *Journal of Guidance, Control, and Dynamics*, Vol. 29, No. 3, May-June 2006, pp. 538–543. doi: 10.2514/1.15596.

[55] Macdonald, M., Mckay, R. J., Vasile, M., Bosquillon de Frescheville, F., Biggs, J. D., and McInnes, C. R., "Low-thrust enabled highly non-keplerian orbits in support of future mars exploration," *Journal of Guidance, Control and Dynamics*, Vol. 35, No. 5, September-October 2011, pp. 1396–1411. doi: 10.2514/1.52602.

[56] Luzum, B., Capitaine, N., Fienga, A., Folkner, W., Fukushima, T., Hilton, J., Hohenkerk, C., Krasinsky, G., Petit, G., Pitjeva, E., Soffel, M., and Wallace, P., "The IAU 2009 system of astronomical constants: the report of the IAU working group on numerical standards for fundamental astronomy." *Celestial Mechanics and Dynamical Astronomy*, Vol. 110, No. 4, August 2011, pp. 293–304. doi: 10.1007/s10569-011-9352-4.

[57] Janhunen, P. and Sandroos, A., "Simulation study of solar wind push on a charged wire: basis of solar wind electric sail propulsion," *Annales Geophysicae*, Vol. 25, No. 3, March 2007, pp. 755–767. doi: 10.5194/angeo-25-755-2007.

[58] Janhunen, P., Toivanen, P. K., Polkko, J., Merikallio, S., Salminen, P., Haeggström, E., Seppänen, H., Kurppa, R., Ukkonen, J., Kiprich, S., Thornell, G., Kratz, H., Richter, L., Krömer, O., Rosta, R., Noorma, M., Envall, J., Lätt, S., Mengali, G., Quarta, A. A., Koivisto, H., Tarvainen, O., Kalvas, T., Kauppinen, J., Nuottajärvi, A., and Obraztsov, A., "Electric solar wind sail: toward test missions," *Review of Scientific Instruments*, Vol. 81, No. 11, November 2010, pp. 111301–1–11301–11. doi: 10.1063/1.3514548.

[59] Mengali, G., Quarta, A. A., and Janhunen, P., "Electric sail performance analysis," *Journal of Spacecraft and Rockets*, Vol. 45, No. 1, January-February 2008, pp. 122–129. doi: 10.2514/1.31769.

[60] Yen, C. L., "Solar sail geostorm warning mission design," *14th AAS/AIAA Space Flight Mechanics Conference*, Maui, HI, February 8–12 2004, Paper AAS 04-107.

[61] Hudson, H. S., "A space parasol as a countermeasure against the greenhouse effect," *Journal of the British Interplanetary Society*, Vol. 44, March 1991, pp. 139–141.

[62] McInnes, C. R., "Minimum mass solar shield for terrestrial climate control," *Journal of the British Interplanetary Society*, Vol. 55, No. 9-10, 2002, pp. 307–311.

[63] Angel, R., "Feasibility of cooling the Earth with a cloud of small spacecraft near the inner Lagrange point (L1)," *Proceedings of the National Academy of Sciences of United States of America*, Vol. 103, No. 46, November 2006, pp. 17184–17189. doi: 10.1073/pnas.0608163103.

[64] Biggs, J. D. and McInnes, C. R., "Passive orbit control for space-based geoengineering," *Journal of Guidance, Control and Dynamics*, Vol. 33, No. 3, May-June 2010, pp. 1017–1020. doi: 10.2514/1.46054.

[65] Bookless, J. and McInnes, C. R., "Control of Lagrange point orbits using solar sail propulsion," *Acta Astronautica*, Vol. 62, May 2008, pp. 159–176. doi: 10.1016/j.actaastro.2006.12.051.

[66] Tsuda, Y., Mori, O., Funase, R., Hirotaka, S., Yamamoto, T., Saiki, T., Endo, T., Yonekura, K., Hoshino, H., and Kawaguchi, J., "Achievement of IKAROS – Japanese deep space solar sail demonstration mission," *Acta Astronautica*, Vol. 82, No. 2, February 2013, pp. 183–188. doi: 10.1016/j.actaastro.2012.03.032.

[67] Ogata, K., *Modern control engineering*, chap. 5, Prentice-Hall, Upper Saddle River, New Jersey, 1997, pp. 232–238, ISBN: 0-13-227307-1.

[68] Muhlemann, D. O., Hudson, R. H., Holdridge, D., Carpenter, R. L., and Oslund, K., "Observed solar pressure perturbations of Echo I," *Science*, Vol. 132, No. 3438, November 1960, pp. 1487. doi: 10.1126/science.132.3438.1487.

[69] Koblik, V., Polyakhova, E., and Sokolov, L., "Solar sail near the Sun: point-like and extended models of radiation source," *Advances in Space Research*, Vol. 48, No. 11, December 2011, pp. 1717–1739. doi: 10.1016/j.asr.2011.04.024.

[70] Mengali, G. and Quarta, A. A., "Optimal control laws for axially symmetric solar sails," *Journal of Spacecraft and Rockets*, Vol. 42, No. 6, November-December 2005, pp. 1130–1133. doi: 10.2514/1.17102.

[71] Hearn, E. J., *Mechanics of materials*, Vol. 1, chap. 9, Butterworth-Heinemann, 3rd ed., August 1997, pp. 202–203, ISBN: 0-750-63265-8.

[72] Chakrabarty, J., *Theory of plasticity*, chap. 5, Butterworth-Heinemann, 3rd ed., May 2006, pp. 359–361, ISBN: 0-750-66638-2.

[73] Rowe, W. M., Luedke, E. E., and Edwards, D. K., "Thermal radiative properties of solar sail film materials," *American Institute of Aeronautics and Astronautics and American Society of Mechanical Engineers, Thermophysics and Heat Transfer Conference, 2nd*, Palo Alto, CA, 24-26 May 1978, Paper AIAA 78-852.

[74] Banik, J. A., Lively, P. S., Taleghani, B. K., and Jenkins, C. H., "Solar sail topology variations due to on-orbit thermal effects," *Journal of Spacecraft and Rockets*, Vol. 44, No. 3, May-June 2007, pp. 558–570. doi: 10.2514/1.22902.

[75] Dachwald, B., Mengali, G., Quarta, A. A., and Macdonald, M., "Parametric model and optimal control of solar sails with optical degradation," *Journal of Guidance, Control, and Dynamics*, Vol. 29, No. 5, September-October 2006, pp. 1170–1178. doi: 10.2514/1.20313.

[76] Dachwald, B., Macdonald, M., McInnes, C. R., Mengali, G., and Quarta, A. A., "Impact of optical degradation on solar sail mission performance," *Journal of Spacecraft and Rockets*, Vol. 44, No. 4, July-August 2007, pp. 740–749. doi: 10.2514/1.21432.

[77] Jenkins, C. H. M., Gough, A. R., Pappa, R. S., Carroll, J., Blandino, J. R., Miles, J. J., and Rakoczy, J., "Design considerations for an integrated solar sail diagnostics system," *45th AIAA/ASME/ASCE/AHS/ASC Structures, Structural Dynamics & Materials Conference*, Palm Springs, California, April 19–22 2004, Paper AIAA 2004-1510.

[78] Su, X., Abdi, F., Taleghani, B., and Blandino, J. R., "Wrinkling analysis of a Kapton square membrane under tensile loading," *44th AIAA/ASME/ASCE/AHS/ASC Structures, Structural Dynamics, and Materials Conference*, Norfolk, Virginia, April 7–10 2003, Paper AIAA 2003-1985.

[79] Granqvist, C. G., Avendano, E., and Azens, A., "Electrochromic coatings and devices: survey of some recent advances," *Thin Solid Films*, Vol. 442, No. 1-2, October 2003, pp. 201–211. doi: 10.1016/S0040-6090(03)00983-0.

[80] Mori, O., Tsuda, Y., Shirasawa, Y., Saiki, T., Mimasu, Y., and Kawaguchi, J., "Attitude control of IKAROS solar sail spacecraft and its flight results," *61st International Astronautical Congress*, Prague, Czech Republic, September 27–October 1 2010, Paper IAC-10.C1.4.3.

[81] Funase, R., Shirasawa, Y., Mimasu, Y., Mori, O., Tsuda, Y., Saiki, T., and Kawaguchi, J., "Fuel-free and oscillation-free attitude control of IKAROS

solar sail spacecraft using reflectivity control device," *28th International Symposium on Space Technology and Science*, Okinawa, Japan, June 5–12 2011.

[82] Lücking, C. M., Colombo, C., and McInnes, C. R., "Orbit control of high area-to-mass ratio spacecraft using electrochromic coating," *61st International Astronautical Congress*, Prague, Czech Republic, September 27 – October 1 2010, Paper IAC-10-C1.2.7.

[83] Lücking, C. M., Colombo, C., and McInnes, C. R., "Electrochromic orbit control for smart-dust devices," *Journal of Guidance, Control and Dynamics*, Vol. 35, No. 5, September-October 2012, pp. 1548–1558. doi: dx.doi.org/10.2514/1.55488.

[84] McInnes, C. R., "Passive control of displaced solar sail orbits," *Journal of Guidance, Control and Dynamics*, Vol. 21, No. 6, November–December 1998, pp. 975–982. doi: 10.2514/2.4334.

[85] Chopra, K. L., Paulson, P. D., and Dutta, V., "Thin-film solar cells: an overview," *Progress in Photovoltaics: Research and Applications*, Vol. 12, No. 2-3, March-May 2004, pp. 69–92. doi: 10.1002/pip.541.

[86] Dachwald, B., "Optimization of interplanetary solar sailcraft trajectories using evolutionary neurocontrol," *Journal of Guidance, Control, and Dynamics*, Vol. 27, No. 1, January-February 2004, pp. 66–72. doi: 10.2514/1.9286.

[87] Quarta, A. A. and Mengali, G., "Minimum-time space missions with solar electric propulsion," *Aerospace Science and Technology*, Vol. 15, No. 5, July-August 2011, pp. 381–392. doi: 10.1016/j.ast.2010.09.003.

[88] Otte, K., Makhova, L., Braun, A., and Konovalov, I., "Flexible Cu(In,Ga)Se_2 thin-film solar cells for space application," *Thin Solid Films*, Vol. 511-512, July 2006, pp. 613–622. doi: 10.1016/j.tsf.2005.11.068.

[89] Franklin, G. F., Powell, J. D., and Emami-Naeini, A., *Feedback control of dynamic systems*, chap. 4, Prentice-Hall, 4th ed., 2002, pp. 227–229, ISBN: 0-130-32393-4.

[90] Young, R. M., "Updated Heliostorm warning mission: enhancements based on new technology," *48th AIAA/ASME/ASCE/AHS/ASC Structures, Structural Dynamics, and Materials Conference*, Honolulu, Hawaii, April 23–26 2007, Paper AIAA 2007-2249.

[91] Adeli, S. N., Lappas, V., and Wie, B., "A scalable bus-based attitude control system for solar sails," *Advances in Space Research*, Vol. 48, No. 11, December 2011, pp. 1836–1847. doi: 10.1016/j.asr.2011.08.024.

[92] Dachwald, B., "Interplanetary mission analysis for non-perfectly reflecting solar sailcraft using evolutionary neurocontrol," *AAS/AIAA Astrodynamics Specialist Conference*, Big Sky, Montana, August 3–7 2003, Paper AAS 03-579.

[93] Capderou, M., *Satellites orbit and missions*, chap. 3, 7, Springer-Verlag, 2005, ISBN: 2-287-21317-1.

[94] Chobotov, V. A., *Orbital mechanics*, chap. 10, AIAA Educational Series, AIAA, 3rd ed., 2002, pp. 215–240, ISBN: 1-56347-537-5.

[95] Coffey, S. L., Deprit, A., and Deprit, E., "Frozen orbits for satellites close to an Earth-like planet," *Celestial Mechanics and Dynamical Astronomy*, Vol. 59, No. 1, May 1994, pp. 37–72. doi: 10.1007/BF00691970.

[96] Lara, M., Deprit, A., and Elipe, A., "Numerical continuation of families of frozen orbits in the zonal problem of artificial satellite theory," *Celestial Mechanics and Dynamical Astronomy*, Vol. 62, No. 2, June 1995, pp. 167–181. doi: 10.1007/BF00692085.

[97] Scheeres, D. J., Guman, M. D., and Villac, B. F., "Stability analysis of planetary satellite orbiters: application to the Europa orbiter," *Journal of Guidance Control and Dynamics*, Vol. 24, No. 4, July-August 2001, pp. 778–787. doi: 10.2514/2.4778.

[98] Paskowitz, M. E. and Scheeres, D. J., "Design of science orbits about planetary satellites: application to Europa," *Journal of Guidance Control and Dynamics*, Vol. 29, No. 5, September-October 2006, pp. 1147–1158. doi: 10.2514/1.36220.

[99] Abad, A., Elipe, A., and Tresaco, E., "Analytical model to find frozen orbits for a lunar orbiter," *Journal of Guidance, Control and Dynamics*, Vol. 32, No. 3, May-June 2009, pp. 888–898. doi: 10.2514/1.38350.

[100] Lara, M., Palacián, J. F., Yanguas, P., and Corral, C., "Analytical theory for spacecraft motion about Mercury," *Acta Astronautica*, Vol. 66, No. 7–8, April-May 2010, pp. 1022–1038. doi: 10.1016/j.actaastro.2009.10.011.

[101] Delsate, N., Robutel, P., Lemaître, A., and Carletti, T., "Frozen orbits at high eccentricity and inclination: application to Mercury orbiter," *Celestial*

Mechanics and Dynamical Astronomy, Vol. 108, No. 3, November 2010, pp. 275–300. doi: 10.1007/s10569-010-9306-2.

[102] Leipold, M. E. and Wagner, O., "Mercury Sun-synchronous polar orbits using solar sail propulsion," *Journal of Guidance Control and Dynamics*, Vol. 19, No. 6, November-December 1996, pp. 1337–1341. doi: 10.2514/3.21791.

[103] Macdonald, M., McKay, R. J., Vasile, M., and Bosquillon De Frescheville, F., "Extension of the Sun-synchronous orbit," *Journal of Guidance Control and Dynamics*, Vol. 33, No. 6, November-December 2010, pp. 1935–1939. doi: 10.2514/1.49011.

[104] Anderson, P. and Macdonald, M., "Extension of highly elliptical orbits using continuous low-thrust propulsion," *Journal of Guidance, Control and Dynamics*, Vol. 36, No. 1, January–February 2013, pp. 282–292. doi: 10.2514/1.55304.

[105] Tremaine, S., Touma, J., and Namouni, F., "Satellite dynamics on the Laplace surface," *The Astronomical Journal*, Vol. 137, No. 3, March 2009, pp. 3706–3717. doi: 10.1088/0004-6256/137/3/3706.

[106] Quarta, A. A. and Mengali, G., "Optimal switching strategy for radially accelerated trajectories," *Celestial Mechanics and Dynamical Astronomy*, Vol. 105, No. 4, December 2009, pp. 361–377. doi: 10.1007/s10569-009-9233-2.

[107] Beutler, G., *Methods of celestial mechanics, Vol. I*, chap. 3, Astronomy and Astrophysics Library, Springer-Verlag, 2005, pp. 44–121, ISBN: 3-540-40749-9.

[108] Farago, F. and Laskar, J., "High-inclination orbits in the secular quadrupolar three-body problem," *Monthly Notices of the Royal Astronomical Society*, Vol. 401, No. 2, January 2010, pp. 1189–1198. doi: 10.1111/j.1365-2966.2009.15711.x.

[109] Kozai, Y., "The motion of a close Earth satellite," *Astronomical Journal*, Vol. 64, No. 1274, November 1959, pp. 367–377. doi: 10.1086/107957.

[110] Boué, G. and Laskar, J., "Precession of a planet with a satellite," *Icarus*, Vol. 185, No. 2, December 2006, pp. 312–330. doi: 10.1016/j.icarus.2006.07.019.

[111] Bloch, A. M., *Nonholonomic mechanics and control*, chap. 3, Interdisciplinary Applied Mathematics, Springer-Verlag, 2005, p. 152, ISBN: 0-387-95535-6.

[112] Archinal, B. A., A'Hearn, M. F., Bowell, E., Conrad, A., Consolmagno, G. J., Courtin, R., Fukushima, T., Hestroffer, D., Hilton, J. L., Krasinsky, G. A., Neumann, G., Oberst, J., Seidelmann, P. K., Stooke, P., Tholen, D. J., Thomas, P. C., and Williams, I. P., "Report of the IAU working group on cartographic coordinates and rotational elements: 2009," *Celestial Mechanics and Dynamical Astronomy*, Vol. 109, No. 2, February 2011, pp. 101–135. doi: 10.1007/s10569-010-9320-4.

[113] Anderson, J. D., Colombo, G., Esposito, P. B., Lau, E. L., and Trager, G. B., "The mass, gravity field, and ephemeris of Mercury," *Icarus*, Vol. 71, No. 3, September 1987, pp. 337–349. doi: 10.1016/0019-1035(87)90033-9.

[114] Standish, E. M., "Keplerian elements for approximate positions of the major planets," `http://ssd.jpl.nasa.gov/txt/aprx_pos_planets.pdf`, cited 8th February 2013.

[115] Walker, M. J. H., Owens, J., and Ireland, B., "A set of modified equinoctial orbit elements," *Celestial Mechanics*, Vol. 36, No. 4, August 1985, pp. 409–419. doi: 10.1007/BF01227493.

[116] Walker, M. J. H., Owens, J., and Ireland, B., "Errata: A set of modified equinoctial orbit elements," *Celestial Mechanics*, Vol. 38, No. 4, April 1986, pp. 391–392. doi: 10.1007/BF01238929.

[117] Hintz, G. R., "Survey of orbit element sets," *Journal of Guidance Control and Dynamics*, Vol. 31, No. 3, May-June 2008, pp. 785–790. doi: 10.2514/1.32237.

[118] Meire, R. and Vanderbauwhede, A., "A useful result for certain linear periodic ordinary differential equations," *Journal of Computational and Applied Mathematics*, Vol. 5, No. 1, March 1979, pp. 59–61. doi: 10.1016/0771-050X(79)90028-7.

List of Figures

List of Tables

List of Acronyms

AEP *Artificial Equilibrium Point*

CR3BP *Circular Restricted Three-Body Problem*

EMP *Electrochromic Material Panel*

ER3BP *Elliptic Restricted Three-Body Problem*

E-Sail *Electric Solar Wind Sail*

MagSail *Magnetic Sail*

M2P2 *Mini-Magnetospheric Plasma Thruster*

R3BP *Restricted Three-Body Problem*